

**DESIGN OPTIMIZATION AND PRECLINICAL TESTING OF PEDIATRIC ROTARY
BLOOD PUMPS AND COMPONENTS: TOWARDS THE PEDIAFLOW® VAD**

by

Salim Esmail Olia

B.S.E. Bioengineering, University of Pittsburgh, 2009

Submitted to the Graduate Faculty of
the Swanson School of Engineering in partial fulfillment
of the requirements for the degree of
Doctor of Philosophy in Bioengineering

University of Pittsburgh

2018

UNIVERSITY OF PITTSBURGH
SWANSON SCHOOL OF ENGINEERING

This dissertation was presented

by

Salim Esmail Olia

It was defended on

July 16, 2018

and approved by

Harvey S. Borovetz, PhD
Professor; Departments of Surgery & Bioengineering

James F. Antaki, PhD *
Professor; Department of Biomedical Engineering, Carnegie Mellon University, PA;
Departments of Bioengineering & Surgery

Peter D. Wearden, MD PhD †
Assistant Professor; Departments of Cardiothoracic Surgery & Bioengineering

Dissertation Director: Marina V. Kameneva, PhD
Research Professor; Departments of Surgery & Bioengineering

Current Affiliations:

* Professor; Department of Biomedical Engineer, Cornell University, NY

† Chair; Department of Cardiovascular Services, Nemours Children's Hospital, FL

Copyright © by Salim Esmail Olia

2018

DESIGN OPTIMIZATION AND PRECLINICAL TESTING OF PEDIATRIC ROTARY BLOOD PUMPS AND COMPONENTS: TOWARDS THE PEDIAFLOW® VAD

Salim Esmail Olia, PhD

University of Pittsburgh, 2018

Limited options exist for children ($BSA < 1.5 \text{ m}^2$) requiring long-term mechanical circulatory support (MCS). Unlike adults where compact, 3rd generation, continuous-flow, implantable rotary blood pumps (RBPs) are now the standard for ventricular assist device (VAD)-indications, the only pediatric-approved chronic MCS device is the Berlin Heart® EXCOR®: a 1st generation pulsatile, pneumatically-driven, paracorporeal life-saving technology albeit with a substantial risk profile associated with frequent neurological and coagulation-related serious adverse events.

In support of the smallest and most vulnerable patients, the goal of this research is to facilitate the development and translation of next-generation pediatric RBPs, including the University of Pittsburgh-led Consortium's PediaFlow®: a miniature, implantable, rotodynamic, fully magnetically levitated, continuous-flow pediatric VAD intended to support patients between 3 to 15 kg at a flow rates of 0.3-1.5 L/min for up to six months.

Presented here is the *i*) development of a standardized method for *in vitro* mechanical blood trauma testing of pediatric MCS devices; *ii*) design and *ex vivo* evaluation of a novel, pediatric-appropriate, suction resistant, placement insensitive, left ventricular drainage cannula; *iii*) creation of an MCS-tailored monitoring software for preclinical testing; *iv*) development of a

PediaFlow®-specific flow estimation algorithm; and v) hemocompatibility findings *in vitro* and *in vivo* of the 4th generation PediaFlow® (PF4) VAD.

The PF4, comparable in size to an AA battery, is the embodiment of more than a decade of extensive computational and experimental efforts over the span of four device iterations to minimize size, optimize performance, and maximize safety. This dissertation represents the work and results to date of PediaFlow® PF4 on the path to preclinical testing to submit an Investigation Device Exception (IDE) application in anticipation of eventual clinical trials.

TABLE OF CONTENTS

NOMENCLATURE	XVI
PREFACE	XVIII
1.0 INTRODUCTION	1
1.1 MECHANICAL CIRCULATORY SUPPORT	1
1.1.1 Adult Experience	1
1.1.2 Assisted Circulation in Pediatrics	2
1.2 MECHANICAL BLOOD TRAUMA	3
1.2.1 Introduction	4
1.2.2 Hemolysis	7
1.2.3 Sublethal RBC Damage.....	8
1.2.4 Factors Affecting RBC Mechanical Trauma	16
1.2.5 Sublethal RBC Damage Effects on Platelets.....	18
1.2.6 Blood Transfusions in MCS	19
1.2.7 Conclusions	20
1.3 THE PEDIAFLOW® PEDIATRIC VAD	21
1.3.1 Development and Evolution	21
1.3.2 PediaFlow® 4th Generation (PF4).....	22
1.4 OBJECTIVES	24

	Objective #1: Design, optimize, and validate new standards of practice for the <i>in vitro</i> measurement of mechanical blood trauma in pediatric blood pumps.	25
	Objective #2: Evaluate the performance and suitability of an inflow cannula design for use with pediatric rotary blood pumps.	26
	Objective #3: Develop a comprehensive Diagnostic Support System (DSS) for <i>in vivo</i> preclinical testing of the PediaFlow® pediatric VAD.	26
2.0	<i>IN VITRO</i> ASSESSMENT OF MECHANICAL BLOOD TRAUMA IN PEDIATRIC BLOOD PUMPS	27
2.1	INTRODUCTION.....	27
2.1.1	Benchtop Hemolysis Testing	27
2.1.2	Previous PediaFlow® Testing	28
2.2	A REUSABLE, COMPLIANT, SMALL VOLUME BLOOD RESERVOIR FOR <i>IN VITRO</i> FLOW LOOPS.....	30
2.2.1	Introduction.....	30
2.2.2	Materials and Methods.....	32
2.2.3	Results.....	34
2.2.4	Summary.....	37
2.3	RESERVOIR FOR INTRAVENTRICULAR MCS DEVICES.....	37
2.3.1	Methods.....	38
2.3.2	Results and Discussion	39
2.3.3	Limitations and Future Work.....	41
2.4	MATERIALS AND METHODS	42
2.4.1	Blood Preparation	43
2.4.2	Circulating Mock Loop	43
2.4.3	Blood Sampling.....	45
2.4.4	Measurements and Analysis.....	45
2.5	RESULTS.....	46

2.6	DISCUSSION	47
2.6.1	Limitations.....	49
2.7	CONCLUSIONS	50
3.0	DESIGN AND EVALUATION OF A PEDIATRIC INFLOW CANNULA FOR ROTARY BLOOD PUMPS	51
3.1	INTRODUCTION.....	52
3.1.1	Previous Cannulae (PF1-PF3).....	53
3.1.2	Conformal Cannula	54
3.1.3	Initial PF4 Implants.....	57
3.2	MATERIALS AND METHODS	58
3.2.1	Cannula Design.....	58
3.2.2	Experimental Setup	59
3.2.3	Data Analysis	61
3.3	RESULTS	62
3.3.1	Positional Sensitivity.....	63
3.3.2	Borescope Results	64
3.4	DISCUSSION	65
3.5	CONCLUSIONS	68
4.0	A COMPREHENSIVE DIAGNOSTIC SUPPORT SYSTEM (DSS) FOR <i>IN VIVO</i> TESTING OF THE PEDIAFLOW®	69
4.1	INTRODUCTION.....	69
4.1.1	PediaFlow® Operation and Monitoring.....	70
4.2	SYSTEM ARCHITECTURE AND DEVELOPMENT	72
4.2.1	Materials and Methods.....	73
4.2.2	Results and Discussion	74
4.2.3	Future Work.....	77

4.3	PEDIAFLOW FLOW ESTIMATION	78
4.3.1	Introduction	78
4.3.2	Materials and Methods	79
4.3.3	Results and Discussion	81
4.3.4	Future Work	89
5.0	PRECLINICAL PERFORMANCE OF THE 4 TH GENERATION PEDIAFLOW® PEDIATRIC VAD	90
5.1	METHODS	90
5.1.1	<i>In Vitro</i> Assessment	90
5.1.2	<i>In Vivo</i> Evaluation	91
5.1.3	Current PF4 Implantable Design	91
5.2	RESULTS	93
5.3	DISCUSSION	96
5.4	CONCLUSIONS	98
6.0	FINAL CONCLUSIONS AND FUTURE DIRECTIONS	100
6.1.1	<i>In Vitro</i> Blood Trauma Testing	101
6.1.2	Sublethal RBC Damage	101
6.1.3	Outflow Graft Permeability	102
6.1.4	DSS Functionality	102
6.1.5	Transfusions During MCS	102
	APPENDIX A	105
	APPENDIX B	116
	APPENDIX C	124
	APPENDIX D	137
	BIBLIOGRAPHY	162

LIST OF TABLES

Table 1. Preliminary <i>in vivo</i> implants of a <i>de novo</i> conformal cannula using the Levitronix ® PediMAG® extracorporeal blood pump.	56
Table 2. Positional sensitivity results for the three cannulae using the over-pumping protocol ($n_{op} = 21$)	63
Table 3. The pump constants, parameters, and measurements for dimensional analysis, and the three nondimensional characteristic coefficient equations for the flow estimator algorithm.....	86
Table 4. Emboli generation rate in saline with the Thoratec® PediMAG®.	118
Table 5. Summary of the 4th generation PediaFlow® prototypes (PF4.x) fabricated by the Consortium.	124
Table 6. The inflow cannulae developed, utilized or under consideration for use with the PF4.	125
Table 7. The outflow graft assemblies used during the <i>in vivo</i> assessments of the PF4.....	126
Table 8. Summary of the <i>in vivo</i> PF4-implanted juvenile ovine experiments.	131
Table 9. Additional blood parameters of the 3rd and 4th generation PediaFlow® and sham <i>in vivo</i> animal studies presented in 5.2. All were within reference values.....	133
Table 10. Summary of the surgical sham (control) animal studies.....	135

LIST OF FIGURES

Figure 1. Bright-field illuminated normal and rigidified erythrocytes undergoing shear using the Linkam Shearing Stage.	11
Figure 2. Bovine RBC aggregation under Bright-field illumination.	13
Figure 3. Effect of suspension media with matched viscosities on bovine RBC mechanical fragility	18
Figure 4. Evolution and miniaturization of the PediaFlow® from the first prototype (PF1) to the 4 th generation (PF4) pediatric VAD.	22
Figure 5. The PediaFlow® PF4 prototype and implantable components.	23
Figure 6. Characteristic H-Q pump curves of PF3 and PF4 using a blood analog (viscosity = 2.39 cP).	24
Figure 7. A) Benchtop hemolysis testing of the 1 st generation PediaFlow®, and B) top view schematic of the <i>in vitro</i> mock loop for the PF1-PF3 prototypes utilizing a magnetic stir plate.	28
Figure 8. The elevated reservoir and magnetic stir plate during <i>in vitro</i> testing of a PF3 prototype pump.	29
Figure 9. Example mock loops used for <i>in vitro</i> hemolysis testing of blood pumps.	31
Figure 10. Commercially available, pediatric (left) and adult (right) soft-shell reservoirs used in previous benchtop blood biocompatibility experiments highlighting the deficient extraneous and fenestrated ports.	32
Figure 11. Schematic of the reusable ½”-port A) printed base, B) machined clamp set, and C) the manufactured reservoir components with the modified blood bag before assembly.	33
Figure 12. CFD predicted velocity contours at 0.5 L/min for the commercial venous blood bag with the fenestrated port defined as the reservoir A) inlet or B) outlet, and C) the developed ½”-port reservoir assembly.	35
Figure 13. The vertically hung, ½”-port blood reservoir assembly after clamping, filling and de-airing.	36

Figure 14. A) The intraventricular-RBP blood reservoir design, B) the reservoir inlet-entrance angles ($\phi = 60^\circ$ & 80°) under consideration, and (inset) the generic RBP-model used during CFD.	38
Figure 15. Velocity pathlines of the intraventricular-MCS compatible, 500 mL, <i>in vitro</i> blood reservoir superimposed with an emboli particle study to assess air entrapment.	40
Figure 16. Benchtop hemolysis loop with the SLA-printed blood reservoir and an inline compliance chamber during <i>in vitro</i> testing of an intraventricular RBP.....	41
Figure 17. A) Schematic of the pediatric <i>in vitro</i> hemolysis loop and B) actual experimental setup.	44
Figure 18. A) NIH results for the eight RBPs tested using the pediatric <i>in vitro</i> protocol, a summary of the daily blood pool parameters (inset), and B) a comparison between the PF3 and PF4 prototypes.	46
Figure 19. A) NIH results (AVG \pm SD) over corresponding blood TPP concentration grouped by TPP less than 6.0 g/dL and/or RBC MFI greater than 0.6, and B) a histogram plot of the same data.....	47
Figure 20. NIH results (AVG \pm SD) of the PF4.x prototypes after excluding donor blood pools with a rocker bead test mechanical fragility index above 0.6 or a total plasma protein concentration less than 6.0 g/dL.	48
Figure 21. Representative inflow cannula used for PF1-PF3 <i>in vivo</i> implants with custom sewing rings and pump connectors.....	54
Figure 22. The pediatric conformal inflow cannula assembly	55
Figure 23. Necropsy results of the two chronic conformal cannula implants.	56
Figure 24. The bevel-type inflow cannula developed and used with the initial PF4 implants.....	57
Figure 25. The three pediatric inflow cannulae and respective tip geometries under consideration	58
Figure 26. (A) Schematic of the modified <i>ex vivo</i> isolated-flow loop used to assess cannula performance (aortic vent not shown) and (B) an image of the <i>ex vivo</i> flow loop in the normally aligned state.	60
Figure 27. Sample data set from one experiment showing cannula performance as measured by achievable flow rate under both protocols.....	62
Figure 28. Positional sensitivity results of the three cannulae in the hypovolemic protocol ($n_{hv} = 15$).	64

Figure 29. Color enhanced representative intraventricular images of the normally aligned cannulae (top) and the misaligned cannulae (bottom) from the boroscope.....	65
Figure 30. Occlusion modality results of the left ventricle as determined by intraventricular imaging and flow rate analysis.	66
Figure 31. A screenshot of the WinDAQ® window and <i>in vivo</i> computer cart (inset) running the software.	71
Figure 32. A screenshot of the first DSS1.1 program iteration used both <i>in vitro</i> and <i>in vivo</i>	74
Figure 33. The DSS2.1 during an <i>in vivo</i> implant.	75
Figure 34. The DSS3.2 and the PediaFlow®/Levacor® pump controller software.	76
Figure 35. A) An automated DSS4.1 email alarm and attached screenshot (B) sent using the SMTP service.....	77
Figure 36. A schematic (left) and example image (right) of the simple static loop used for H-Q testing to acquire hemodynamic and PF4 controller values under steady, non-pulsatile conditions.	80
Figure 37. The schematic (left) and actual setup (right) of the pulse duplicator setup mimicking PF4 pump operation <i>in vivo</i> for acquiring the H-Q data under pulsatile-flow conditions used to develop the parameters and coefficients for flow estimation.	81
Figure 38. H-Q plots for two PF4.x prototypes generated from the <i>in vitro</i> mock loop experiments.....	82
Figure 39. Signal measurements of PF4.x prototype generated under pulsatile conditions	83
Figure 40. Motor current signal shortcomings with the original PF4 preclinical controllers.	83
Figure 41. Rotor position (RP) signal drift (red) over the 115 post-operative hour (POH) period and ‘RP/MS regression’ flow estimator compared to the flow probe measurement (blue).	85
Figure 42. The original (left) and modified (right) algorithm for the dimensional analysis PF4 flow estimator.	87
Figure 43. S044-12 (PF4.6.1) implant showing the overall parameter trends (left) and a signal snippet (right).....	87
Figure 44. S011-13 (PF4.6.1) with the upgraded controller showing the overall parameter trends (left) and a signal snippet showcasing the enhanced MC signal (right).	88
Figure 45. The PF4 PediaFlow® prototype and implantable components	92

Figure 46. The calculated <i>in vitro</i> Normalized Index of Hemolysis (NIH) values (mean±SD) for the PF4.x prototypes compared to the PediMAG® control.	93
Figure 47. Results of the two PF4 ovine studies using the current-design cannulae system (PF4-S10, PF4-S11), in comparison to the previous 3 rd -gen. chronic implant (PF3-S01) and the non-implanted surgical control ‘Shams’ (n=3, mean±SD):.....	94
Figure 48. Necropsy images of PF4-S11 (14-day) implant.....	95
Figure 49. Explant photos of the PF4-S10 (60-day) implant.	96
Figure 50. A) Schematic of reduced volume and large volume rocker bead tests running simultaneously and B) comparison of MFI values obtained from reduced volume and large volume tests run simultaneously at matched hematocrits between 25 and 40% using bovine blood (Pearson’s correlation coefficient $r = 0.941$).	109
Figure 51. A) MFI values at hematocrit concentrations between 25 and 50% and B) the resultant regression analysis of the MFI residuals after linearization using the reduced volume RBT with human blood.	111
Figure 52. Comparison of the reduced volume MMFI to the MFI (mean ± 1.0 SD) across four different human blood units at hematocrits between 25 and 50%.	112
Figure 53. Effect of total plasma protein on red blood cell modified mechanical fragility index values as measured by the reduced volume RBT at 40% hematocrit using human blood. (* - $P < 0.01$).	113
Figure 54. Schematic of the test loop for assessment of gas emboli and hemolysis.	119
Figure 55. Display screen of the EDAC Quantifier system.	120
Figure 56. <i>In vitro</i> test setup with the EDAC cells (inset) used to measure the emboli within the flow loop.....	120
Figure 57. Plot of NIH ± SDEV as a function of negative inlet pressure and flow rate.....	121
Figure 58. Plot of emboli generation rate ± SDEV as a function of negative inlet pressure and flow rate.....	121
Figure 59. Total gaseous emboli entering and exiting the pump at each inlet pressure and flow rate.....	122
Figure 60. Histogram of total emboli segregated by size diameter for one 0.5 L/min study at -40 mmHg.....	123
Figure 61. Qualitative analysis of outflow graft permeability.....	127
Figure 62. The PF4 ‘quick-connect’ attachment mechanism.	128

Figure 63. A) The original PF4.x threaded nut (A) driveline connector and the new push-pull connector (B) used in PF4.6.1 and subsequent prototypes.....129

Figure 64. Plasma-free hemoglobin values for the initial *in vivo* PF4 implants.....132

Figure 65. Necropsy images of the PF3-S01 (72-day) implant.136

NOMENCLATURE

The following abbreviations are used repeatedly throughout the document:

ACT	... activated clotting time
AF	... actual (measured) flow rate
CF	... continuous flow
CPB	... cardiopulmonary bypass
BSA	... body surface area
DAQ	... data acquisition
DSS	... diagnostic support system
ECMO	... extracorporeal membrane oxygenation
FB	... fibrinogen
Hb	... hemoglobin
fHb	... free hemoglobin
Ht	... hematocrit
LAP	... left atrial pressure
LV	... left ventricle
LVP	... left ventricle pressure
MC	... motor current
MCS	... mechanical circulatory support
MCSD	... mechanical circulatory support device

MFI	... (RBC) mechanical fragility index
MMFI	... modified (RBC) mechanical fragility index
MS	... motor speed
NIH	... normalize index of hemolysis
PF1-PF4	... 1 st - 4 th developmental PediaFlow® generation
PEx.y	... PediaFlow® pump prototype
plfHb	... plasma-free hemoglobin
POD	... post-operative day
POH	... post-operative hour
RBC	... red blood cell
RBP	... rotary blood pump
RBT	... rocker bead test
RP	... (axial) rotor position
-Sxxx	... <i>in vivo</i> ovine implant study number
SLA	... stereolithography additive (3D printing process)
TPP	... total plasma protein
VAD	... ventricular assist device

PREFACE

This dissertation was possible only through the grace, guidance, and contributions of a great number of people, and reflects of the innumerable opportunities afforded to me throughout. First and foremost, I would like to thank my advisor Dr. Marina Kameneva for her endless support and patience. Since allowing me to join her lab as a sophomore undergraduate, she has spent countless hours teaching and assisting me in experimental design, data analysis, conference presentation, and manuscript preparation. My development into a researcher and subsequent contributions to this field are directly attributable to her expertise, continuous curiosity, and work ethic; for which I am forever grateful.

I would also like to express my gratitude to Dr. Harvey Borovetz, Dr. James Antaki, and Dr. Peter Wearden as the members of my committee. As Chair and Chair-Emeritus of the Bioengineering Department during his tenure as my co-advisor, Dr. Borovetz was a continual beacon of encouragement, motivation, and guidance. I am especially grateful for Dr. Antaki and Dr. Wearden's participation, as two premier experts in pediatric mechanical circulatory support and at the helm for technical and clinical development of the PediaFlow®, respectively.

Additionally, it would be remiss of me to not recognize the importance of the Artificial Heart Program at UPMC towards my personal and professional development. A source of continual inspiration by highlighting on-going challenges and unmet needs, my experiences clinically helped focus my research while allowing me to apply my knowledge to help support

our patients. I can't thank enough Dr. Richard Schaub and Stephen Winowich for the opportunity they afforded to me.

For the work presented in this dissertation, I would like to acknowledge in particular- *Kameneva Laboratory*: Dr. Amanda Daly, Daniel Crompton, Michael Griffin, Dr. Richard Miller, Hannah Voorhees, Andrew Wearden, Dr. Rui Zhao, and Luke Ziegler. *Wagner Laboratory*: Dr. Venkat Shankarraman and Dr. Sang-Ho Ye. *Carnegie Mellon University*: Dr. Arielle Drummond, Dr. Antonio Ferreira, Dr. Jeongho Kim, and Dr. Dennis Trumble. *LaunchPoint Technologies*: Dave Paden, Shaun Snyder, Josiah Verkaik, and Dr. Jingchun Wu. *McGowan Center for Preclinical Studies (CPCS)*: Shawn Bengston, Chelsea Causgrove, Teri Dulak, Joseph Hanke, Amy Jo Wiester, along with Janice Curnow, Jennifer Geisler, and Jessica Lang (Special T, Lily, and I couldn't have done it without them). *FDA CDRH*: Dr. Luke Herbertson and Dr. Richard Malinauskas.

I am profoundly grateful for the financial support provided towards me through Dr. Sanjeev Shroff's Cardiovascular Bioengineering Training Program (NIH T32-HL076124), an NIH SBIR R44 HL118907, the US Food and Drug Administration's Critical Path Initiative, the Commonwealth of Pennsylvania, the McGowan Institute for Regenerative Medicine and the Department of Bioengineering at the University of Pittsburgh.

The leadership of NHLBI and Dr. J. Timothy Baldwin to create novel mechanical circulatory support systems for pediatric patients was instrumental towards the inception and development of the PediaFlow®. Funding for the PediaFlow® and the presented research was provided through the NIH Pediatric Circulatory Support (Contract No. N01-HV-48192) and PumpKIN (Contract No. N01-HV-00235) -Programs, NICHD Grant 5RC1HD064041, NIH STTR Grant R41 HL077028, and NIH Grant R01 HL089456.

Thanks to Dr. Philip Marascalco, Dr. Timothy Maul, and Dr. Joshua Woolley for taking me under your wings, or at least allowing a ‘wet behind the ears’ undergrad to tag-along, while remaining my mentors to this day. I’d also like to recognize Dr. Douglas Nelson for his continual and well-appreciated presence throughout my graduate career as both a fellow student and cherished friend.

Finally, none of this would have ever been possible without the love and support of my family; it’s long overdue to flip the hourglass...

1.0 INTRODUCTION

This section has been published in part in The Journal of Thoracic and Cardiovascular Surgery [1].

Within the United States, 25% of all neonates born with a congenital heart defect will require invasive treatment within the first 12 months of life [2]. Nearly 1,800 infants die from congenital heart disease each year while an additional 350 develop cardiomyopathy [3, 4]. Children under 15 kg listed for cardiac transplantation have the highest waiting list mortality rate (17%) in all solid-organ transplantation categories[5]. Cardiac transplantation remains the standard of care for refractory heart failure, but with limited donor availability, only 56% of infants listed received an organ over the last decade [6]. While the use of mechanical circulatory support (MCS) has successfully decreased waiting list mortality and has been used as a bridge-to-recovery, availability of MCS devices (MCSDs) for children remains limited [7, 8].

1.1 MECHANICAL CIRCULATORY SUPPORT

1.1.1 Adult Experience

Heart disease is the leading cause of mortality in adults internationally and domestically, responsible for 1 in every 7 deaths within the United States.[9]. With MCSD development

spanning more than five decades for adults, multiple paradigm shifts from pulsatile total artificial hearts, to pulsatile (1st generation) ventricular assist devices (VADs), to continuous-flow (CF) rotary blood pumps (RBPs) have revolutionized the field of MCS in adults. Utilizing centrifugal- or axial-flow designs with a single moving impeller eliminates the flexible blood membranes, check valves, long cannulas, and tortuous blood paths required for prior pulsatile pumps. This increased simplicity allows for smaller blood-contacting surface area and reduced dead space, thereby reducing thrombosis potential and infection risks, in addition to decreasing the overall device size [10]. Similarly, controller size has been markedly reduced by the elimination of large percutaneous drivelines, compressors, vacuum pumps, solenoids, and large power supplies associated with positive-displacement VADs [11]. Supported by either blood bearings/seals (2nd generation) or suspended by hydrodynamic or electromagnetic forces (3rd generation), RBPs are now the standard for chronic MCS support clinically [11, 12]. With multiple adult CF VADs approved by the Food and Drug Administration (FDA) for bridge-to-transplant or destination therapy applications, these technologies have rescued thousands of adults with refractory end-stage heart failure, with additional devices currently under development or in clinical trials [13].

1.1.2 Assisted Circulation in Pediatrics

Extracorporeal membrane oxygenation (ECMO) is used extensively for providing temporary cardiac support to children from neonates to adolescents. Although resource intensive, it is cost effective, institutionally available, and rapidly initiated [14]. However, ECMO is indicated only for short durations requiring immobilization, sedation, and has a high complication rate related to bleeding and thromboembolism proportional to support length [15].

For adolescents with sufficient Body Surface Area (BSA), the use of adult-indicated durable CF-VADs is partially reported in the PediMACs registry with a six month survival rate approaching 90% (n=126) since creation in 2012 [16]. The majority of CF-VADs were implanted in patients 6 years of age or older due to device size, though there is a growing off-label usage of the smaller HeartWare® HVAD typically implanted with an outflow graft constriction or ran at lower speeds (RPM) to maintain pediatric-appropriate flow rates in younger patients [16-20]. Operating outside of its intended design range, pump performance is markedly reduced and therefore increasing the risk for potential complications. Unlike adults however, currently the only FDA approved, pediatric-specific, bridge-to-transplant MCS device is the Berlin Heart® EXCOR®; a paracorporeal, pneumatically-driven, pulsatile VAD that provides extended support for the pediatric population through the use of varying volume sized pumps coupled to a large pneumatic driver. The potential of the EXCOR® as a life-saving technology for children with heart failure is reflected in our center’s experience since 2004 [21]. However the EXCOR® has a substantial risk profile with approximately 80% of patients experiencing at least one significant adverse event, the majority (~50%) from severe bleeding or infection, and is associated with frequent pump exchanges due to device thrombosis around the valve leaflets [22].

1.2 MECHANICAL BLOOD TRAUMA

This section has been published in part in International Journal of Artificial Organs [23].

Despite many decades of improvements in MCSDs, blood damage remains a serious problem during support, contributing to variety of adverse events, and consequently affecting

patient survival and quality of life. The mechanisms of cumulative cell damage in continuous-flow blood pumps are still not fully understood despite numerous *in vitro*, *in vivo*, and *in silico* studies of blood trauma. Previous investigations have almost exclusively focused on *lethal* blood damage, namely hemolysis, which is typically negligible during normal operation of current generation MCSDs. The measurement of plasma free hemoglobin (plfHb) concentration to characterize hemolysis is straightforward, however *sublethal* trauma is more difficult to detect and quantify since no simple direct test exists. Similarly, while multiple studies have focused on thrombosis within blood pumps and accessories, sublethal blood trauma and its sequelae have yet to be adequately documented or characterized. This review summarizes the current understanding of lethal and sublethal trauma to red blood cells (RBCs) produced by the exposure of blood to flow parameters and conditions similar to MCS.

1.2.1 Introduction

Whole blood is a complex, heterogeneous, multi-cellular suspension, the importance of which cannot be overstated. Blood is responsible for gas exchange, nutrient transport, waste removal, cell signaling, immunomodulation and immunoprotection, wound healing, and overall homeostasis. The cellular (~45%) and plasma (~55%) components of blood, while distinct, are interdependent and essential for maintaining proper functions. The phenomenon of mechanical blood trauma arises from the exposure of flowing blood to non-physiological conditions found within MCSDs, summarized concisely as “too many non-physiological factors affecting too many physiological objects.” Although yet to be identified or discovered. These objects include blood cells (erythrocytes/RBCs, platelets, leukocytes) with various functions, cell volumes, rheological properties, life spans, and population sizes and other numerous components inside

blood plasma, like proteins (albumin/globulins), blood coagulation factors, immunoglobulins, nutrients, minerals, salts, ions, and hundreds of other dissolved constituents. The most common nonphysiological factors are mechanical stresses, excessive temperatures, turbulence, cavitation, flow rates, the presence (or absence) of flow pulsatility, incompatible foreign surfaces, etc. Inside a MCSD, these factors may act independently, collectively, or synergistically. All cellular species of blood are sensitive to these factors and can be activated, deactivated, or irreversibly damaged. Furthermore, many plasma components may be denatured due to exposure to MCSDs.

Healthy, human denucleated red blood cells (RBCs) have the longest life span in circulation (100-120 days), maintaining an intravascular population of about 5.1 ± 1.0 million/mm³ of blood or approximately 40% to 45% of blood volume [24]. Due to their remarkable deformability, RBCs with size of $\sim 8 \mu\text{m}$ are able to easily enter and pass through blood capillaries with diameters as small as $3 \mu\text{m}$. Best known for gas transport, they are also essential to the dynamic, non-Newtonian rheological properties of blood which provide adaptive viscosity in various compartments of the vascular system. This is in turn responsible for the vessel wall shear stresses that affect endothelial function. Healthy platelets are $2 \mu\text{m}$ to $3 \mu\text{m}$ in size, with an *in vivo* life span of about 10 days and a concentration of 0.15 to 0.45 million/mm³ of blood. Their major function is to prevent and stop bleeding by creating plugs/clots involving the very complex coagulation cascade. As a key component in hemostasis, platelets are extremely sensitive to the factors listed above leading to their activation, aggregation, deposition, or dysfunction. Due to exposure to non-physiological environments, activated platelets may create microthrombi in the MCSD that can cause the device to fail and/or create emboli, potentially blocking blood flow to vital organs. Standard practice to temper the risk of MCSD thrombogenicity is to administer anticoagulant or antiplatelet therapies directly into the blood

intravenously (e.g.: heparin, bivalirudin) or indirectly enterically (e.g.: warfarin, clopidogrel, acetylsalicylic acid [asprin], etc.), an intervention that raises the risk of unintended bleeding. Consequently, coagulopathy related complications (including bleeding, thromboembolism, neurological dysfunction, and pump thrombosis) are the leading cause of adverse events in patients on mechanical circulatory support [16]. Therefore, the reduction of blood damage remains a major challenge for developers of blood-contacting devices.

Over many decades, there have been an abundance of studies on blood damage to understand, reduce, and eliminate complications related to blood-contacting foreign surfaces and non-physiological flow conditions. The best known, easily detectable, and reproducible marker of *in vivo* or *in vitro* blood trauma is *hemolysis*, which is manifested by hemoglobin released from ruptured, overstretched, overheated, or prematurely aged RBCs, or some combination thereof. Numerous publications are dedicated to the *in vitro*, *in vivo*, and computational investigations of the fluid dynamic and microenvironmental conditions in MCSDs leading to device-induced hemolysis and the consequences of plfHb in blood. Despite considerable efforts by device developers to mitigate the risk of blood trauma, a significant increase in hemolysis takes place preceding the diagnosis of pump thrombosis. This phenomenon is associated with substantial morbidity and mortality of MCSD recipients, which is now increasingly reported [25-27]. Sublethal trauma, which is difficult to detect and characterize compared to hemolysis, has yet to be extensively examined. Even mild hemolysis *in vivo*, which is not an abrupt threat to renal function, can be a harbinger of potential ongoing damage to other blood components (including platelets, white blood cells, von Willebrand factor, etc.), which can cause or indicate serious complications like thrombosis. Therefore, it is important to assess the susceptibility of blood to sublethal trauma or possibly the extent of sublethal damage incurred to serve as an early

diagnostic marker. While there are many questions regarding what tests could predict complications, unfortunately no machine or single experiment exists that can measure both lethal and sublethal injury in a MCSDs patient's blood. Acknowledging the breadth and depth of sublethal blood damage, this subchapter will primarily focus on sublethal trauma to RBCs including the mechanisms of damage, the resulting physiological changes, and the consequences of pathological erythrocytes.

1.2.2 Hemolysis

Extensive experience with heart-assist devices has demonstrated that they have the propensity to damage blood to some extent. Therefore, special attention must be paid to the prediction and reduction of blood damage when designing, testing, and clinically operating MCSDs. The prolonged contact and collision between blood cells and foreign surfaces, cavitation, excessive exposure to high fluid stresses, and turbulence may cause the complete mechanical destruction of RBCs. These factors can also denature proteins, activate platelets and leukocytes, elevate inflammatory mediators, cause complement activation, and change the mechanical properties of red blood cells akin to accelerated aging [28-33]. The inverse relationship between the magnitude of shear stress and length of exposure time on hemolysis, first summarized by Leverett *et al*, has remained an active area of interest since the inception of MCS [34]. The eponymously named "Leverett curve", a quantitative description of the hemolytic threshold as a function of shear stress and exposure time, is thus the primary driver for designers of any non-static, blood-contacting medical device [35]. This is especially relevant as the evolution of RBPs towards 3rd generation (bearing-less) devices has resulted in lower peak shear stresses albeit with longer exposure times due to recirculation with specific suspension modalities [36-40].

Hemolysis manifests clinically as anemia, fatigue, jaundice, hematuria, and kidney failure, among many other symptoms [41]. In addition to renal damage, mechanical hemolysis can cause hypercoagulation, bleeding, thromboembolism, and neurologic dysfunction (stroke, altered mental status, etc.) [28, 30, 42]. Even low levels of hemolysis have been shown to drastically increase RBC aggregation at low shear conditions [43]. Additionally, the release of hemoglobin from the overstretched RBCs into the plasma may have a toxic effect on the cardiovascular system due to its ability to bind nitric oxide, an endothelium-derived relaxing factor, leading to vasoconstriction, hypertension, renal damage, and platelet activation [44]. By the end of the 19th century, it was already recognized that hemolysis promotes intravascular thrombosis [45]. Experiments using stroma-free RBC lysate revealed that a hemoglobin concentration as low as 30 mg/dL induced spontaneous platelet aggregation, which increased in direct proportion to the concentration of lysate [46].

1.2.3 Sublethal RBC Damage

For many decades, it has been observed that the mechanical properties of RBCs could be altered during prolonged exposure to shear stresses well below the hemolytic threshold [29]. The concept of *sublethal RBC damage* was first introduced by PM Galletti (a pioneering researcher in artificial organs and tissue engineering), who attributed the observed development of anemia and shortened RBC life spans in animals that underwent extracorporeal perfusion for 10 to 48 hours to a process of ongoing sublethal blood trauma [47]. Additional studies by Bernstein *et al* and Indeglia *et al* confirmed this relationship between subhemolytic shear stresses during assisted circulation and the premature removal of damaged RBCs, eventually leading to postperfusion anemia [48-50]. This sublethal trauma is much harder to detect and characterize than total lysis.

The experiments of Sandza *et al*, where isolated rabbit spleens were perfused by a mixture of sheared and non-sheared autologous RBCs, proved that the spleen could “recognize” and selectively remove cells that had been exposed to shear stresses lower than 10 Pa for 2 hours, suggesting that some changes had occurred to the mechanical or chemical properties of the RBCs [51]. Clinically observed, chronic anemia in patients supported with MCSs is sometimes attributed to undetermined mechanisms [52]. However, it might directly result from the sublethal RBC damage and lifespan shortening as described by Galletti *et al*. This is corroborated by previously published clinical data on anemic patients with circulatory support devices and heart valves that showed alterations in patient blood rheology such as increased blood viscosity, RBC aggregation, and decreased RBC deformability [52-55]. Moreover, an increasing occurrence of thrombosis and inflammatory events without measurable hemolysis may be unknowingly triggered by sublethal damage to blood, as it is not yet a part of clinical practice.

RBC Deformability

RBC deformability is critically important for the passage of these cells through the entire vascular system, including the smallest capillaries in microcirculation, to provide adequate transport of gases, sufficient supply of nutrients, and efficient removal of waste products. It has been found that naturally aged RBCs are removed from circulation by the spleen as they become less deformable [56]. Each single RBC enters the spleen about twice per hour where it is “tested” for the ability to pass through tiny slits in the red pulp. The body applies this built-in “rheometer” to measure RBC deformability and remove those that fail this examination. Therefore, the deformability of RBCs appears to be the major determinant of their survival in the vascular system, and hence, their lifespan. RBCs exposed to extensive mechanical stress can therefore be prematurely removed from circulation because of an increase in their rigidity. In this context,

sublethal trauma may be considered analogous to an accelerated RBC aging process. Healthy RBCs are able to enter and pass through much smaller capillaries, thus decreasing blood viscosity 5 to 6 times below that of blood containing rigid RBCs [57]. Impairment of RBC deformability reduces the number of functioning capillaries due to RBC exclusion, inducing tissue ischemia. The decrease in RBC deformability after exposure to mechanical stress has been reported in many studies [58-64]. Baskurt *et al* illustrated this phenomenon by subjecting human RBCs to a uniform shear stress of 120 Pa for 15 to 120 seconds at 37°C. This level of stress significantly impaired RBC deformability as assessed by ektacytometry, with no visible hemolysis observed in the sheared RBC suspensions [61]. Kameneva *et al* demonstrated that the reduction of RBC deformability induced by mechanical stress was worsened when combined with hypothermia and a decrease in plasma protein concentration due to hemodilution, especially in cases of moderate and deep hypothermia widely applied during cardiopulmonary bypass in infants [58]. Dao *et al* found a reduction of human RBC filterability accompanied by significant changes in the RBC lipid bilayer due to exposure of RBC suspensions to sublethal shear stress of 100 Pa for 120 seconds [65].

There are various methods for the assessment of RBC deformability described in the literature including but not limited to micropipette aspiration, filtration, viscometry, and imaging-based modalities [66]. Ektacytometry, a common imaging-based technique, uses laser diffraction analysis to assess cellular deformation in low hematocrit RBC suspensions under shear [67]. These authors prefer to assess RBC deformability with bright-field illumination instead, enabling direct visualization of cell shape, using the Linkam Optical Shearing Stage (CSS-450; Linkam Scientific Instruments) [59]. The apparatus consists of a parallel disc sample chamber with an adjustable height top plate (typically 10-20 μm) and rotating bottom stage. RBC

samples are suspended in a concentrated polyvinyl pyrrolidone (PVP) solution ($\mu = 30$ cP or mPa·s) and exposed to Couette flow at various shear rates while simultaneously observed using a synchronized CCD camera (QICAM Fast Color, QImaging). The resulting images are then analyzed to quantitatively determine cell deformability using ImageJ (NIH) or automated software to yield an Elongation Index calculated as $(L-W)/(L+W)$, where L is the length and W the width of the RBC under shear. A representative image produced by the Linkam System is shown in **Figure 1**, where a mixture of normal and rigidified RBCs was sheared at (A) 0 and (B) 1000 s^{-1} (corresponding to a shear stress of 0 and 30 Pa, respectively).

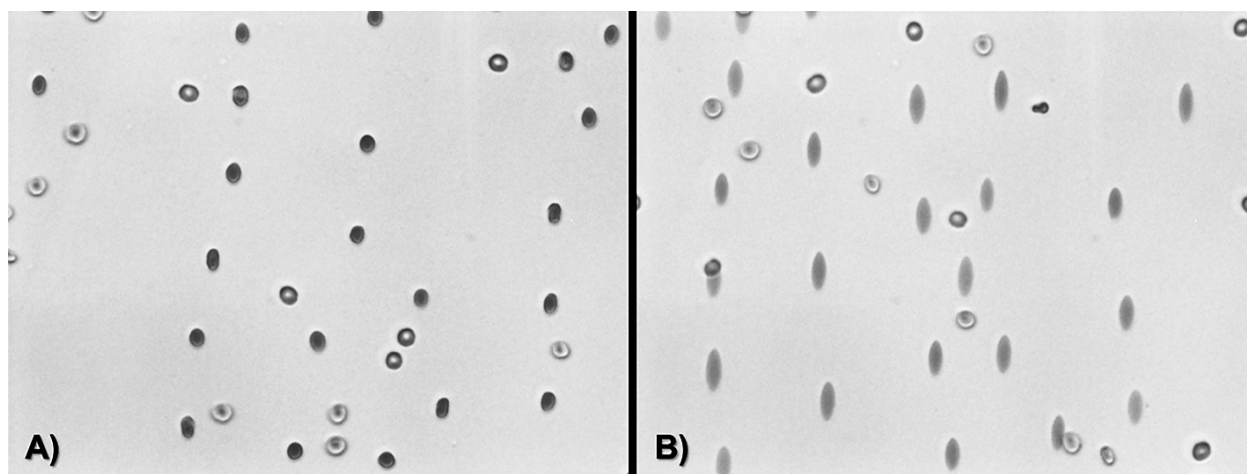


Figure 1. Bright-field illuminated normal and rigidified erythrocytes undergoing shear using the Linkam Shearing Stage. Assessment of RBC deformability at (A) 0 and (B) 1000 s^{-1} shows normal RBCs elongating and becoming ellipsoidal under shear stress while the rigid cells remain circular.

RBC Aggregation

The RBCs of human and some other mammalian species, especially active versus sedentary ones such as a horse, feline and antelope, build aggregates that can be observed in blood *in vitro* and *in vivo* under no flow or low flow states [68]. RBC aggregation is caused by fibrinogen and other large protein molecules in blood plasma. The physiological significance of RBC aggregation is

not yet fully understood, but it has been shown to promote the development of a cell-depleted plasma layer near walls of small blood vessels, thereby reducing wall shear stress loading and diminishing the release of endothelium-dependent vasodilators [69]. A drastic increase in RBC aggregation at low flow conditions has been seen even at low levels of hemolysis [70]. Furthermore, it is known that an increase in RBC aggregation relative to normal physiological levels is associated with inflammation, infection, or some other pathological states; which is usually related to an increase in the concentrations of plasma fibrinogen, immunoglobulin, and other plasma macromolecules [71, 72]. The majority of preclinical animal studies for MCSs are performed in ruminants because of their acceptable size, docile behavior, long-term manageability, and cost effectiveness [73]. Despite a relatively high physiological concentration of fibrinogen for bovines (up to 0.5-0.8 g/dL), ovines and bovines typically exhibit no RBC aggregation. Nevertheless, it was possible to observe aggregation of RBCs in bovine blood during MCSs implantations as shown in **Figure 2** [74]. **Figure 2-A** is a micrograph of blood from a MCS-implanted animal with a fibrinogen concentration of 1.0 g/dL showing a very strong aggregation of RBCs. Due to a typical postsurgical reaction after MCS implantation, these animals exhibited increased fibrinogen levels. **Figure 2-B** shows blood of a control calf with no tendency for RBC aggregation. When RBCs of this normal calf (**B**) were resuspended in the plasma of the implanted calf (**A**), they still did not show any tendency to aggregate (**C**). However, RBCs of the MCS-supported calf (**A**) re-suspended in the plasma of the control calf (**B**) began aggregating (**D**) even at the much lower fibrinogen concentration of 0.2 g/dL in plasma. The same phenomenon was reported during testing of MCS-implanted ovines [75]. These observations support the hypothesis that sublethal mechanical stress increases RBC aggregability, perhaps via decreased membrane sialic acid concentration and cell surface

negative charge, which normally creates repulsing forces between RBCs [64, 76-78]. While the difference in RBC aggregation behavior in these preclinical models should be noted, the abnormal aggregation of ovine or bovine erythrocytes may serve as an indicator for sublethal blood trauma during MCSD testing. RBC aggregation is of basic scientific and clinical interest, with a number of reports associating a strong increase in this parameter to multiple pathologies, and a variety of experimental studies aimed at finding and testing drugs that are able to reduce RBC aggregation. Yet the advantages and disadvantages of having low or no RBC aggregation are not clear. A significant increase in RBC aggregation from MCSD-induced sublethal mechanical blood damage could affect patient microcirculation by increasing the near- wall cell-free layer, allowing more platelets and leukocytes to concentrate near the vessel wall. This in turn, may promote inflammation (due to excess leukocytes) and thrombosis (due to excess platelets), which are major complications of mechanically assisted circulation.

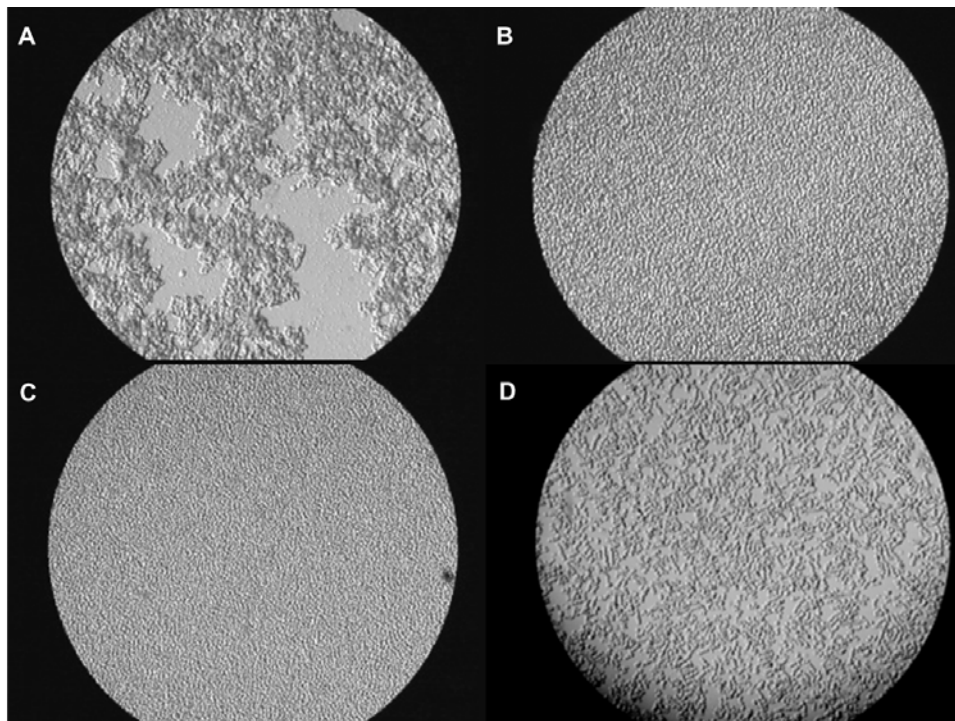


Figure 2. Bovine RBC aggregation under Bright-field illumination. (A) Blood of a calf implanted with a MCSD (high RBC aggregation and high plasma fibrinogen concentration); (B) Blood of a control calf (no RBC

aggregation and low fibrinogen concentration); (C) Control RBCs placed in the MCSD animal's plasma (no RBC aggregation at high fibrinogen concentration); and (D) MCSD calf RBCs placed in the control calf plasma (high RBC aggregation despite low fibrinogen concentration). The aggregation present in frames (A) and, especially, (D) indicate that there are RBC-specific changes directly induced by mechanical stress related to MCSD support. Reprinted with permission from IOS Press [74].

There are several methods used for evaluating RBC aggregation, namely, photometric techniques based on alterations of light reflectance or transmittance of RBC suspensions during the process of cell aggregation using special aggregometers (e.g., Myrenne Aggregometer or RheoScan) [79]. In addition, RBC aggregation can be assessed using low-shear blood viscosity and erythrocyte sedimentation rate (ESR) parameters [80]. Since the concentration of RBCs strongly affects the results of any aggregation measurement, the hematocrit of the blood sample should be always adjusted to a "standard" value (traditionally, 40% for most methods).

Mechanical Fragility of Red Blood Cells

The sensitivity of RBCs to mechanical stress is one indicator toward the extent of sublethal damage to blood. A sensitive method to assess the mechanical fragility (MF) of RBCs is the *Rocker-bead MF test* [81], which could be used during MCSD support to warn of blood damage preceding measurable hemolysis [82]. A corresponding *Mechanical Fragility Index* (MFI) is calculated by measuring the amount of free hemoglobin generated after blood vials containing stainless steel ball bearings are subjected to a defined amount of mechanical stress by rocking at specific parameters for a controlled period of time [81, 83, 84]. The Rocker-bead MF test was found to be a practical, straightforward, and reproducible way to determine changes in RBC susceptibility to mechanical stress related to aging, excessive exposure to mechanical stresses, or disease states. It is worth noting that RBC mechanical fragility in human neonates was found to

be higher than that in adults [85]. In all tested adult species, younger RBCs (less dense) were found to be less fragile than senescent RBCs (more dense) as sorted by density [64, 86]. This test also has demonstrated that RBCs from blood obtained from premenopausal women were significantly less susceptible to shear stress-induced hemolysis compared to those obtained from age-matched males due to RBC turnover from the menstrual cycle [87]. The Rocker-bead MF test has also been applied to compare mechanical blood damage produced by cell salvage suction devices and more recently was used for evaluating sublethal RBC injury induced by Blood Bank storage [88, 89]. While there was no significant difference in MF observed between ABO groups, there was a strong increase in RBC fragility proportional to storage time. In the same study of the Blood Bank-stored donor RBCs, the cells were tested for potential changes in their rheological properties using a viscoelasticity analyzer (Vilastic-3; Vilastic Instruments). All stored RBC suspensions demonstrated a progressive increase in viscosity and cell rigidity at equivalent shear rates over 7 weeks of storage, indicating a significant decrease in RBC deformability over that period of time [89, 90]. The clinical effects of storage time on donor RBC units, including cell membrane changes, decreased oxygen deliverability, and increased oxidative species – termed RBC *storage lesion* – is well established [91, 92].

Because of the dependence of the Rocker-bead MF test results on RBC concentration, any comparison between groups or time points requires the adjustment of the sample hematocrit to a “standard” value before testing as performed in the studies presented above [89, 92]. Further work to improve the test by Ziegler *et al*, including eliminating the additional time for hematocrit normalization and significantly reducing the blood volume requirement [93], was accomplished in conjunction with this dissertation and is included in **Appendix A**. The proposed reduced

volume Rocker-bead MF test and accompanying modified MFI (MMFI) now has the potential to become an important scientific and possibly clinical hematological parameter [23, 93].

1.2.4 Factors Affecting RBC Mechanical Trauma

Several studies have demonstrated potential ways to reduce mechanical blood trauma caused by MCSD using biocompatible and rheologically active additives to blood [61, 94-97]. Kamada *et al* used albumin additives to the priming solution during extracorporeal circulation in patients undergoing coronary bypass surgery to prevent erythrocyte crenation, thus improving RBC deformability. This modification of the procedure also improved microcirculatory flow in patients undergoing open heart surgery [94]. It is important to note that current circuit priming strategies, especially in pediatrics, remain unsettled over the use of albumin, synthetic colloid suspensions, packed RBC units, fresh frozen plasma (FFP), or some combination therein, due to clinical concerns of hemodilution, inflammation, bleeding, and cost effectiveness [98-102]. Though as indicated in this review, sublethal mechanical blood trauma likely plays a role in some of these complications. Armstrong *et al* demonstrated that the nonionic surfactant poloxamer-188 (RheothRx) protected RBCs from damage caused by mechanical stress and reduced leakage of ADP from RBCs, thus potentially inhibiting ADP-induced platelet aggregation. The authors proposed that nonspecific adsorption of copolymer to the RBC surface via the hydrophobic polyoxypropylene moiety was responsible for shielding them from mechanical damage. RheothRx injection has subsequently been shown to effectively treat acute ischemic disorders such as myocardial infarction [95].

Various plasma proteins have likewise demonstrated protective effects on RBC mechanical damage [96]. In these studies, bovine cells suspended in various solutions were

simultaneously exposed to the same mechanical stress using the standard RBC Rocker-bead MF test in experiments performed at room temperature with controlled osmolality and viscosity of the suspension media. The lowest hemolysis was obtained for RBCs suspended in serum, plasma, and albumin solutions; while hemolysis in phosphate buffered saline (PBS) or in dextran (Dextran-40) suspensions was over 3 times greater than in plasma ($p < 0.001$). The presence of relatively small amounts of plasma (30%) in PBS media significantly ($p < 0.001$) decreased mechanical hemolysis compared to RBCs suspended in PBS only. The clinical significance of these results is that a decrease in the concentration of plasma proteins due to hemodilution may elevate blood damage during extracorporeal circulation [96]. Protective effects of a 4%-modified fluid gelatin solution and a 4% albumin solution on blood bank-stored RBC exposed to mechanical stress has been reported by Sumpelmann *et al* [103]. A similar protective effect was demonstrated by replacement of 20% of blood plasma with a perfluorochemical-based blood substitute in *in vitro* experiments, promising improvement in blood oxygenation as well [97]. An additional benefit of this additive was a decrease in low shear viscosity and erythrocyte sedimentation rate, both related to the ability of the perfluorochemical emulsion to reduce RBC aggregation. Finally, a significant reduction of mechanical hemolysis was observed in suspensions of bovine RBCs in autologous bovine plasma and/or polyethylene glycol (PEG ~20,000 MW; Sigma) compared to Dextran-40 (40,000 MW; Sigma) and PBS as shown in **Figure 3** [23, 104]. Therefore, in summary there are both biochemical and mechano-physical considerations towards the use of specific molecular additives or products in the protection of erythrocytes against mechanical hemolysis.

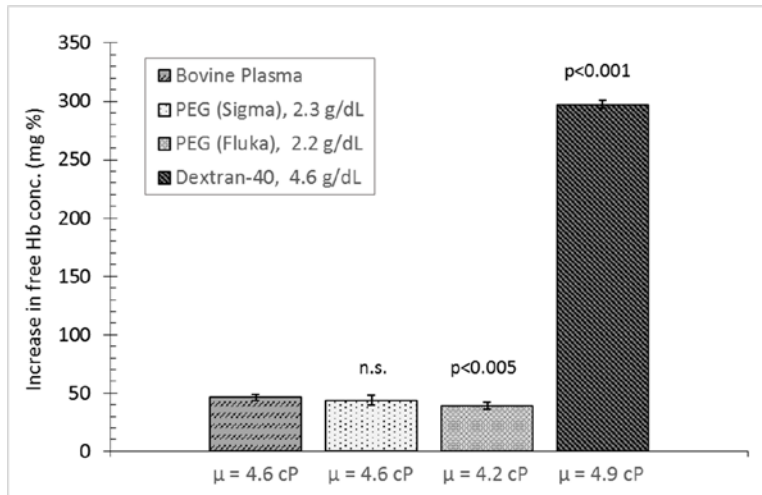


Figure 3. Effect of suspension media with matched viscosities on bovine RBC mechanical fragility; highlighting the protective effects of plasma proteins and PEG versus Dextran-40 solution. Data from Kameneva *et al* [104], and reprinted with permission from WICHTIG [23].

1.2.5 Sublethal RBC Damage Effects on Platelets

Exposure of platelets to supraphysiological mechanical stress can cause their activation and eventual dysfunction with far-reaching implications [105-109]. However, in addition to hemolysis-induced platelet activation, there is growing evidence that sublethal erythrocyte damage promotes platelet activation as well. The potential loss of smaller molecules such as ATP and 2-3diphosphoglycerate (2-3 DPG) through 10 Å to 20 Å micropores in stretched RBCs was described by Sutera [29]. Alkhamis *et al* followed with a study that found a 2% release of ADP, from RBCs under shear, induced platelet aggregation *in vitro* [110]. The leakage of these platelet activating factors was also found after short exposure times of blood in extracorporeal systems [29, 111].

In addition to the agonistic effects from the release of intracellular RBC contents, there is a rheological aberration that contributes to platelet activation and behavior [112]. For example,

alterations in RBC deformability may modify their effect on platelet transport to boundary walls [113-115]. Using chemically-modified RBCs to change deformability, Aarts *et al* showed an increase in platelet adhesions with increasing RBC rigidity within isolated arteries *in vitro* [116]. This was corroborated in a follow-up, double-blind, clinical, *in vivo* study using isoxsuprine, a vasodilator found to increase erythrocyte deformability, which supported the previous findings that increased RBC deformability reduces platelet-wall interaction and adhesion [117]. The results of computational simulations demonstrated that at a wide range of shear rates and hematocrit values, the rate of platelet adhesion is mainly limited by the frequency of their near-wall rebounding collisions with RBCs [118]. These findings suggest that to examine and address thrombotic complications without the consideration of the rheological and biochemical influence of erythrocytes may be a gross oversimplification and should not be overlooked when investigating thrombosis in MCSDs.

1.2.6 Blood Transfusions in MCS

First-generation, pulsatile-flow ventricular assist devices and now continuous-flow, rotary blood pumps have broadened the availability of MCSDs for adult patients with heart disease. While mechanical circulatory support has been gaining acceptance, there are growing reports of MCSD-associated complications that require consideration including device thrombosis and nonsurgical bleeding [16, 26, 27, 119-124]. Due to “first-in, first-out” policies to minimize waste, packed RBC units given to patients within the United States are typically close to their maximum storage duration limit (average 42 days) as dictated by the Food and Drug Administration (FDA). Since collected erythrocytes already have an age distribution before subsequently spending one-third of their lifespan deteriorating *ex vivo*, it is unsurprising that a

25% loss of donor RBCs within 24 hours of transfusion, while physiologically taxing, is still considered clinically acceptable [125, 126]. The potential consequences of administering blood products (e.g., inflammation, allosensitization, pulmonary hypertension, right heart failure, hepatic congestion, coagulopathy, and mortality) are well established, but acute and chronic postoperative transfusions remain prevalent for MCSD-implanted patients [124, 127, 128]. Although bleeding is unavoidable from surgical insult, one center reported an average packed RBC transfusion rate after implantation of 5.7 units per patient overall with an upper limit of 120 units [129]. Understanding that there is a significant increase in the mechanical fragility of stored Blood Bank RBCs and the results of mechanical stress from MCSDs, one can question the utility of transfusing MCS patients only for these cells to lyse, be prematurely removed by the spleen, and unable to improve microcirculation.

1.2.7 Conclusions

With current technology, there is no way to completely avoid mechanical damage to blood cells produced by MCSDs. However, the negative impact produced by mechanically damaged blood cells on organ and tissue functionality necessitates the need continually strive to minimize the complications associated with MCS. In summary, the rheological and biochemical impact of blood trauma should not be overlooked when investigating thrombosis, hemolysis, or anemia in MCSD patients. Though mechanical trauma in blood pumps is commonly categorized as either erythrocyte destruction or coagulopathy centered, the interdependence of all blood and blood flow components must be kept in mind during the design, development, and use of MCSDs.

1.3 THE PEDIAFLOW® PEDIATRIC VAD

While there continues to be a need for next-generation pediatric MCS technology, the small market potential has limited commercial interest. Driven by the lack of progress for this underserved population, the National Heart, Lung, and Blood Institute's (NHLBI) Pediatric Circulatory Support Program (PCSP) awarded over \$22 million in 2004 to fund five separate consortia towards the development of novel pediatric MCS devices [7]. As a follow on to this initiative, in 2010 NHLBI launched the Pumps for Kids, Infants, and Neonates (PumpKIN) – Pre-Clinical Program and awarded four contracts (\$24 million) to support four pre-clinical efforts (three for pediatric devices funded under PCSP) to gain Investigational Device Exemption (IDE) from the FDA [130]. The PediaFlow® Consortium, consisting of the University of Pittsburgh, Children's Hospital of Pittsburgh, Carnegie Mellon University and LaunchPoint Technologies™ (Goleta, CA), received an award in both NHLBI Programs.

1.3.1 Development and Evolution

As a participant in both NHLBI programs, the PediaFlow® Consortium designed an implantable, mixed flow, fully magnetically levitated (maglev), rotodynamic VAD to support the smallest (BSA $<0.5 \text{ m}^2$ with a cardiac index $>3.0 \text{ L/min/m}^2$) and most vulnerable patients (due to their large numbers and lack of any device) for durations consistent with bridge-to-transplant wait list times, with the objective of minimizing MCS-associated serious adverse events [5, 131]. From the first prototype (PF1) demonstrating the feasibility and biocompatibility of a *de novo*, mixed-flow (or “diagonal”) maglev pump, the developmental evolution and miniaturization of the PediaFlow® pediatric VAD summarized in **Figure 4** involved the implementation of

turbomachinery principles outside of the usual operating ranges. [132-134]. Designed to run at supercritical speeds (RPMs above resonance frequencies), the 3rd generation PediaFlow® (PF3) demonstrated excellent biocompatibility *in vivo* but was unable to achieve target flow rates due to rotor (impeller) instability precluding operation at uppermost pump speeds [134, 135].

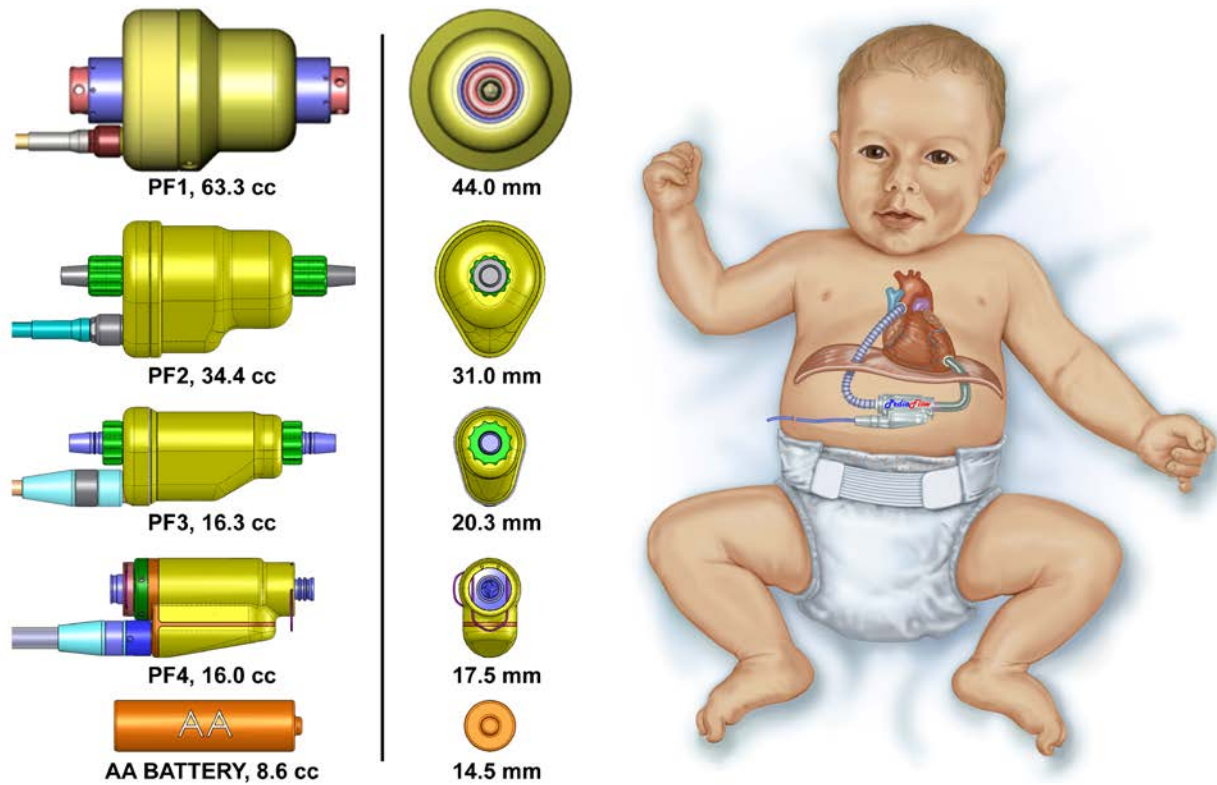


Figure 4. Evolution and miniaturization of the PediaFlow® from the first prototype (PF1) to the 4th generation (PF4) pediatric VAD.

1.3.2 PediaFlow® 4th Generation (PF4)

Intended to provide up to six months of circulatory support for patients between 3 to 15 kg at flow rates of 0.3-1.5 L/min, the 4th generation PediaFlow® pediatric VAD (PF4) is the result of over 10 years of biomedical, mechanical, electrical, and computational engineering (**Figure 5-**

A). Representing the final/frozen pump topology design, the PF4's optimized blood-flow path consists of a tapered cylindrical impeller with four blades on the conical inlet face, leading to a single 1.5 mm annular fluid gap region, before passing through a three vane flow straightener machined into the aft-housing upon exit (**Figure 5-B**) [135]. By increasing the voice (levitation) coil to motor stator size-ratio and optimizing the impeller blading, but otherwise similar to the PF3 design, the PF4 was able generate higher flows over greater pressure heads to reach the target design goals. Integrated 'quick-connect' coupling mechanisms, recessed within the housing, enable direct attachment to the pump inlet and outlet. Approximately the size of AA battery, a decrease in size of almost 75% from the initial PF1 prototype (**Figure 5-C**), the PF4 is intended to be fully implantable in infants as small as 5 kg through placement behind the left rectus abdominus muscle with a single percutaneous driveline for electrical power.

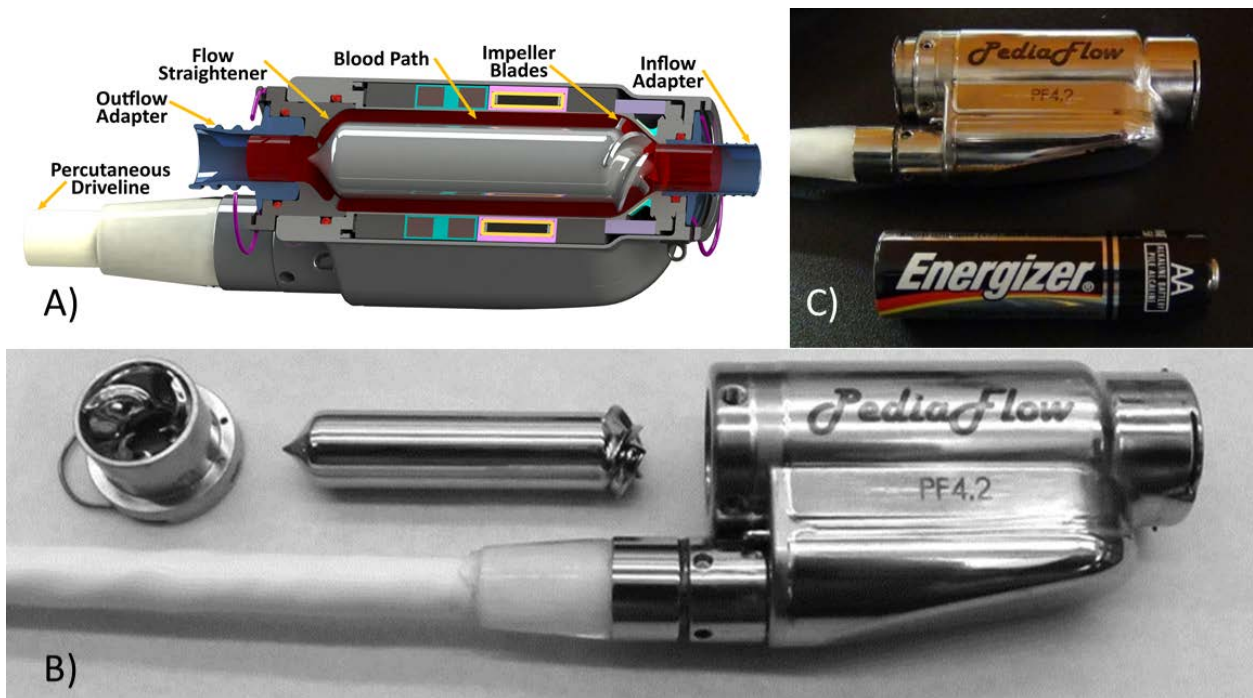


Figure 5. The PediaFlow® PF4 prototype and implantable components. **A)** The PF4 pump topology, **B)** the disassembled pump showing the stator, rotor, and housing, and **C)** size comparison to an AA-size battery.

Benchtop evaluation of the PF4 to confirm hydraulic performance *in vitro* was performed by measuring pump flow rate and pressure differential in a closed flow loop using a 2.39 centipoise (cP) blood analog glycerol-solution at room temperature to generate characteristic pump ‘H-Q’ curves following previously published methods [132]. The characteristic performance curves of the PF4 highlighted an expanded operating range between 0.3 to 2.0 L/min at physiologically relevant pressure ranges in contrast to PF3 (**Figure 6**).

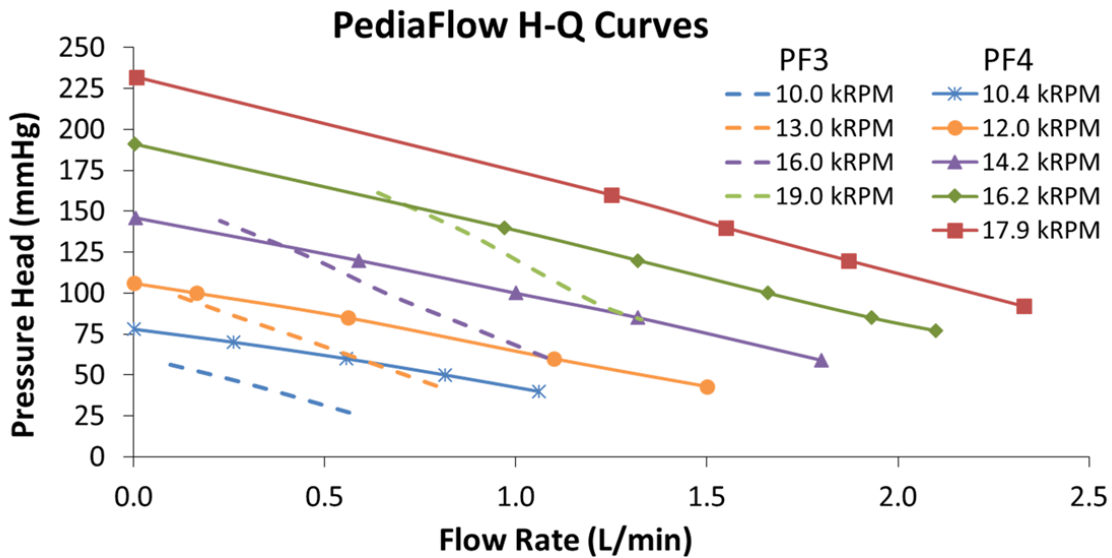


Figure 6. Characteristic H-Q pump curves of PF3 and PF4 using a blood analog (viscosity = 2.39 cP).

1.4 OBJECTIVES

The overall goal of this research is to facilitate the translation of next generation, pediatric blood pumps from the bench top to the bedside by developing the framework to enable precise testing, optimal patient coupling, and accurate device diagnostics.

The development and success of these next-generation devices are contingent on several areas that have remained unaddressed. The lack of a standardized practice for the *in vitro*

assessment of pediatric MCSDs prevents intra- or inter-consortium comparisons [37, 136]. Equally important to RBP performance are the cannulae used to connect the device to the patient's heart and great vessels, with a broad analysis required to determine a pediatric-appropriate design [137-139]. Finally, there is no comprehensive, encompassing, off-the-shelf data acquisition platform that can serve to record pump parameters while providing alarm monitoring, real-time flow estimation, and diagnostic support services during preclinical testing.

Towards this end, this dissertation describes the work and effort, in part, resulting in the optimized PediaFlow implantable system of today.

Objective #1: Design, optimize, and validate new standards of practice for the *in vitro* measurement of mechanical blood trauma in pediatric blood pumps.

Appropriate testing parameters and guidelines characteristic of pediatric patients was determined in order to accurately simulate *in vivo* operation on the bench top through the analysis of literature and hemorheological examination. A pediatric mock loop was optimized to enhance blood mixing, minimize blood damage unrelated to the tested device, and maximize reproducibility of the pump tests. The developed standards were used in the *in vitro* hemolysis assessment of the PF4 prototypes and the previously tested and clinically approved Thoratec® PediMAG® (Pleasanton, CA) extracorporeal blood pump for validation.

Objective #2: Evaluate the performance and suitability of an inflow cannula design for use with pediatric rotary blood pumps.

Based on preliminary *in vivo* findings, a tailored approach was taken to verify and validate the inflow and outflow pathways used to connect the pediatric pump. A new inflow cannula was designed and evaluated against previous iterations to examine pressure losses, ventricle unloading, positional sensitivity, and resistance to ventricular suction.

Objective #3: Develop a comprehensive Diagnostic Support System (DSS) for *in vivo* preclinical testing of the PediaFlow® pediatric VAD.

The purpose of the DSS platform is to provide a straightforward user interface, enhanced data logging capability, complex real-time flow estimation, advanced alarm detection, basic resolution suggestions, and remote monitoring capabilities. Software architecture, data flow, and front panel layout was designed based on maximizing computation efficiency, redundancy, and usability. A flow estimation algorithm for the PF4 was developed from pulsatile mock-loop testing and implemented within the platform. The DSS iterations were implemented, evaluated, and improved “just-in-time” in conjunction with, and in support of on-going PF4 *in vivo* implant studies.

2.0 IN VITRO ASSESSMENT OF MECHANICAL BLOOD TRAUMA IN PEDIATRIC BLOOD PUMPS

The characterization of blood damage is essential for the development and regulatory approval of any blood-contacting medical device [140, 141]. While computational fluid dynamics (CFD)-simulations are used extensively during the design process of MCS devices and preclinical *in vivo* animal studies are considered the conclusive indicators for the biocompatibility, *in vitro* benchtop testing remains integral as both cost-effective and a requirement for demonstrating safety [36, 142].

2.1 INTRODUCTION

2.1.1 Benchtop Hemolysis Testing

A crucial component to the development of any mechanical circulatory support device is preclinical *in-vitro* hemolysis testing. Multiple publications have served as de-facto guidelines for examining full-support adult RBP, yet continued variability in blood preparation, experimental procedures, and reported results makes comparisons between devices or even laboratories impossible. As noted by Herbertson *et al*, the reported hemolysis results for the same pump at similar operating conditions can vary by two orders of magnitude [84, 143, 144]. The

ASTM F1841 standard is often cited for adult VADs tested at 5 L/min, however the priming loop volumes reported have varied from the suggested 450 ± 45 mL to 600 mL and even 1000 mL of blood [144-147]. It is apparent that the application of these guidelines would be inappropriate when evaluating RBPs for pediatric patients (<20 kg) at flow rates below 2 L/min with much lower total circulating blood volumes, yet literature remains sparse on the testing of pediatric- or partial- support devices.

2.1.2 Previous PediaFlow® Testing

In vitro hemolysis testing for the 1st thru 3rd generation PediaFlow® prototypes utilized a horizontally oriented flow loop using off-the-shelf, commercially-available components [132, 134, 148] as shown in **Figure 7-A**. Initial concerns with stagnation due to extraneous ports, low test flow rates, and disproportionate blood priming-volume requirements led to the use of a magnetic stir plate under the blood reservoir to promote mixing (**Figure 7-B**).

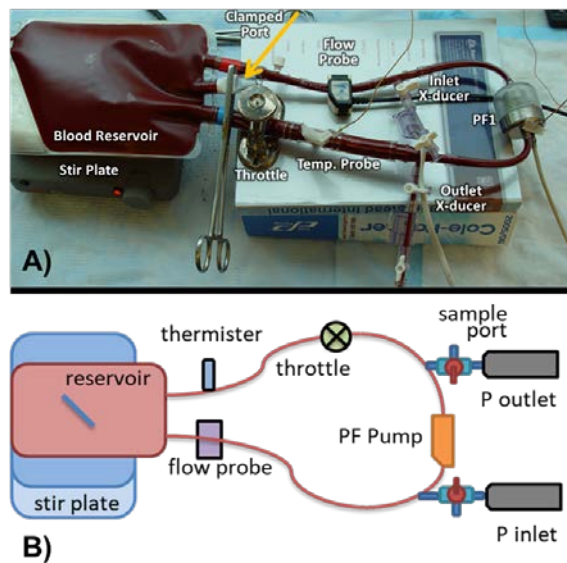


Figure 7. A) Benchtop hemolysis testing of the 1st generation PediaFlow®, and B) top view schematic of the *in vitro* mock loop for the PF1-PF3 prototypes utilizing a magnetic stir plate.

As the standard of practice is to use vertically-oriented flow loops to prevent artificial hemolysis from cavitation or outgassing (**Appendix A**), an attempt was made to increase hydrostatic preload during the testing of the PF3 by elevating the reservoir with respect to the pump with negligible results (**Figure 8**) [144, 149].

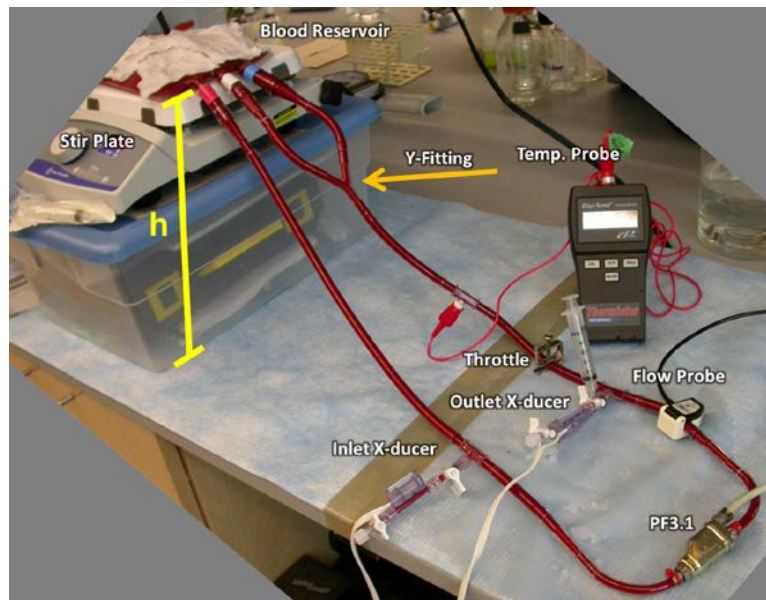


Figure 8. The elevated reservoir and magnetic stir plate during *in vitro* testing of a PF3 prototype pump.

Overall, the existing practice for *in vitro* hemolysis testing of pediatric RBPs was far from ideal. The addition of the magnetic stir bar, a source of shear stress and additional hemolysis (as evidenced by the resultant), now requires the use of an appropriate control to isolate and quantify only MCSD-induced hemolysis. The lack of standard operating procedures led to variable experimental setups, different blood preparation techniques, inconsistent results, and in one instance, the ingestion of a large air bolus after sampling from a stopcock proximal to the pump inlet.

With the impending start of the PumpKIN trial and anticipated delivery of multiple 4th generation PediaFlow® prototypes, a new experimental system for benchtop hemolysis testing of pediatric MCSDs would be necessary.

2.2 A REUSABLE, COMPLIANT, SMALL VOLUME BLOOD RESERVOIR FOR *IN VITRO* FLOW LOOPS

The work presented below has been published in part within Artificial Organs [150].

Bench-top *in vitro* hemolysis testing is a fundamental tool during the design and regulatory safety evaluation of blood-contacting medical devices. While multiple published experimental protocols exist, descriptions of the test loop reservoir remain ambiguous. A critical fixture within the circuit, there is no readily available blood reservoir that ensures thorough mixing and complete air evacuation: two major factors which can affect results. As part of the FDA Critical Path Initiative, a three-piece reservoir was developed consisting of a 3D-printed base, a plastic clamp set, and a medical-grade blood bag. This simple, reusable, and cost-effective design was used successfully in the hemolysis assessment of FDA benchmark nozzles and prototype rotary blood pumps, and may be useful as an integral component to any *in vitro* blood circulation loop.

2.2.1 Introduction

The characterization of blood damage is essential for the development and safety evaluation of many blood-contacting medical devices including ventricular assist devices, cardiopulmonary bypass (CPB) components, and hemodialysis catheters [140, 141]. In addition to pre-clinical *in vivo* animal studies [142], *in vitro* hemolysis testing is an important tool for assessing the hemocompatibility of mechanical circulatory support devices [36]. Although multiple publications describe variations of the typical experimental loop (**Figure 9-A**), they lack details

regarding the blood reservoir [144, 146, 151]: a vital component towards ensuring accuracy and reproducibility.

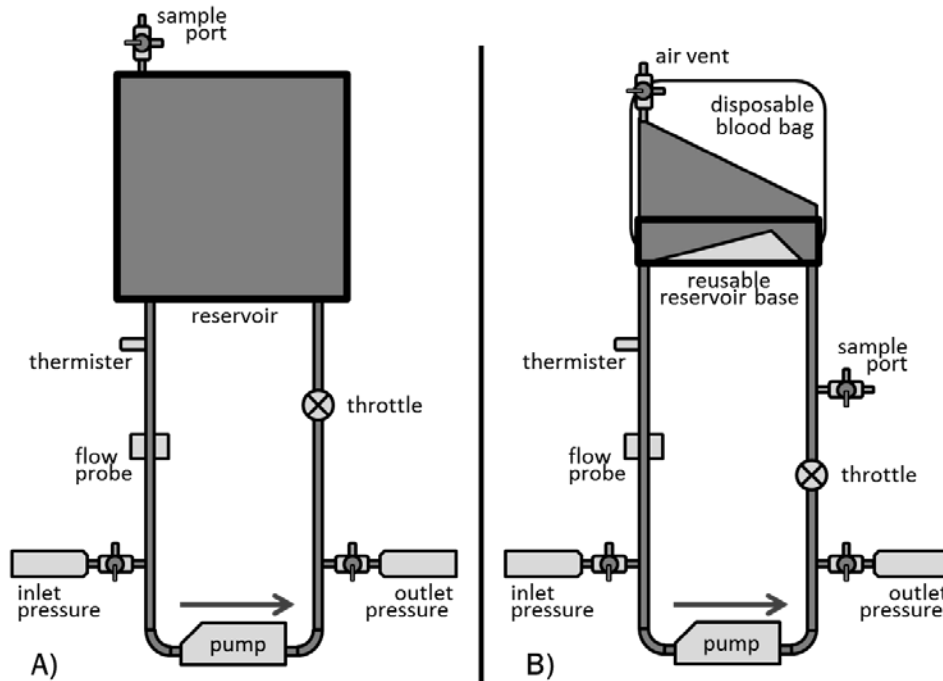


Figure 9. Example mock loops used for *in vitro* hemolysis testing of blood pumps: highlighting the **A)** typical generic reservoir representation and **B)** proposed reservoir design.

Most commercial blood reservoirs cannot 1) accommodate a wide range of blood volumes, 2) provide thorough blood mixing, 3) eliminate the air-blood interface, while 4) remaining reusable or inexpensive. Hard-shell CPB or cardiotomy reservoirs, unable to be de-aired, retain a large air interface. Single-use, soft-shell CPB reservoirs or clinical blood bags often contain extraneous or undersized ports leading to stagnation, pressure loss, and potential collapse (**Figure 10**).

In support of the Food and Drug Administration (FDA) Critical Path Initiative Computation Fluid Dynamics (CFD)/Blood Damage Project, a cost-effective, small volume blood reservoir consisting of a disposable bag clamped to a reusable base (**Figure 9-B**) was

developed to enhance washout while allowing for the complete elimination of air during *in vitro* testing [84].



Figure 10. Commercially available, pediatric (**left**) and adult (**right**) soft-shell reservoirs used in previous benchtop blood biocompatibility experiments highlighting the deficient extraneous and fenestrated ports.

2.2.2 Materials and Methods

1/2”-Port Reusable Base

The rigid base was designed in SolidWorks® (Dassault Systemes®, Velizy, France) with two barb fittings to accept 1/2” ID tubing, a flow separator between the inlet and outlet ports, and a 0.10” external circumferential lip (**Figure 11-A**). The flow separator was shelled to remove excess material while maintaining a minimum thickness of 3/64”. All corners and edges were smoothed on the model before manufacturing. Fabrication was accomplished with a stereolithography additive (SLA) printer (Viper™ SLA® System, 3D Systems® Inc, Valencia, CA, USA) using the Somos® Watershed XC11122 (DSM®, Elgin, IL, USA) photopolymer resin. Following light sanding to remove the printer-generated structural supports, a liquid coat

of the same photopolymer resin was brushed onto the blood-contacting surfaces before a 30-minute UV cure and a final isopropanol rinse.

Disposable Blood Bag

A medical-grade, three-port, 500-mL compliant polyvinyl chloride (PVC) blood bag (Qosina®, Edgewood, NY, USA) was diagonally heat-sealed and trimmed along the bottom to remove the existing orifices. An optional Luer fitting (Qosina®, Edgewood, NY, USA) was fixated into the apex with cyanoacrylate glue before fitting the bag over the base.

Clamp Set

The clamp set consisted of two plastic halves designed to secure the compliant bag against the rigid base (**Figure 11-B**). Milled from rigid PVC stock, the clamps have a 0.10” wide groove to accept the reservoir lip and two throughput holes for assembly using 10-32 machine bolts and wing-nuts.

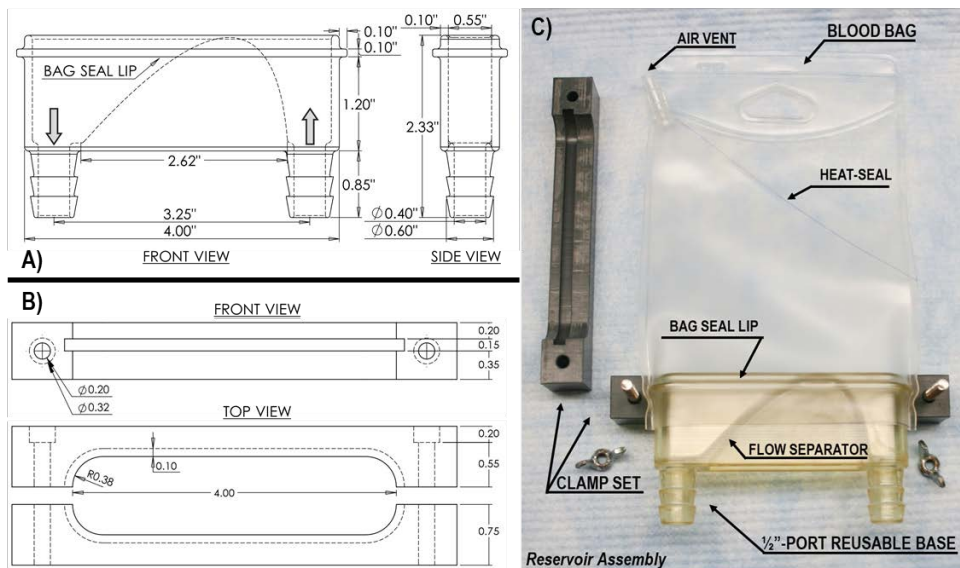


Figure 11. Schematic of the reusable 1/2”-port A) printed base, B) machined clamp set, and C) the manufactured reservoir components with the modified blood bag before assembly.

CFD Analysis

A computational fluid dynamics (CFD) analysis to assess reservoir performance at low flow rates was conducted using SolidWorks® Flow Simulation and compared with a previously employed three-port (two ¼” ID, one ½” ID fenestrated), 1-L commercial CPB venous reservoir bag using a non-Newtonian, power-law blood model (asymptotic viscosity: 3.0 cP) [132, 148]. The reservoirs were assumed to be rigid with inlet flow set to 0.5 L/min to assess their stagnation potential, and an outlet boundary condition of atmospheric pressure at room temperature (20°C).

2.2.3 Results

The single-piece design of the 3D-printed, optically clear, reusable base, devoid of seams or adhesives, reduced the possibility of cracking and contamination. Sufficient wall thicknesses and fillets ensured rigidity and fluid washout of the reservoir base, while lowering printing time and resin cost. With similar material properties as clinically used ABS plastic, the Watershed XC11122 resin meets ISO 10993 standard specifications for cytotoxicity, sensitization, and irritation, along with USP Class VI standards. As the SLA printing process leaves an inherently porous exterior, the integrated liquid resin finish reduced surface roughness to an $R_a < 0.3 \mu\text{m}$ (Contour GT-KI®, Bruker AXS, Madison, WI, USA), avoiding concerns of delamination and wear associated with topical sealants. Compressing the PVC bag between the circumferential lip and clamp created a labyrinth face seal and a leak-proof assembly (**Figure 11-C**). Stain-resistant and easy to clean, the rigid bases have been washed and sanitized with degreasers, enzymatic detergents, 70% ethanol, and 10% bleach without issue before reuse with a new blood bag.

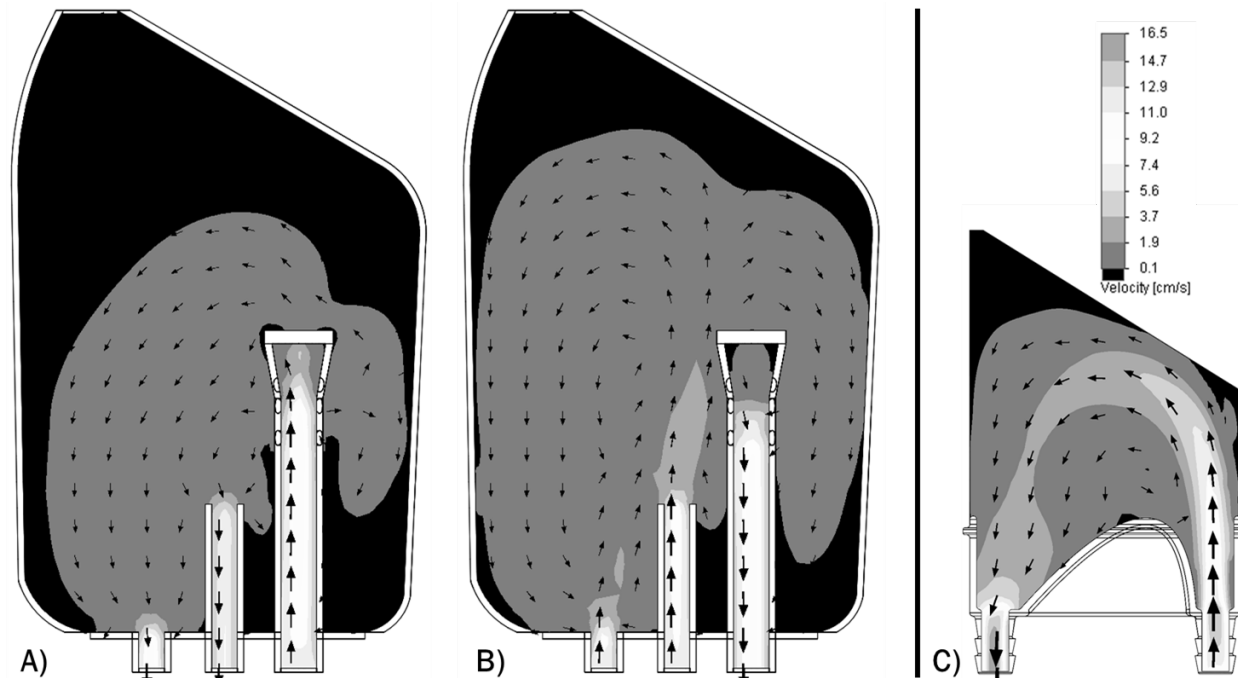


Figure 12. CFD predicted velocity contours at 0.5 L/min for the commercial venous blood bag with the fenestrated port defined as the reservoir **A)** inlet or **B)** outlet, and **C)** the developed 1/2"-port reservoir assembly.

The cross-sectional velocity profiles from CFD-analysis of the commercial venous reservoir bag and proposed reservoir at 0.5 L/min are presented in **Figure 12**. Regions below 0.1 cm/s shown in black designate possible areas of stagnation. After equally distributing blood flow through the two smaller ports to minimize dead space, the three-port commercial bag was examined in two flow configurations. Defining the fenestrated port as the reservoir inlet created large areas of stasis below the inlet sleeve and above the bag outlets (**Figure 12-A**). Reversing the reservoir fluid flow direction decreased those regions by the development of two distinct circulation patterns from the overlapping flows between the shared inlet ports (**Figure 12-B**). In both conditions, peak velocity of 10.8 cm/s was located inside the sleeve of the fenestrated port. In contrast, the designed reservoir assembly had a maximum velocity of 16.5 cm/s and maintained a well-developed, counter-clockwise flow regime (**Figure 12-C**). The flow fields

looked similar at higher flow rates (5 L/min, not shown) with reduced stagnation areas due to jetting, though with more pronounced secondary flow fields in the commercial reservoir.

While vertical operation is suggested to ensure adequate preload and allow hanging using the existing reinforced opening (**Figure 13**), the reservoir has also been utilized horizontally allowing for possible water bath submersion [144]. Priming and air removal was straightforward with the Luer fitting deairing port. The angled heat seal reduces blood volume and, in conjunction with the flow separator within the base, directs flow to minimize stagnant regions within the reservoir. As assembled, the ½”-port reservoirs have a fluid capacity of 250 mL and are customizable by adjusting the bag size, heat-seal angle, and insertion depth of the base before clamping.



Figure 13. The vertically hung, ½”-port blood reservoir assembly after clamping, filling and de-airing.

2.2.4 Summary

This cost-effective assembly provides a useful *in vitro*, bench-top reservoir for hemolysis testing of blood-contacting devices. The reusable, single-piece base enables attachment to low cost, disposable blood bags. The rigid, large bore ports and flow separator minimize resistance, promote mixing, and prevent bag collapse, while the angled compliant bag allows for complete de-airing. The versatility of the reservoir makes it an effective component for any flow loop utilizing blood or other fluids, with an added heat exchanger if temperature control is required during vertical operation. Aside from possible natural yellowing of the reusable base due to ambient UV-light exposure, performance remains unchanged after four years of consistent use in a multi-laboratory study [84]. This novel reservoir has been used successfully during the hemolysis assessment in the FDA benchmark nozzles, rotary blood pump prototypes, and for flow visualization experiments [84].

2.3 RESERVOIR FOR INTRAVENTRICULAR MCS DEVICES

Benchtop evaluation of intraventricular RBPs pose a unique challenge owing to features on the pump surfaces, which impacts hemocompatibility, but may be covered or obstructed after attachment to tubing, compliant blood bags, or clinical hard-shell reservoirs. Maintaining inlet clearance and adequate mixing during testing is crucial at the lower flows associated with pediatric and partial support VADs. An attempt was made to develop a new blood reservoir to address the growing pool of transmyocardial-type VADs, and support *in-vitro* hemolysis assessment.

2.3.1 Methods

Design requirements for an intraventricular-compatible MCS reservoir include: i) a non-collapsible region around the pump inlet, ii) a target total loop blood volume < 1000 mL, iii) gravity assisted priming and drainage, iv) minimal stagnation zones, v) a pump orientation analogous to apical cannulation, vi) straightforward pump insertion and removal without requiring full submersion of the device.

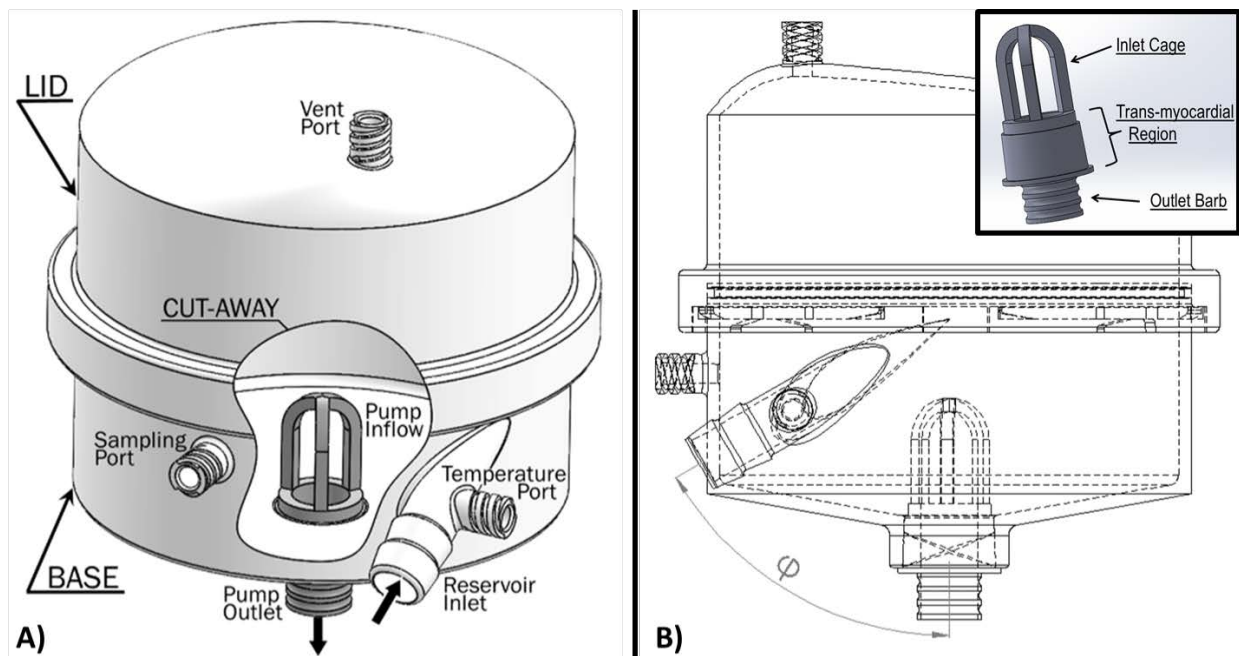


Figure 14. A) The intraventricular-RBP blood reservoir design, B) the reservoir inlet-entrance angles ($\phi = 60^\circ$ & 80°) under consideration, and (inset) the generic RBP-model used during CFD.

A two-piece, bottom-mount, cylindrical reservoir (**Figure 14-A**) was designed in SolidWorks® for SLA-printing using the same optically clear, ABS-like, biocompatible resin and fabrication process from 2.2.2 (Somos® Watershed XC11122). The assembly consists of a lug-type lid which mates flush with the inner lumen of the reservoir base with a radial seal (AS568-043 silicone o-ring, 9396K124, McMaster-Carr®, Elmhurst, IL) outside of the chamber.

Two interchangeable domed lids provide blood volumes of 300 or 500 mL and attach with a keyed, quarter-turn locking mechanism. The 3/8" ID tubing reservoir inlet barb, tangent to the reservoir base, provides washout with either lid size. Pump insertion is provided from the exterior through a 1.0 cm long interference/friction fit opening at the sloped base. Three luer fittings provide ports for fluid sampling, temperature measurement, and venting of the reservoir. A corresponding stand, consisting of three aluminum legs and an acrylic base, elevates the reservoir assembly to accommodate the extra-ventricular portion of the pump and outflow tubing.

Computational Fluid Dynamics (CFD) was performed using SolidWorks® Flow Simulation to determine optimal reservoir entrance inlet angle (**Figure 14-B**) by visual assessment of overall washout, stagnation areas, and ability to remove air emboli removal during operation. Input conditions and assumptions include: i) reservoir inlet flow rate: 0.5-2.0 L/min, ii) pump inflow pressure: 760 mmHg, iii) Newtonian fluid $\mu = 3.5$ cP (asymptotic viscosity of ~30% Ht whole blood at 37°C), and iv) reservoir inlet entrance angle (ϕ): 60° & 80°.

2.3.2 Results and Discussion

Example screenshots from the CFD analysis of the 500 mL capacity reservoir for both inlet entrance angles at two flow rates are shown in **Figure 15**. While blood mixing appears equivalent, air entrapment at the offset vent luer fitting for removal was notably enhanced with the sharper entrance angle (ϕ : 60°) at the flow rates examined. This reservoir design was subsequently printed and evaluated on the bench.

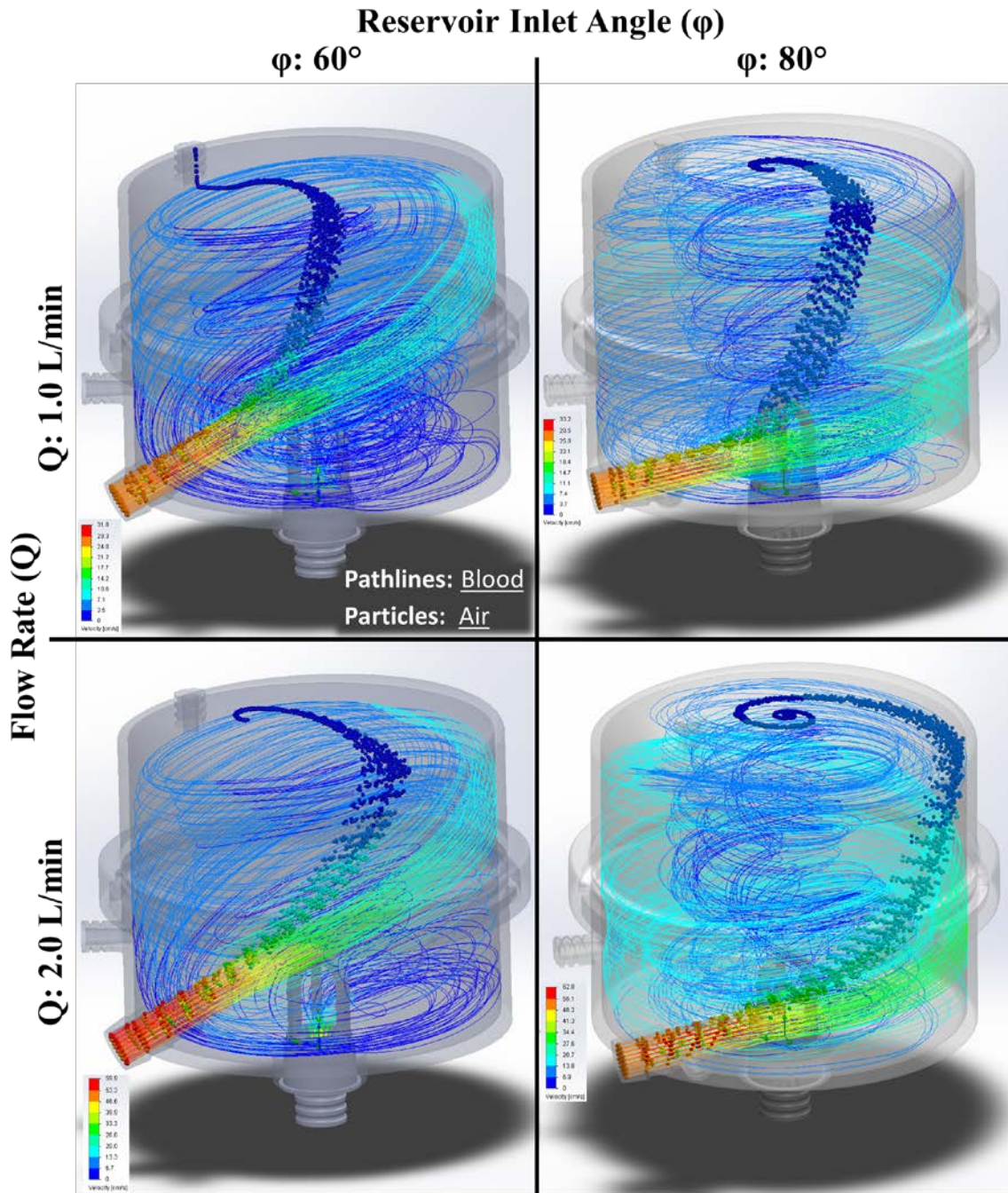


Figure 15. Velocity pathlines of the intraventricular-MCS compatible, 500 mL, *in vitro* blood reservoir superimposed with an emboli particle study to assess air entrapment.

The tapered, friction-fit orifice successfully secured and formed a fluid-tight seal with the use of a silicone tubing “sleeve” around the trans-myocardial portion of a RBP prototype

(VADovations® Inc, Oklahoma City, OK) undergoing evaluation, while the lid mechanism was both leak-proof and easy to operate. Finally, the complementary platform provided adequate stability and clearance for the pump and outflow tubing of the mock loop.

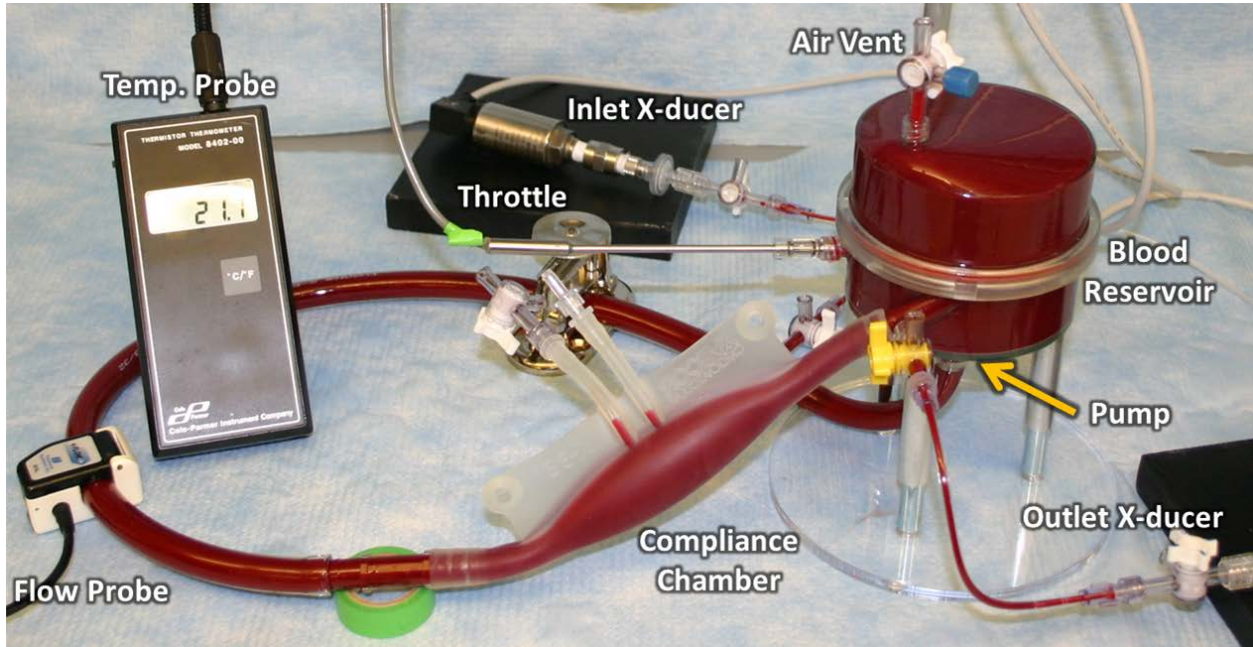


Figure 16. Benchtop hemolysis loop with the SLA-printed blood reservoir and an inline compliance chamber during *in vitro* testing of an intraventricular RBP.

2.3.3 Limitations and Future Work

While the reservoir was used initially in several *in vitro* hemolysis experiments successfully (**Figure 16**), two significant shortcomings with this design soon became evident negating its utility and continued use. Due to the rigidity of the printed housing, a compliance chamber (R-38 ECMO Bladder, Medtronic®, Columbia Heights, MN) was required for sampling during intermediate timepoints without blood volume replacement, and therefore a requisite each test.

Of greater concern, however, was the formation of a large vortex at all hemodynamic conditions due to the cylindrical reservoir design and tangential inlet entrance. Contrary to the

CFD predictions, instead of remaining at the dome, any air present would travel down and be immediately ingested by the pump. In addition to the deleterious effect on blood trauma and micro-emboli generation leading to signal failure of the ultrasonic flow probes, the air can disrupt the hydraulic or magnetic suspension of the rotor causing damage to the pump itself.

Therefore additional development is necessary to design an intraventricular RBP-compatible blood reservoir that addresses these limitations, potentially through off-axis pump placement and an integral compliance component.

2.4 MATERIALS AND METHODS

Crucial to the development of any mechanical circulatory support device is preclinical in-vitro hemolysis testing. Multiple publications have served as de-facto guidelines for examining full-support adult rotary blood pumps, yet continued variability in blood preparation, experimental procedures, and reported results makes comparisons between devices or even laboratories impossible. With the growing interest in pediatric- and partial- support ventricular assist devices (VADs), these existing standards are moreover inappropriate for in-vitro testing of lower flow devices. As part of the PediaFlow® Consortium, a new method is necessary that includes strict adherence to blood preparation, flow loop setup, and sampling procedures to determine the hemolytic potential of the next-generation MCSDs.

2.4.1 Blood Preparation

Fresh, venipuncture ovine blood anticoagulated with sodium citrate was purchased (Lampire Biological Laboratories® Inc, Peperstown, PA) and shipped on ice overnight for use within 3 days. The blood was gravity fed through a 40- μ m leukocyte reducing filter (Pall Biomedical® SQ49S, Fajardo, PR) and hematocrit was adjusted to $30\pm 1\%$ with the addition or removal of autologous plasma. After examination under microscope for gross abnormalities, the blood pool was then measured for the following parameters: total hemoglobin concentration (tHb), plasma-free hemoglobin (plfHb), blood density, whole blood and plasma viscosity (@ shear rate of 200 s^{-1}), total plasma protein (TPP) and fibrinogen (FB) concentrations, and plasma osmolality. In addition, the RBC mechanical fragility index (MFI) of the blood pool each day was assessed using the large volume rocker bead test [84, 93].

2.4.2 Circulating Mock Loop

A schematic of the loop design is shown in **Figure 17**, consisting of a de-airable reservoir (**2.2**), 1/4" and 1/2" ID medical grade Tygon™ tubing (S-50-HL, Saint-Gobain™, Akron, OH), two pressure sensors (PCB Piezotronics® Inc., Depew, NY), a clamp-on tubing flow probe (TS410, Transonic®, Ithaca, NY), a thermistor (Cole-Parmer, Vernon Hills, IL), a manually-adjustable tubing-clamp throttle, high-flow stopcocks (Smith Medical, Minneapolis, MN), pressure monitoring line (Baxter), and polycarbonate barb fittings as appropriate (Qosina®, Edgewood, NY, USA). After assembly each day, the loop was washed with phosphate buffered saline (PBS) for no more than three minutes to ensure the system was sealed and operational. The loop was then drained, primed, and circulated with fresh 1% bovine serum albumin in PBS to passivate all

blood contacting surfaces for five minutes before thoroughly emptying. Blood was gravity filled from the lowest point and walked through the loop components to minimize bubbles. After de-airing the reservoir, the blood was circulated for 30 seconds before stopping to remove any additional visible air before commencing the experiment.

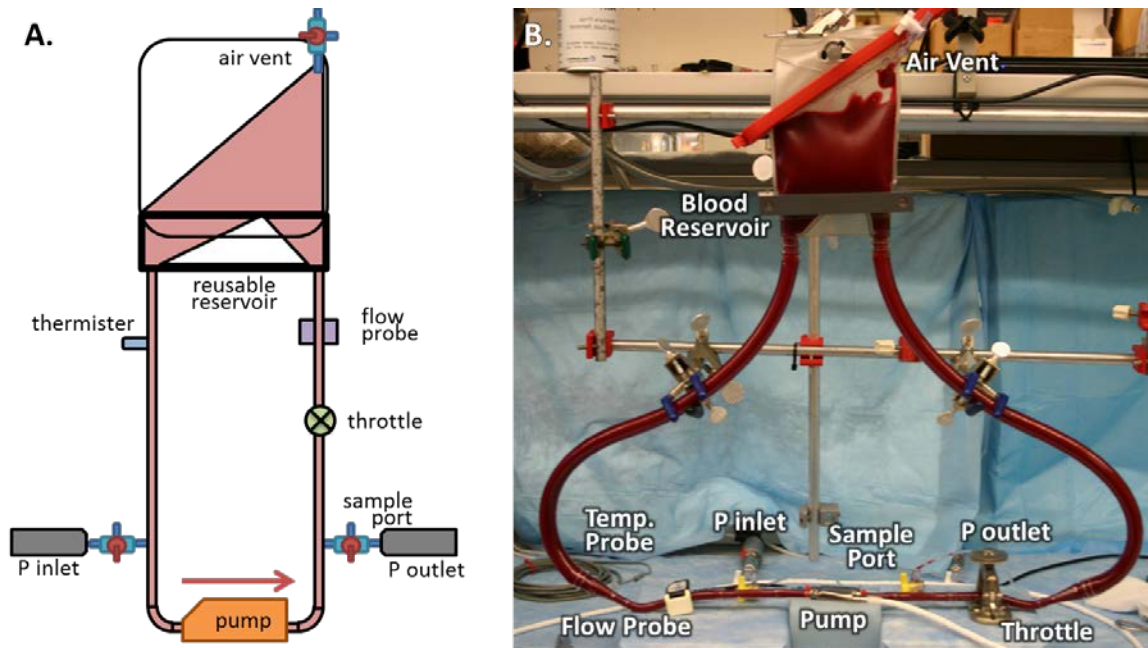


Figure 17. A) Schematic of the pediatric *in vitro* hemolysis loop and B) actual experimental setup.

Loop parameters and MCS D signals were recorded prior to pump start, after achieving desired testing conditions for pressure and flow rate (baseline), and every 30 minutes thereafter. The throttle, and pump speed if necessary, was adjusted as needed to maintain target flow rates, while temperature was monitored but not controlled.

Between tests, the loop was drained and recirculated twice for 10 minutes with fresh PBS, passivating with albumin, and refilling with fresh blood as described above. At the end of each test day, following the multiple PBS rinses until minimal blood was visible, the loop was dismantled. The stopcocks and monitoring line were discarded, while the remaining individual components were cleaned using a 1% solution of lipid-remover (Simple-Green®, Sunshine

Makers Inc, Huntington Beach, CA) and enzymatic detergent (Tergazyme®, Alconox, Inc., White Plains, NY), rinsed (distilled water), dried, and saved for reuse.

2.4.3 Blood Sampling

Samples were taken from the loop one minute after pump start, and every hour subsequently, for the measurement of baseline parameters (e.g.: hematocrit, plasma-free hemoglobin) and trending of plasma-free hemoglobin for hemolysis throughout the experimental duration. All sampling was done from the outflow port, with an initial 0.5 mL discard drawn followed by two plfHb samples (~3 mL/ea) per timepoint. The stopcock port was then immediately cleaned using 4x4 gauze and PBS until no blood remained visible.

2.4.4 Measurements and Analysis

Sample processing (i.e.: repeated centrifugation of the plasma supernatant) and measurement of plasma-free hemoglobin (i.e.: absorbance at 540nm) remained unchanged from previous PediaFlow® iterations [24, 132]. The Normalized Index of Hemolysis (NIH) was calculated for each pediatric hemodynamic test condition as follows [143]:

$$NIH(g/100L) = \frac{\Delta Hb \cdot V \cdot (100 - Ht) / 100}{[Q \cdot T] / 100}$$

where ΔHb is the measured change in plasma free hemoglobin (g/L), V is the total circuit volume (L), Ht is the blood hematocrit (%), Q is the flow rate (L/min), and T is the test duration (min). All calculations and data analyses were done in Excel (Microsoft, Redmond, WA) and SPSS (IBM® Corp, Armonk, NY).

2.5 RESULTS

Seven PF4.x prototypes plus a clinical control (PediMAG®, Thoratec® Corp, Pleasanton, CA) were evaluated at three flow rates (0.5, 1.0, and 1.5 L/min) for 120 minutes against a pressure head of ~100 mmHg at a starting blood loop volume of 300 mL.

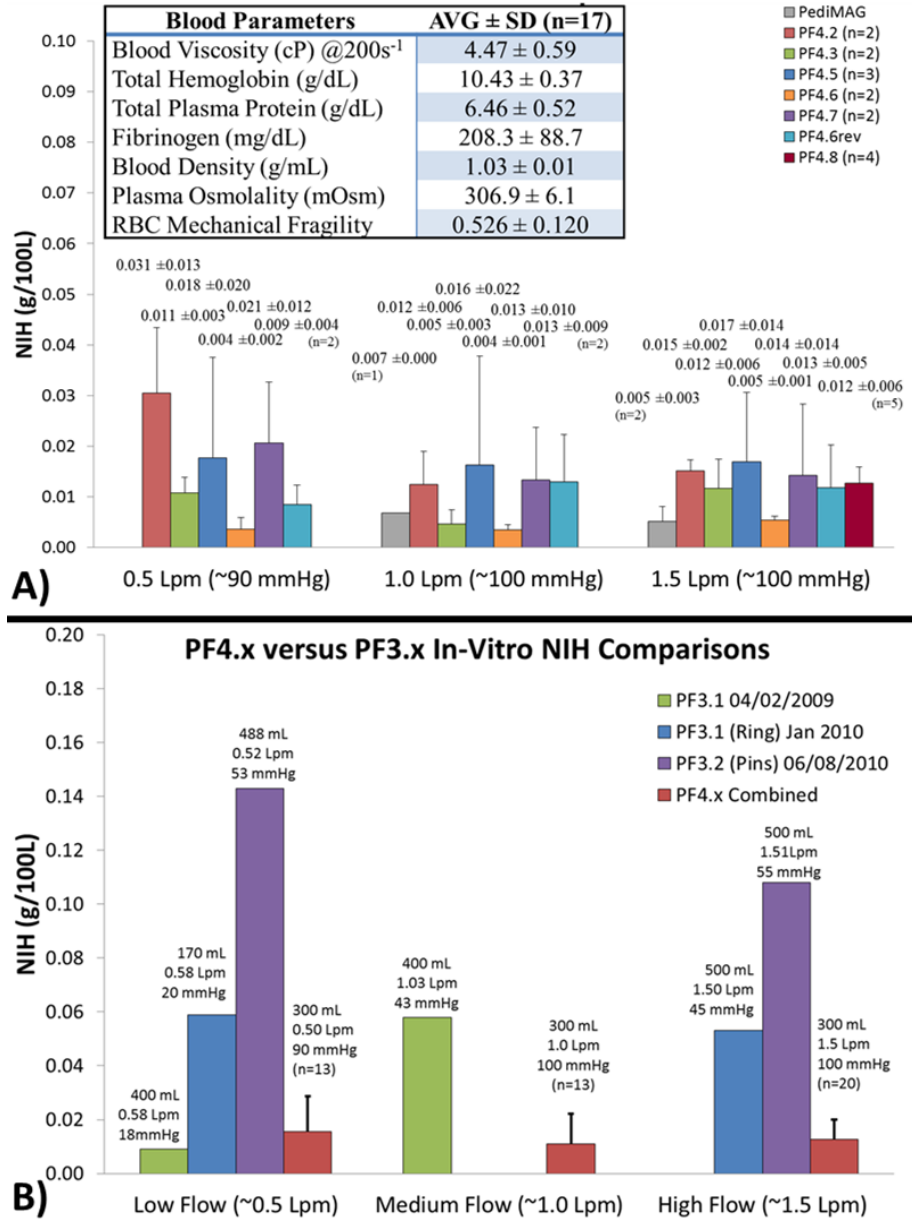


Figure 18. A) NIH results for the eight RBPs tested using the pediatric *in vitro* protocol, a summary of the daily blood pool parameters (**inset**), and **B**) a comparison between the PF3 and PF4 prototypes.

The mean NIH result for each pump at the three flow rates is shown in **Figure 18-A**, along with a table summarizing the daily blood pool parameters between the 17 days of experiments (**Figure 18-inset**). **Figure 18-B** is a comparison of the *in vitro* hemocompatibility performance between the 3rd and 4th generation PediaFlow® iterations.

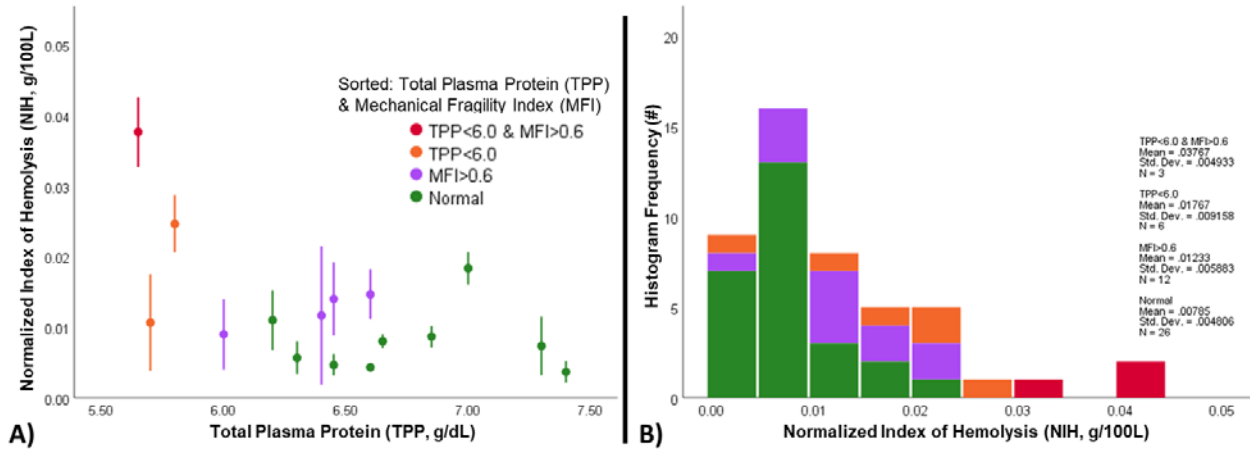


Figure 19. A) NIH results (AVG \pm SD) over corresponding blood TPP concentration grouped by TPP less than 6.0 g/dL and/or RBC MFI greater than 0.6, and B) a histogram plot of the same data.

2.6 DISCUSSION

In vitro testing of hemolysis in pediatric circulatory assist devices is very challenging due to the low flow rates at which these devices are intended to operate. A major source of errors in these tests originates from poor mixing of blood in the flow loop, especially within the blood reservoir. Therefore, the first aim was to redesign the flow system to assure that blood samples collected during the test are representative of the entire blood volume for plfHb concentration. Important features of this flow system are i) the relocation of a significant portion of the loop volume into the large diameter tubing connecting the pump to the reservoir, and ii) the very smooth transition

of the tubing from the horizontally placed pump to vertically positioned blood bag. The second aim was to eliminate potential artifacts and extraneous sources of hemolysis by 1) applying a gravity-driven filling procedure to minimize air bubbles and pre-test blood trauma, 2) strict adherence to sampling procedures (i.e.: drawing from the outlet to minimize the introduction of air, performing a 0.5 mL discard to remove any stagnant blood within the stopcock, taking two samples for plfHb measurement each timepoint, not performing intermediate blood volume replacement, maintaining the luer sampling port, etc.), 3) using fresh blood between different test conditions, and finally 4) complete disassembly before cleaning/sanitizing to prevent contamination by leaching.

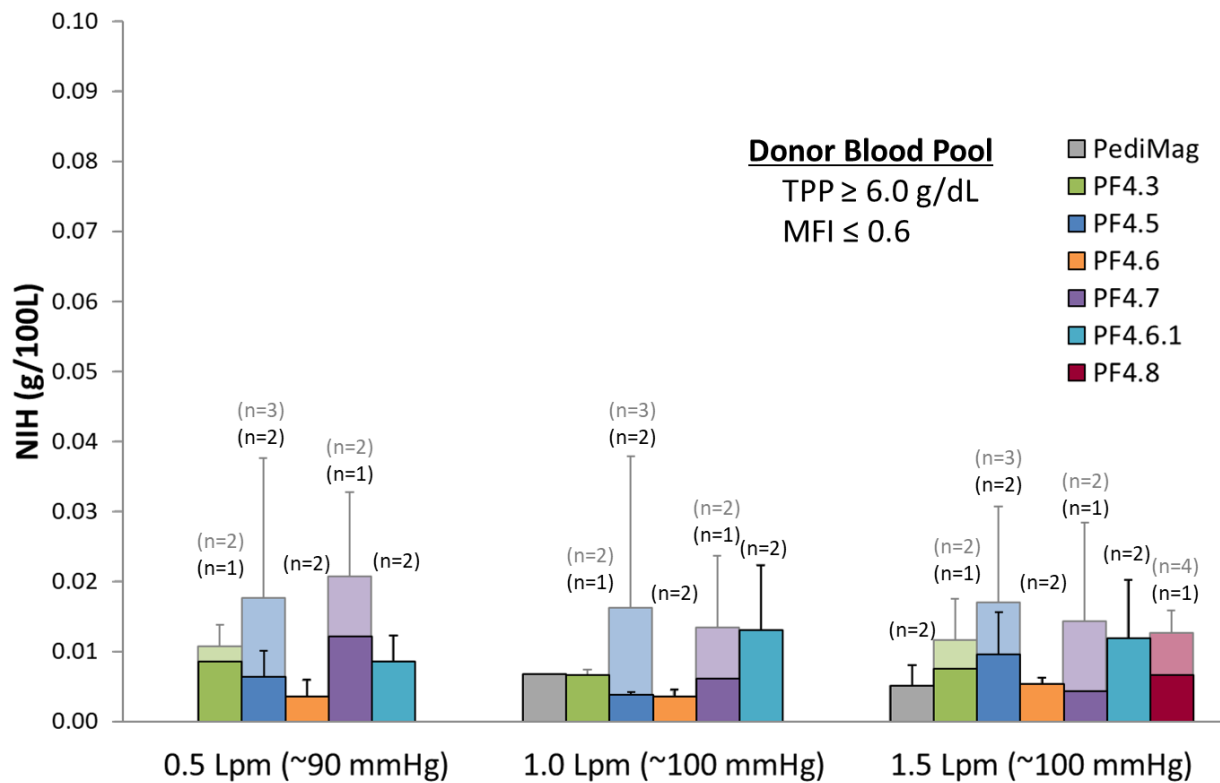


Figure 20. NIH results (AVG ± SD) of the PF4.x prototypes after excluding donor blood pools with a rocker bead test mechanical fragility index above 0.6 or a total plasma protein concentration less than 6.0 g/dL.

As evidenced by the multilaboratory experimental arm of the FDA's Critical Path Initiative and reflected here, both initial blood quality and proper preparation is critical for controlling variability and achieving repeatability. Units that appear to have any amount of clotting should not be used, as blood quality remains questionable regardless of filtration. Accordingly, the purchase of aseptically-drawn, venipuncture blood is less fraught with difficulties associated with abattoir-sourced resources (e.g.: contamination, debris, and clots). As with previous investigators, no correlation was found between RBC MFI and NIH ($r=0.133$, $p=0.37$) in these experiments. However, there was a mild inverse correlation between TPP and NIH ($r=-0.495$, $p<0.01$), which may be reflective of the plasma protein protective effect on RBCs and the original motivation for using autologous plasma for blood hematocrit normalization instead of more popular crystalloid solutions (i.e.: PlasmaLyte, or PBS) [93, 96, 146]. As suggested by **Figure 19**, blood used for *in vitro* hemolysis testing should have an RBT-MFI no more than 0.6 and a TPP concentration no less than 6.0 g/dL to minimize variability and accurately characterize device hemocompatibility. **Figure 20** highlights the decreased variability shown in NIH results of the PF4.x prototypes after exclusion of the blood pools that did not meet the criteria.

2.6.1 Limitations

Acknowledging the deleterious effect of protein dilution, anticoagulating with sodium citrate is the compromise to ensure complete and stable anticoagulation, utilizing a well-known calcium chelator, while still remaining readily reversible. Unfortunately, as a weak acid, excess citrate concentrations can cause acidosis leading to increased RBC MF and poor experimental

outcomes. The pH of the blood pool, which was not measured in this study, should be checked and corrected with bicarbonate before proceeding with *in vitro* hemolysis testing.

2.7 CONCLUSIONS

Benchtop characterization of blood trauma remains an integral and required component for the design, development, and eventual regulatory approval of MCSDs. The increase in smaller and more hemocompatible RBP designs, indicated for pediatric or partial-support use, necessitates the development of new experimental protocols appropriate for these hemodynamic conditions. The experimental setup described here was successfully used in the hemocompatibility assessment of the 4th generation PediaFlow® prototypes, with the potential to support *in vitro* hemolysis testing of, the increasingly popular, intraventricular-type VADs.

3.0 DESIGN AND EVALUATION OF A PEDIATRIC INFLOW CANNULA FOR ROTARY BLOOD PUMPS

This chapter has been published in part within ASAIO Journal [152].

To address the challenge of unloading the left ventricle during pediatric mechanical circulatory support using next-generation rotary blood pumps, a novel inflow cannula was developed. This unique inflow cannula for pediatric, continuous-flow, left ventricular assist devices (VADs) with a parabolic-shaped inlet entrance was evaluated alongside a bevel-tip and fenestrated-tip cannula via an *ex vivo*, isolated-heart experimental setup. Performance was characterized using two clinical scenarios of over-pumping and hypovolemia, created by varying pump speed and filling preload pressure respectively, at ideal and off-axis cannula placement to assess ventricular unloading and positional sensitivity. Quantitative and qualitative assessments were performed on the resultant hemodynamics and intra-ventricular boroscopic visualization to classify conditions of non-suction, partial, gradual or severe entrainment, and ventricular collapse. The parabolic-tip cannula was found to be significantly less sensitive to placement position (p-values < 0.001) than the bevel-tip cannula under all conditions, while not statistically different from the fenestrated cannula. Visual analysis of the parabolic-tip cannula showed complete resistance to entrainment whereas the fenestrated-tip had partial entrainment in 90% and 87% of the over-pumping and hypovolemic studies, respectively. We conclude that future

pediatric VAD designs may benefit from incorporating the parabolic-tip inflow cannula design in order to maximize unloading of the left ventricle in ideal and non-optimal conditions.

3.1 INTRODUCTION

With approximately 36,000 new cases each year in the United States, congenital heart disease is the most frequent birth defect in children [9]. In addition, pediatric cardiomyopathy is a very serious disorder leading to end-stage heart disease with an incidence of 1.13 cases per 100,000 children in the United States [3]. Some of these patients will require a heart transplantation, but with a waiting list mortality rate of 31% at 6-months many of these patients would potentially be saved by long-term mechanical circulatory support (MCS) [153].

Currently the only options for pediatric MCS in the smallest patients ($BSA < 0.7 \text{ m}^2$) are extracorporeal membrane oxygenation (ECMO) and the Berlin Heart® EXCOR® [154]. ECMO is limited to short term support, as the risk of bleeding and thromboembolism complications are proportional to the support length [15]. Indeed, the success rate for ECMO as a bridge to transplant in pediatrics is less than that of adults supported with ventricular assist devices (VADs) [155-157]. While the pulsatile, paracorporeal EXCOR® has greatly improved patient outcomes as the only U.S. Food and Drug Administration-approved pediatric VAD, approximately 80% of patients experienced a significant adverse event during the Investigational Device Exemption (IDE) study [22]. A subsequent multicenter, prospective study reported substantial significant adverse events within the 204 patient cohort, namely for major bleeding (44%), major infection (46%), and neurological dysfunction (29%) [158]. Additionally, both therapies immobilize or limit patient mobility due to pump size, cannulation strategies, and

controller equipment. Therefore, there is increased interest in the development of implantable, continuous-flow VADs for chronic, pediatric MCS [7, 12, 154].

While rotary blood pumps are ubiquitous within the adult population, less attention has been given to the development of similar technology for pediatric support [7]. Important to the safety and efficacy of a rotodynamic VAD is the interface between the inflow cannula and ventricle. As rotary VADs actively empty the heart throughout the cardiac cycle with the potential to generate negative inlet pressures, premature occlusion at the inflow can lead to complications including myocardial entrapment, inadequate support, thrombosis, hemolysis, inner wall bruising, ventricular collapse or arrhythmias [138, 139]. Pediatric MCS candidates, with smaller and variable anatomical configurations, may be more susceptible to misalignment and ventricular suction in comparison with current adult cannula designs. Therefore, design of an appropriate inflow cannula is of utmost importance in order to reduce the risk of post-surgical complications.

3.1.1 Previous Cannulae (PF1-PF3)

Until the 4th generation PF4, previous *in vivo* ovine implantations of the PediaFlow prototypes (PF1-PF3) utilized commercially-available ‘off-the-shelf’ pediatric CPB or ECMO venous drainage cannulae which were then modified for suitability. Ranging from 18-20 Fr with a fenestrated inlet cage, a sewing ring top-hat was added for LV apical cannulation in addition to the connector mechanism for pump attachment as shown in **Figure 21**. These cannulae provided an adequate test bed for assessing pump hydraulic performance and biocompatibility *in vivo* in the juvenile ovine model [132, 134, 148, 159].



Figure 21. Representative inflow cannula used for PF1-PF3 *in vivo* implants with custom sewing rings and pump connectors.

3.1.2 Conformal Cannula

With the introduction of PF4, a PediaFlow® specific cannula was desired to wholly-match the design goals of the pediatric LVAD system. The initial focus for the PF4 inflow cannula was towards a novel conformal cannula developed by the Consortium at Carnegie Mellon University (**Figure 22-A**). This conformal cannula would feature a soft flange at the entrance of the cannula, which would conform to the apex of the ventricle and allow the cannula to act as a more efficient drain to reduce the complications associated with ventricular suction and flow stagnation at the base of the LV. The ability to maximize LV unloading and minimize sensitivity to placement/alignment was previously proven *ex vivo* in a larger form-factor designed for adult VADs [160]. Initial prototypes of the PediaFlow® conformal cannula were carried out using a nitinol wire with a unique clover pattern to allow for the cannula to be malleable and collapsible

into a deployment vehicle (**Figure 22-B,C**). After insertion into the left ventricle, the cannula would unfold into the desired shape after releasing (**Figure 22-D**).

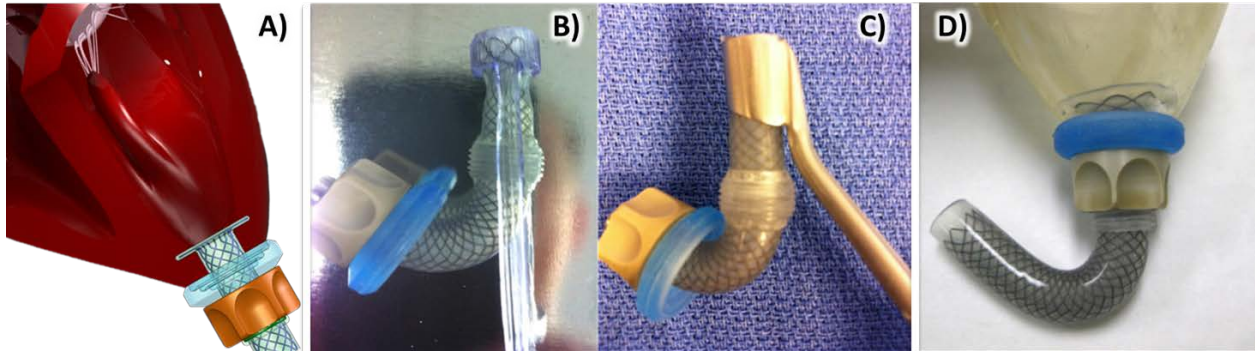


Figure 22. The pediatric conformal inflow cannula assembly (**A**), loaded within the delivery vehicle (**B, C**) for insertion, and deployed into the LV of a silicone ventricle (**D**). Several bench tests of various deployment mechanisms on isolated sheep hearts were performed, with the ease of deployment and placement position within the ventricle encouraging, however the several acute *in vivo* studies that followed were met with some difficulty (**Table 1**). While deployment was relatively easy in an isolated animal heart and pressure flow data were encouraging, deployment *in situ* in a beating heart was not quite as feasible as anticipated. The *in vivo* studies also revealed that it was much more difficult to deploy the cannula completely through the trabeculae that are prevalent in the base of the left ventricle. With only a single deployment attempt possible and lacking haptic feedback when securing locking nut, placement was difficult and inconsistent.

Table 1. Preliminary *in vivo* implants of a *de novo* conformal cannula using the Levitronix® PediMAG® extracorporeal blood pump.

<i>Study Animal</i> (IACUC #)	<i>Wt</i> (kg)	<i>Inflow Cannula</i>	<i>Length (days)</i> <i>Actual/Intended</i>	<i>Avg. Q</i> (L/min)	<i>Findings</i>
CC-S01 (S001-11)	36.6	Conformal 1	Acute (2 hrs)	1.2	1. Successful placement despite difficulty 2. Modifications identified
CC-S02 (S002-11)	34.0	Conformal 1	Acute (1 hr)	0.9	1. Continued difficulty in deployment
CC-S03 (S010-11)	40.0	Conformal 2	3/6	0.9	1. Initial placement successful 2. Drop in Q on POD 3 3. NX: cannula inlet obstructed by trabeculae and tissue overgrowth
CC-S04 (S003-11)	40.0	Conformal 2	6/6	1.25	1. Placement successful 2. NX: myocardial irritation around the inlet flange and ingested thrombus within the pump housing

The results of two 6-day intended chronic implants were also less than ideal, with large pannus growth found completely occluding the inflow flange prematurely ending one study at POD 3 (**Figure 23-A**). The second implant went to term, however examination at necropsy revealed myocardial irritation around the cannula inlet and a large thrombus ingested within the extracorporeal blood pump (**Figure 23-B, C**).

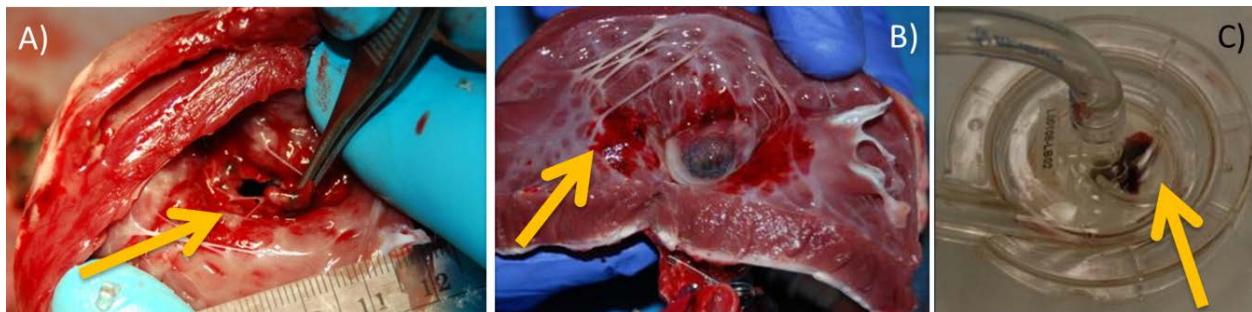


Figure 23. Necropsy results of the two chronic conformal cannula implants. *CC-S03*- a large pannus growth (**A**) in the LV occluding the inlet entrance. *CC-S04*- myocardial irritation (**B**) around the inflow flange and an ingested thrombus (**C**) within the pump housing.

3.1.3 Initial PF4 Implants

After initial setbacks up with a novel conformal cannula under parallel development, the Consortium proceeded to the back-up plan of developing a pediatric version of the standard stove-pipe cannula design used in other VADs. Taking cues from the FDA-approved EXCOR®; a bevel-tip apical inflow cannula was designed and fabricated for the *in vivo* PF4 implants (**Figure 24-A**). The Nitinol wire-reinforced, curved polyurethane body was easily deployable through a cruciate incision to a fixed depth owing to the rigid attachment of the sewing cuff (**Figure 24-B**). After several *in vivo* studies (**Figure 24-C**) revealed the cannula was prone to kinking or inlet occlusion, it was hypothesized that the curvature angle required for animals was greater than that of the design specifications used for humans. A second prototype created using a stiffer 316 Stainless-steel wire, additional strain-relief at the pump connector, and a sheep-specific bend radius, however still suffered from similar complications *in vivo* (**Figure 24-D**) leading to reduced pump flows and limiting operation of PF4 below the design goal of 1.5 L/min.

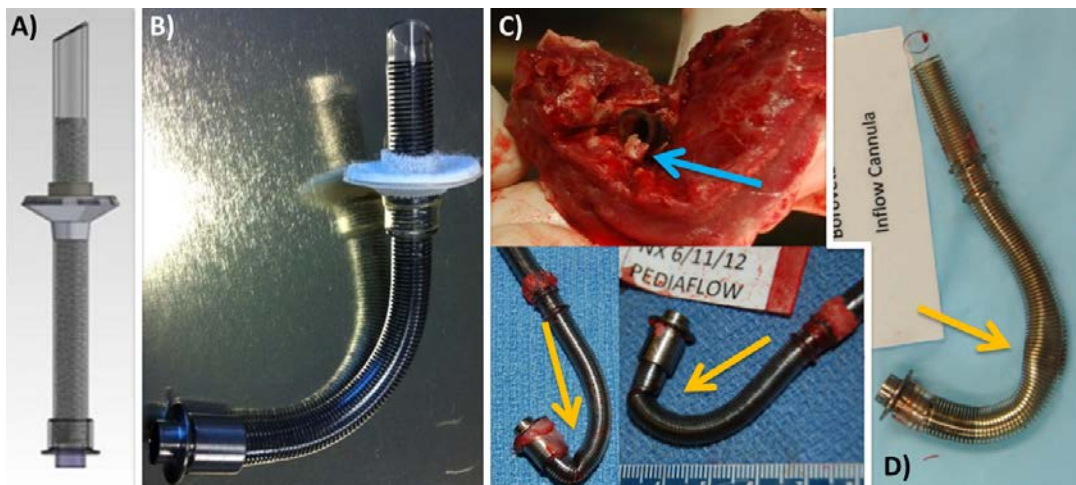


Figure 24. The bevel-type inflow cannula developed and used with the initial PF4 implants. **A)** Rendered apical EXCOR cannula, **B)** the first-generation Nitinol cannula susceptible to inlet occlusion and kinking (**C**), and **D)** the second-generation 316 SS cannula found kinked at explant.

3.2 MATERIALS AND METHODS

3.2.1 Cannula Design

In response to the need for a pediatric-appropriate, left ventricular drainage conduit, a new 5 mm nominal ID inflow cannula was designed and fabricated out of spring-reinforced (stainless steel flat-wire) polyurethane consisting of a parabolic-shaped inflow tip, a removable sewing ring, and tapered strain relief. A finger-operated clamping mechanism on the sewing ring provides a variable cannula insertion depth up to 2.9 cm. The parabolic cannula was compared against a similarly constructed bevel-tip and a commercially-available fenestrated cannula (20 Fr DLP shortened, Medtronic®, Minneapolis, MN, USA), both used for *in vivo* preclinical ovine studies previously (**Figure 25**) [159]. The three cannulae have similar characteristic pressure-flow profiles under static conditions as shown in **Figure 25-D**.

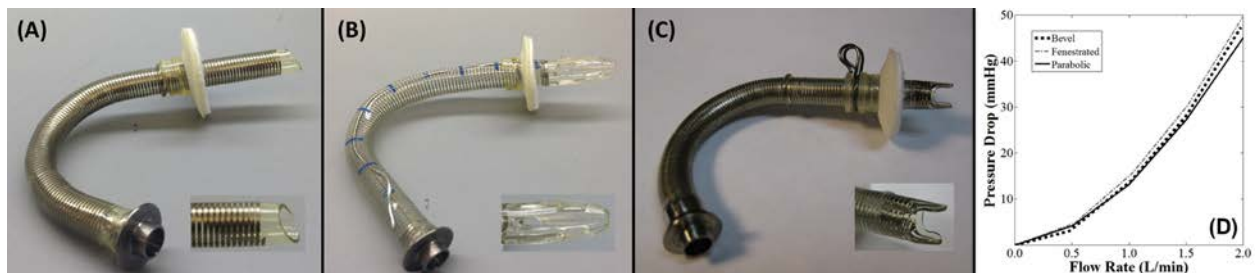


Figure 25. The three pediatric inflow cannulae and respective tip geometries under consideration: the (A) bevel-tip and (B) fenestrated-tip inflow cannulae with fixed-depth sewing rings, and the (C) novel parabolic-tip inflow cannula with the adjustable depth sewing ring. (D) Experimentally derived static characteristic pressure-flow (H-Q) curves of the three cannulae using an acellular 40% glycerol/saline solution ($\mu = 4.6$ cP).

3.2.2 Experimental Setup

Juvenile ovine or caprine hearts were obtained from a slaughter-house, cleaned, weighed, and trimmed of their pericardium for use in an *ex vivo* pediatric isolated heart model. A removable sewing ring was fixated to the apex of the left ventricle (LV) using 2-0 pledgeted sutures and a borescope was introduced from the left atrium (LA), secured with 2-0 purse string, through the mitral valve for visualization purposes. The aorta was closed with a 2-0 purse string around ¼” OD tubing with a stopcock to release trapped air within the ventricle. The test cannula was then inserted 2.4 cm past the sewing ring, through a cruciate incision in the myocardium.

The experimental isolated-heart flow loop was setup as seen in **Figure 26** [161]. The circulating fluid of 40% glycerol in saline (4.9 ± 0.1 cP), a blood analogue, was seeded with neutrally buoyant reflective particles (Amberlite IRA-96, Sigma Aldrich, St. Louis, MO). A constant preload into the ventricle was maintained in the vertically elevated fluid reservoir using an overflow chamber. A centrifugal pump (PediMAG®, Thoratec® Corp, Pleasanton, CA) was used to generate flow through the heart-cannula assembly, and a solenoid pinch-valve (ASCO® Valve Inc., Florham Park, NJ, USA) proximal to the LA inlet was utilized to induce contraction and free wall movement in the ventricle. The left atrial (LAP), left ventricular (LVP), and cannula outlet pressure (COP) were measured using three pressure transducers (648, PCB Piezotronics® Inc., Depew, NY), and a clamp-on flow probe (TS410, Transonic®, Ithaca, NY) was attached at the pump outlet to measure flow rate (Q) through the cannula.

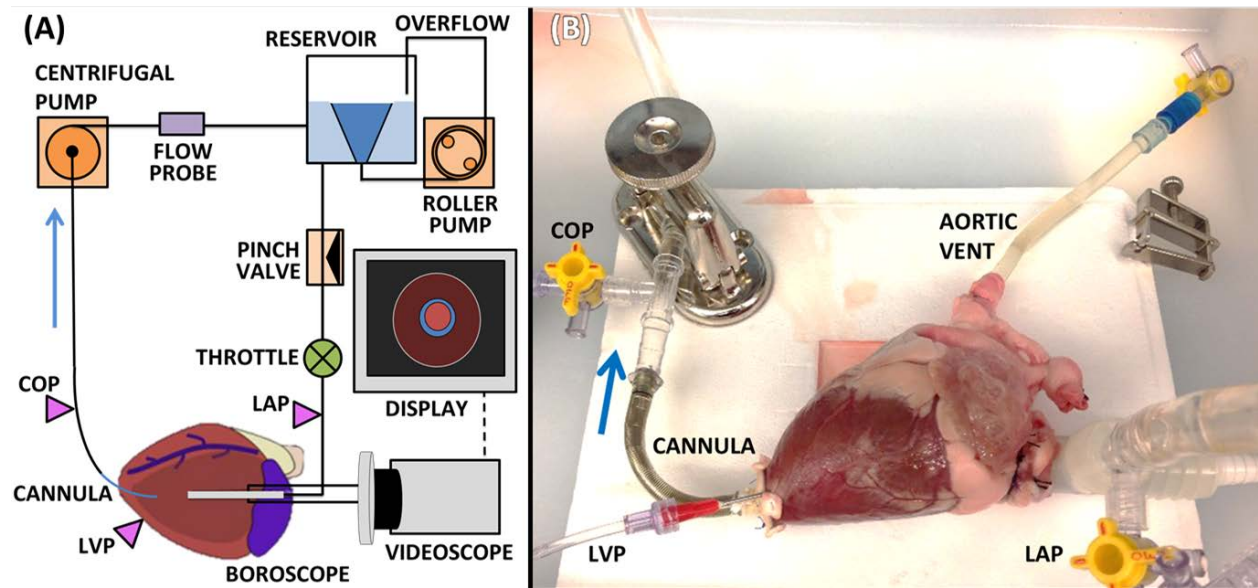


Figure 26. (A) Schematic of the modified *ex vivo* isolated-flow loop used to assess cannula performance (aortic vent not shown) and (B) an image of the *ex vivo* flow loop in the normally aligned state.

The three cannulae were evaluated using two protocol scenarios to mimic the clinical complications of over-pumping and hypovolemia to assess LV unloading ability. Over-pumping was achieved by continually increasing pump speed (PS), starting at an approximate flow rate of 0.3 L/min. The hypovolemia protocol, representing inadequate blood volume, was performed by gradually decreasing LAP from 20 mmHg to 5 mmHg using a proximal tubing clamp while maintaining a constant PS. The over-pumping protocol was carried out with 7 hearts ($n_{op} = 21$) and the hypovolemic protocol was completed with 5 hearts ($n_{hv} = 15$). Both protocols were executed in normal and misaligned positions to assess positional sensitivity, with misalignment created by fixing the cannula posteriorly approximately 45 degrees [160].

3.2.3 Data Analysis

Acquired data was processed using MATLAB® (MathWorks, Natick, MA) for this study. The percent change in flow rate caused by misalignment, termed as the positional sensitivity index (I_{ps}) was calculated using the following equation:

$$I_{ps} = \frac{Q - Q'}{Q} * 100\%$$

for the maximum flows attained in the over-pumping protocol and flows at certain LAPs in the hypovolemic protocol for each cannula, where Q is the flow rate of a normally aligned cannula and Q' is the flow rate when misaligned [160]. Statistical analysis was performed by one-way and repeated measures ANOVA with Bonferroni *post hoc* tests using SPSS® v23.0 (IBM® Corp, Armonk, NY), with significance assumed at $p < 0.05$.

The boroscopic videos were manually analyzed for ventricular collapse and/or entrainment of the cannula orifice during the study [160]. Equal reduction of the LV wall around the cannula was categorized as “Concentric Collapse”, while entrainment was defined in three categories: partial, gradual, and severe. “Partial Entrainment” is defined as the blocking of only a portion of the cannula orifice, while the remaining is unrestricted to flow. In the event of full entrainment of the cannula orifice, a time-analysis was performed to determine the severity. Cases of full entrainment where the average flow rate fell 10% within a one second interval during the suction event were classified as “Severe Entrainment”, while the rest were considered “Gradual Entrainment”. The average flow rate in these cases was calculated for each time point with all data points half a second before and after in order to capture a full loading cycle. If no collapse or entrainment was observed, the experiment was categorized as “No Visible Collapse/Entrainment”.

3.3 RESULTS

A total of seven hearts (average mass of 140.6 ± 15.2 g) were processed, prepared and used for the *ex vivo* analysis. Raw data from the over-pumping and hypovolemic protocols were processed in MATLAB® in order to calculate the positional sensitivities of the cannulae. **Figure 27** is a representative isolated heart experiment showing the hemodynamic performance of each cannula in both protocols in the normal and misaligned state.

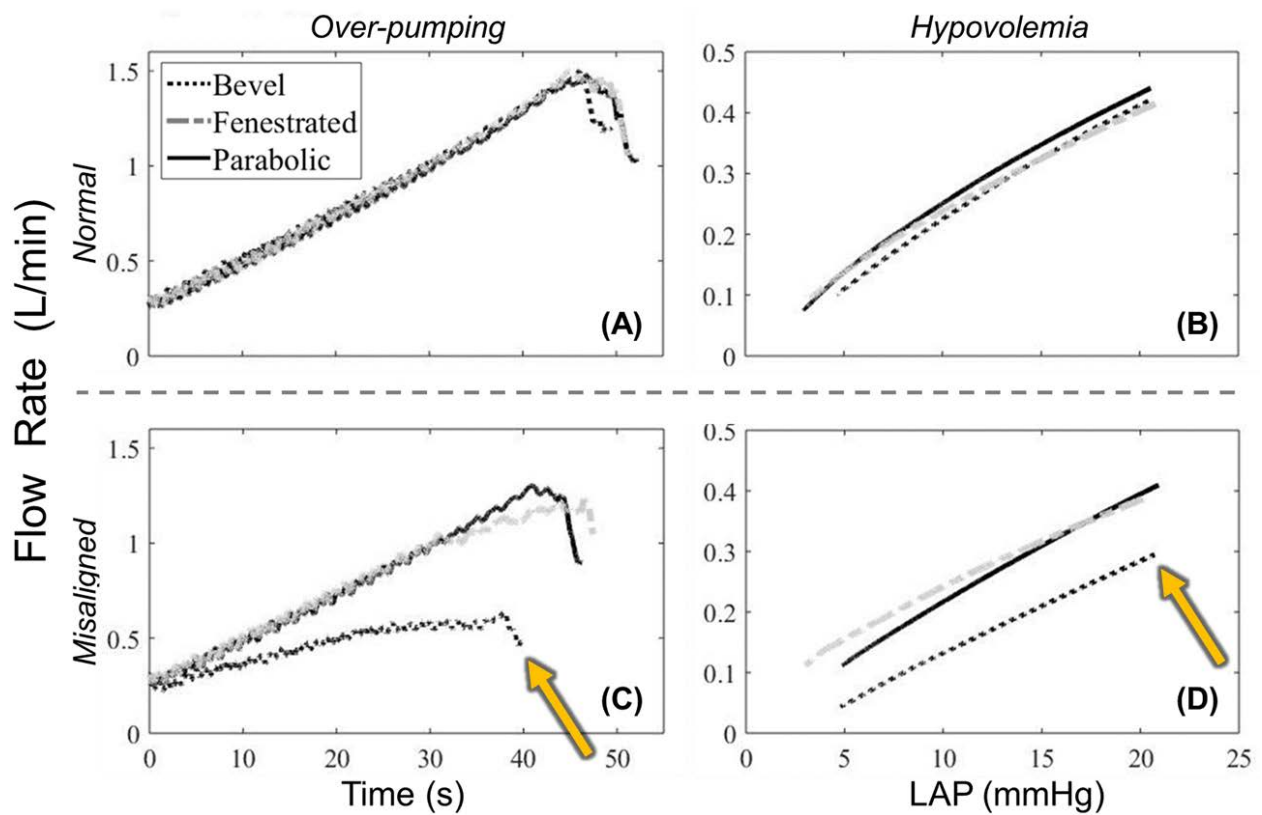


Figure 27. Sample data set from one experiment showing cannula performance as measured by achievable flow rate under both protocols. All three cannulae perform similarly with (A) increasing pump speed or (B) decreasing pre-load, however the bevel-tip had a marked drop in flow rate when misaligned (C, D).

3.3.1 Positional Sensitivity

The maximum flow rates and calculated I_{ps} values for the over-pumping protocol are summarized in **Table 2**. While there was no significant difference in flow rates when normally aligned, there was a significant drop in flow rate for the bevel cannula in comparison to the other two cannulae (p-value < 0.001) when misaligned. Correspondingly, there was no significant difference in I_{ps} between the fenestrated and parabolic cannula, and both were significantly less sensitive to placement position than the bevel cannula (p-value < 0.001).

Table 2. Positional sensitivity results for the three cannulae using the over-pumping protocol ($n_{op} = 21$)

	Cannula Type			<i>P</i>
	Bevel	Fenestrated	Parabolic	
Maximum flow rate (L/min)				
Normal alignment	1.27 ± 0.03	1.25 ± 0.04	1.28 ± 0.04	0.822
Misaligned	0.63 ± 0.07	1.18 ± 0.03	1.19 ± 0.02	<0.001*
I_{ps} (%)	49.9 ± 2.2	4.7 ± 2.2	6.7 ± 1.8	<0.001†

Data presented as mean ± standard error of the mean.

*Bevel v Fenestrated p<0.001, Bevel v Parabolic p<0.001, Fenestrated v Parabolic p=1.000.

†Bevel v Fenestrated p<0.001, Bevel v Parabolic p<0.001, Fenestrated v Parabolic p=1.000.

Likewise, the resultant hypovolemia I_{ps} values across preload pressures for each cannula are shown in **Figure 28**. The bevel-tip cannula was found to be significantly different than the parabolic-tip cannula at each preload pressure (p-value < 0.001), while no significant difference in positional sensitivity was found between the parabolic-tip cannula and the fenestrated-tip cannula (p = 1.000).

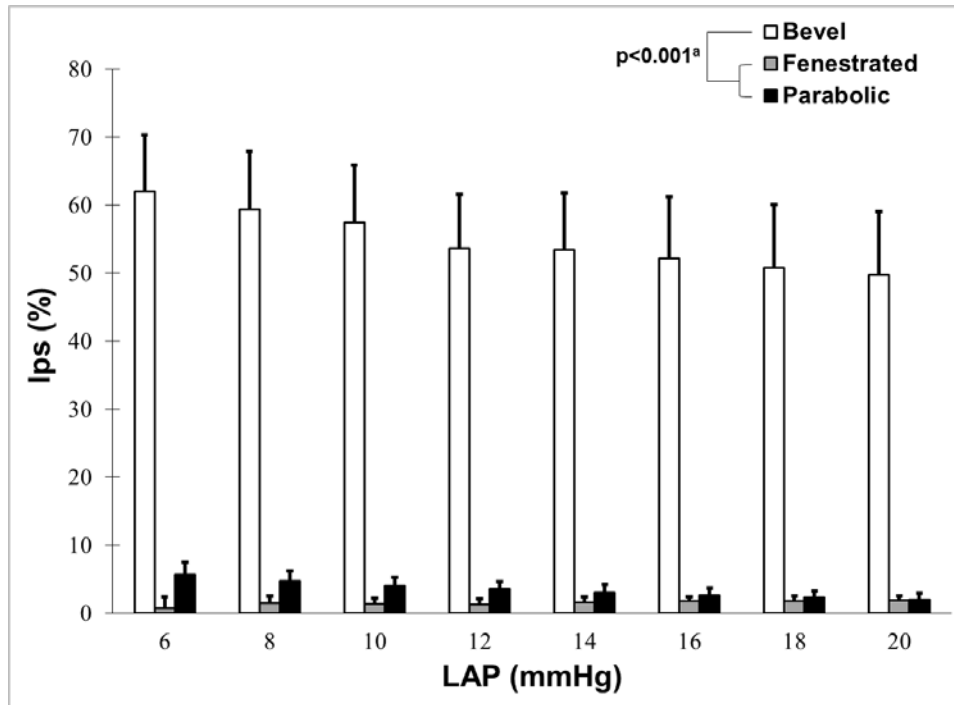


Figure 28. Positional sensitivity results of the three cannulae in the hypovolemic protocol ($n_{hv} = 15$). Data presented as mean \pm standard error of the mean. The bevel cannula was significantly more sensitive to positioning within the ventricle compared to the fenestrated and parabolic cannulae. ^aBevel v Fenestrated $p < 0.001$, Bevel v Parabolic $p < 0.001$, Fenestrated v Parabolic $p = 1.000$.

3.3.2 Borescope Results

Manual inspection through the ventricular borescope tool was performed for each test in the over-pumping and hypovolemic protocols. Multiple cases led to both a concentric collapse and a partial entrainment assessment. In those cases, that experiment was tallied under both conditions, therefore leading to values over 100% for a particular cannula. The visual example in **Figure 29** shows the difference between each cannula in the normally aligned state and the misaligned state. Entrainment and ventricular collapse observations were made from these images, which are summarized in **Figure 30**. Also in this study, there were six separate instances where at least one

of the neutrally buoyant visualization particles were noted to be resting on the caged area of the fenestrated-tip cannula.

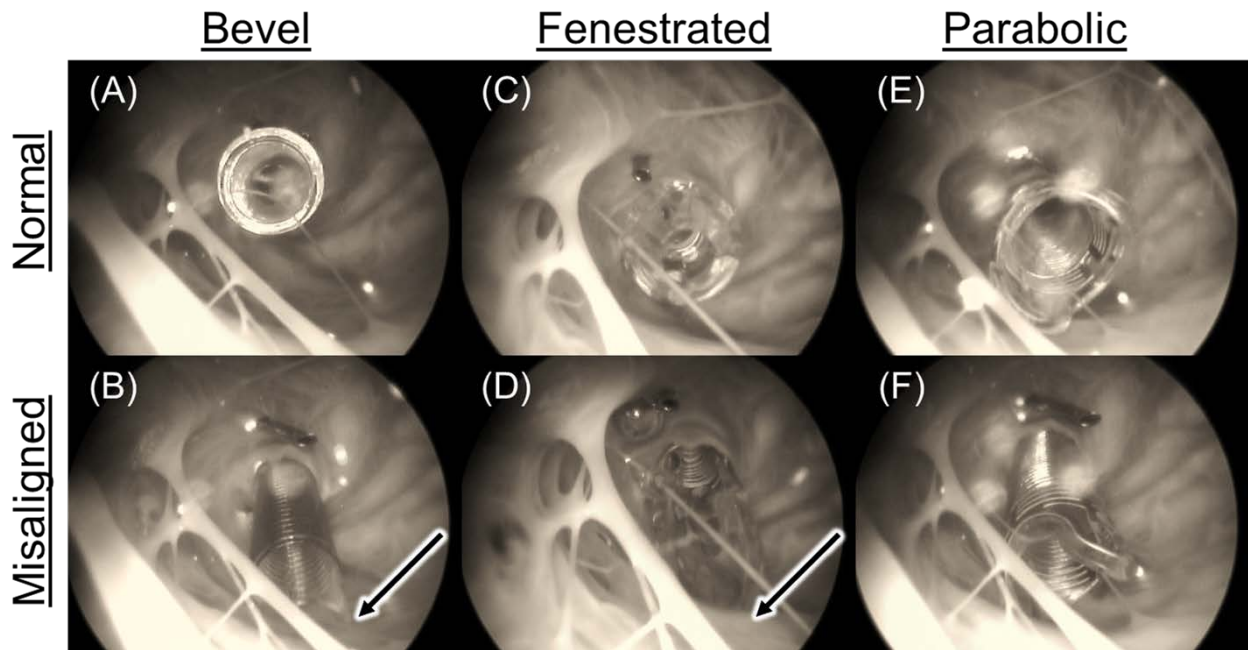


Figure 29. Color enhanced representative intraventricular images of the normally aligned cannulae (top) and the misaligned cannulae (bottom) from the boroscope. The bevel, fenestrated, and parabolic cannulae are shown to have no obstructions with normal placement (**A,C,E**). However, while all cannulae are facing the LV free-wall when misaligned, the bevel and fenestrated tips are prone to premature myocardial entrapment leading to (**B**) severe or (**D**) partial occlusion of cannula inlet indicated by the arrows. In contrast, the parabolic cannula in the misaligned state (**F**) remains unobstructed.

3.4 DISCUSSION

The results from the over-pumping protocol, performed similarly to clinical echocardiography ramp studies, and hypovolemia protocol indicated that the newly developed parabolic cannula performed significantly better than the bevel cannula. The positional sensitivity results for both protocols suggest that the bevel cannula has a narrow optimal operating window to unload the

ventricle, which may explain the complications experienced in prior preclinical *in vivo* juvenile ovine LVAD implantations [162, 163]. Therefore, those complications may be alleviated through the use of the parabolic or fenestrated cannulae, which have a lower sensitivity to misalignment within the ventricle.

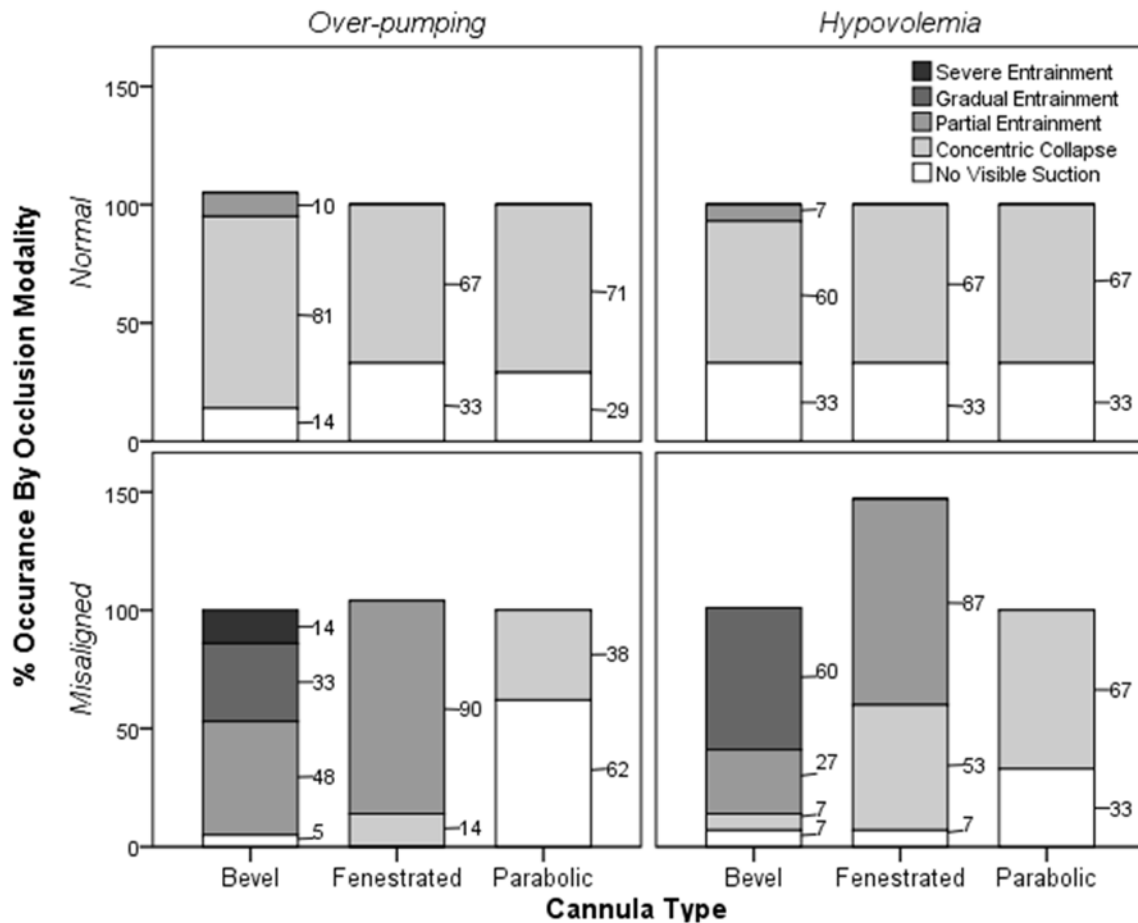


Figure 30. Occlusion modality results of the left ventricle as determined by intraventricular imaging and flow rate analysis. In summary, the bevel cannula was severely dependent on intraventricular alignment, the fenestrated cannula was resistant to full entrainment, while the parabolic cannula showed resistance to all forms of premature ventricular suction.

Visual analysis of the boroscopic images suggests that there may be subtle differences between the parabolic and fenestrated tip geometry, specifically during misalignment. While a clear and open path was observed for the parabolic cannula prior to any subsequent event, the

fenestrated cannula had one or more cage inlets blocked by the ventricular wall in 90% of over-pumping and 87% of hypovolemic studies. This partial entrainment of the fenestrated cannula may lead to damage of the myocardium or hemolysis. Additionally, there were six separate observations of particles resting on the caged portion of the fenestrated cannula which indicates stagnation risk and may be associated with thromboembolic consequences.

The ability to visualize and quantify ventricular ‘suck-down’ makes this a reasonably simple and accurate method for assessing cannula performance, but there are several limitations to this *ex vivo* isolated heart setup described in detail by Bachman *et al* [160]. Most notably, it is impossible to replicate directly on the benchtop the thrombogenic, thromboembolic, or pannus potential that *in vivo* assessment could provide. The addition of the new solenoid pinch valve cycling at 1.0 Hz (60 beats/min) to control LV preload induced measurable pulsatility (unsteady flow) and led to visible contraction of LV chamber. This dynamic, ‘pulsing-heart’ configuration allowed for the observation of partial or incomplete suction events. While still not a true beating-heart preparation, this is an improvement over the previous static setup [160, 161].

Ultimately, this experiment showed that the parabolic cannula design is significantly superior to the bevel cannula in completely unloading the LV while avoiding the partial entrainment and stagnation zones associated with the fenestrated design. While literature is vague on the criticality of inflow cannula alignment, the efforts towards VAD suction detection algorithms and automatic speed controllers allude to the frequency and severity of complications associated with non-optimal unloading of the left ventricle [164, 165]. The use of entrapment resistant and position insensitive pump inlet cannulae may reduce intermittent suction episodes that necessitate speed reductions. This, in part, has served as a basis towards the development of ‘beak’, ‘corona’, and ‘trumpet’ designs with varied success due to thrombosis or

thromboembolic complications related to insertion depth rather than inlet tip geometry [166-168]. It is these depth concerns that may also explain the tradeoffs associated with the conformal cannula, whereby enabling the complete drainage from the base of the LV apex also allows the ingestion of any debris or thrombus into the pump and possibly further downstream in the form of thromboembolic events [167, 168].

With a reinforced parabolic inlet entrance, this cannula combines the efficiency and flow characteristics of standard ‘stovepipe’ designs, while providing secondary flow paths similar to the fenestrated venous drainage cannula. The novel parabolic-tip cannula is defined by a combination of features including a removable sewing ring for unobstructed visualization, a radiopaque tip to ease myocardial insertion, and a nitinol spring clamp for tool-less depth adjustment. These additions are highly significant for pediatric VADs, as variability in myocardium thickness and chamber geometry between patients would hinder optimal placement with only a single, fixed cannula available. The parabolic cannula allows for this versatility from patient to patient while maintaining optimal flow out of the ventricle.

3.5 CONCLUSIONS

These studies reinforce the importance of cannula placement for avoiding premature ventricular suction during assisted circulation, and the influence of inflow tip geometry on mitigating the effects of inlet obstructions. The novel parabolic-tip, adjustable depth, pediatric inflow cannula was insensitive to positional placement and enabled maximum unloading of the left ventricle. This information can help guide future pediatric and adult VAD inflow cannula designs to reduce complications during chronic, continuous-flow mechanical circulatory support.

4.0 A COMPREHENSIVE DIAGNOSTIC SUPPORT SYSTEM (DSS) FOR *IN VIVO* TESTING OF THE PEDIAFLOW®

Despite continuing advances in MCS technology, post-operative complications after VAD implantation persists and can lead to significant morbidity and mortality if unaddressed. Basic device alarms with multiple source triggers and conflicting treatment options, require trained clinicians to qualitatively process pump, hematological, and physiological parameters to determine the most likely diagnosis and select an appropriate course of action. Traditionally beginning development in earnest only after pump finalization, the lack of a clinical interface poses an even greater challenge during *in vivo* studies due to the differences in species, staff expertise, and available resources. The work presented here describes the effort to develop a modular, reusable, and straightforward user interface for managing *in vivo* implants and supporting overall pump development.

4.1 INTRODUCTION

While 2nd and 3rd generation RBPs are significantly less complex mechanically than 1st generation pulsatile VADs, there is also an inherent decrease in available pump parameters with diagnostic utility. With flow sensors, pressure transducers, and/or fill/empty signals, variations in flow rate with a volume-displacement pump are easily attributed to either preload (inlet) or

afterload (outlet) variations solely through the device itself. In contrast, rotodynamic pumps operate at a fixed speed, whereby flow is inversely proportional to the pressure head/drop, or total resistance across the pump, and therefore indistinguishable without the use of derived, low-specificity, time-dependent indices or algorithms (i.e.: pulsatility).

A critical discrepancy during the acute post-operative recovery phase when the patient is most unstable, this is mediated clinically by the availability of supplementary diagnostics (e.g.: Swan-Ganz catheter, echocardiography, etc) providing hemodynamic and physiological parameters for feedback. However, these tools are largely unavailable in survival animal studies due to poor patency rates, infection risks, IACUC guidelines or protocol restrictions, or overall feasibility and animal husbandry considerations, necessitating a greater reliance on the pump parameters available for post-operative management.

Additionally, preclinical testing of prototype blood pumps is a unique challenge due to the incomplete and ongoing nature of device design, with implants often utilizing unfinished controller, software, and alarm designs. Any adverse pump related event if not observed or recognized during the episode may lead to catastrophic failure of the pump or study. Therefore, it would be advantageous to have a software platform during preclinical studies that provides real-time monitoring and alarm notifications to assist in study management and device troubleshooting, instead of serving only as a data recorder for subsequent processing and analysis offline.

4.1.1 PediaFlow® Operation and Monitoring

Since PF2, the controllers accompanying the PediaFlow® pump were first-in-man Levacor® controllers, provided by the Consortium's corporate partner (MedQuest/WorldHeart), modified

to support the specific prototype. These controllers were to provide a temporary operating platform for the PediaFlow® technology while the clinical controller was under development. As the only goal was to design and develop the pump, the computer monitoring software provided minimal functionality aside from levitating the rotor and adjusting motor speed.

Instead, the WinDAQ® (DATAQ®, Akron, OH) software system shown in **Figure 31** was used in tandem on the same netbook (**Figure 31-inset**) to monitor, trend, and record pump and hemodynamic signals. While used successfully for data acquisition (DAQ) since the first PediaFlow® *in vivo* study through the PF3 implants, it is difficult to read and is limited to only data logging and basic out-of-bounds alarm monitoring. It lacks the ability to program or create derived parameters (ie: flow estimation, pulsatility index), moving averages are only available through obscuring popup windows, and the previous history is only accessible through a separate program. These shortcomings make the program far from ideal for pump monitoring and medical management during implants.

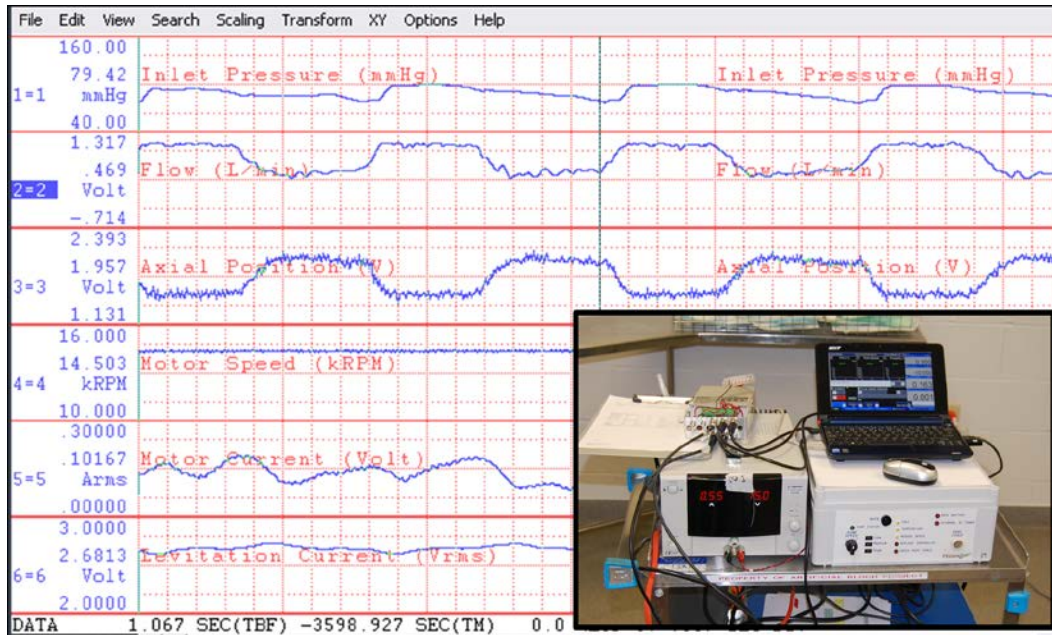


Figure 31. A screenshot of the WinDAQ® window and *in vivo* computer cart (**inset**) running the software.

Commercial DAQ Software

While more advanced, feature-rich, off-the-shelf DAQ platforms exist, like LabChart (ADInstruments®, Colorado Springs, CO) or SignalExpress™ (National Instruments®, Austin, TX), these programs are computer intensive, unable to perform complex signal transformations or calculations, and are less-customizable for the ‘mission-critical’ environment within the ICU. system architecture and application development.

4.2 SYSTEM ARCHITECTURE AND DEVELOPMENT

The DSS was developed around the National Instruments® (NI) DAQ ecosystem which provides straightforward interoperability between NI® hardware and their LabVIEW® programming environment.

Program Design Requirements

The DSS should be informative yet uncluttered with all relevant data presented in an organized manner without overwhelming the user. Any interface should be responsive, exploit operator intuition, and be decoupled from logging functionality to prevent data loss [169]. The use of a modular architecture allows for enhanced functionality through straightforward upgrades. Proper interrogation, analysis, and troubleshooting of any complications would require the ability to easily review event and signal histories. Alarms should be distinguishable by priority to prevent ‘alarm fatigue’ [169]. Message text should be clear and concise in stating the cause and potential resolutions of an alarm to minimize interpretation. Finally, a remote notification routine would

enable doctors and engineers the ability to accurately diagnose and troubleshoot both animal and pump issues without being physically present.

4.2.1 Materials and Methods

The multichannel, high-speed, bus-powered NI® USB-6218BNC DAQ was selected to collect the relevant signals from the pump controller and clinical monitor. This hardware also supports multiple digital input and output lines that were used to implement an alarm buzzer and can be used for potential physical controls in the future.

The DSS was programmed in LabVIEW® 2009 - LabVIEW® 2014 in accordance with the following design guidelines and requirements in mind. The graphical user interface (GUI) should be informative yet uncluttered with all relevant data presented in an organized manner without overwhelming the user. Any interface should be responsive, exploit operator intuition, and be decoupled from logging functionality to prevent data loss [169]. The use of a modular architecture allows for enhanced functionality through straightforward upgrades. Proper interrogation, analysis, and troubleshooting of any complications would require the ability to easily review event and signal histories. Alarms should be distinguishable by priority to prevent ‘alarm fatigue’ [169]. Message text should be clear and concise in stating the cause and potential resolutions of an alarm to minimize interpretation. Finally, a remote notification routine would enable doctors and engineers the ability to accurately diagnose and troubleshoot both animal and pump issues without being physically present.

Initial shakedown assessment of each code iteration occurred during *in vitro* hemolysis testing of the PF4 pump to verify system stability, individual feature functionality, and conduct any necessary debugging. The preclinical, *in vivo*, PediaFlow® implants served as the validation

platform for the DSS with observations from the user groups, operator opinions, or noted struggling as the basis to change the GUI layout or upgrade functionality.

4.2.2 Results and Discussion

Since its introduction (**Figure 32**) at the start of first PF4.x hemocompatibility assessment, there have been four major iterations of the DSS program. The DSS software backbone consists of a three-loop parallel process, state-machine structure splitting acquisition, recording, and the operator interface into three separate threads. Separate configuration files save program, calibration, alarm, and flow estimation settings immediately after changing to allow for easy restoration of the previous parameters after a computer crash or failure. A three-second rolling buffer captures the full cardiac cycle for displaying mean signal values, calculating pulsatility index (PI), and determining out-of-bounds alarms. Pop-up menus maintain visibility of the main logging screen while performing any interaction. System responsiveness was maintained by reducing hard drive access programmatically through the use of a custom burst-write data logging algorithm.

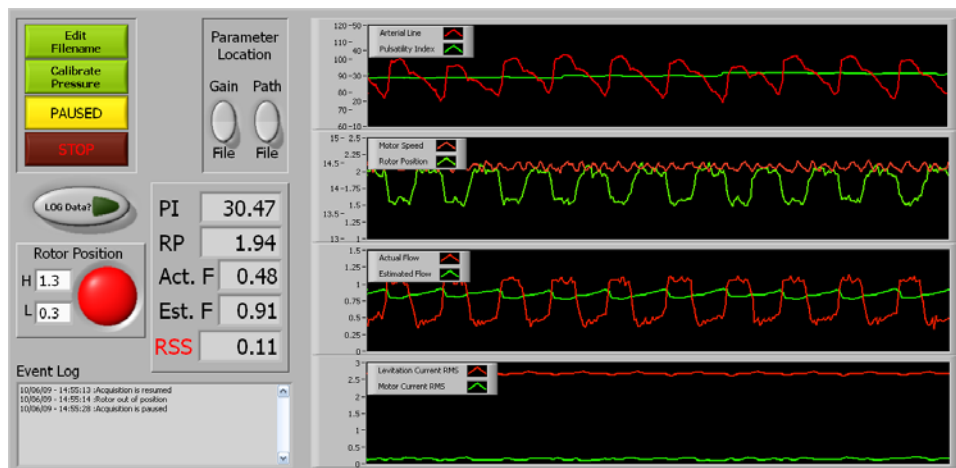


Figure 32. A screenshot of the first DSS1.1 program iteration used both *in vitro* and *in vivo*.

Immediately during the use, the need for each input signal to have its own digital display, alarm limits, a user-enterable linear calibration, and a reprogrammable flow estimator became abundantly evident and was changed in the next version (**Figure 33**).

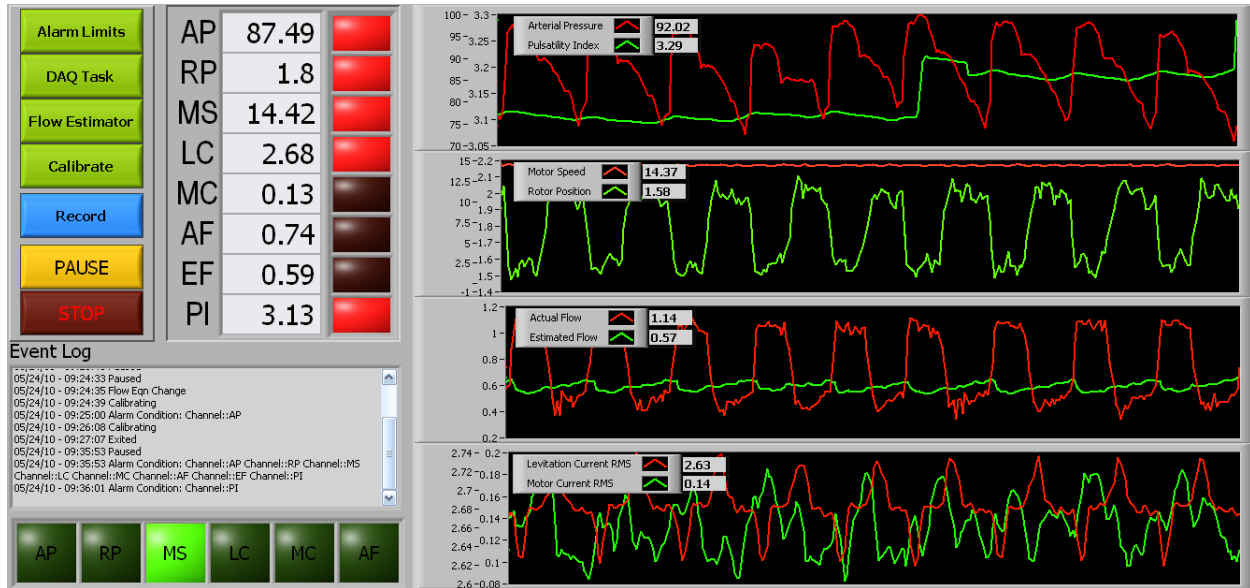


Figure 33. The DSS2.1 during an *in vivo* implant.

Findings from the DSS2.1 included: 1) the desire for inputting a second pressure transducer signal either for pump inlet pressure (*in vitro*) or central venous pressure (*in vivo*), 2) accuracy indicators for the derived parameters (i.e.: estimated flow, and pulsatility index), 3) ability to change the log file path and recording structure from a single file (*in vitro*) or hourly files (*in vivo*), 4) ability to add free text comments to the event log file, and 5) moving workflow from left to right due to screen sharing with the controller software. This is reflected in the third iteration as shown in **Figure 34**.

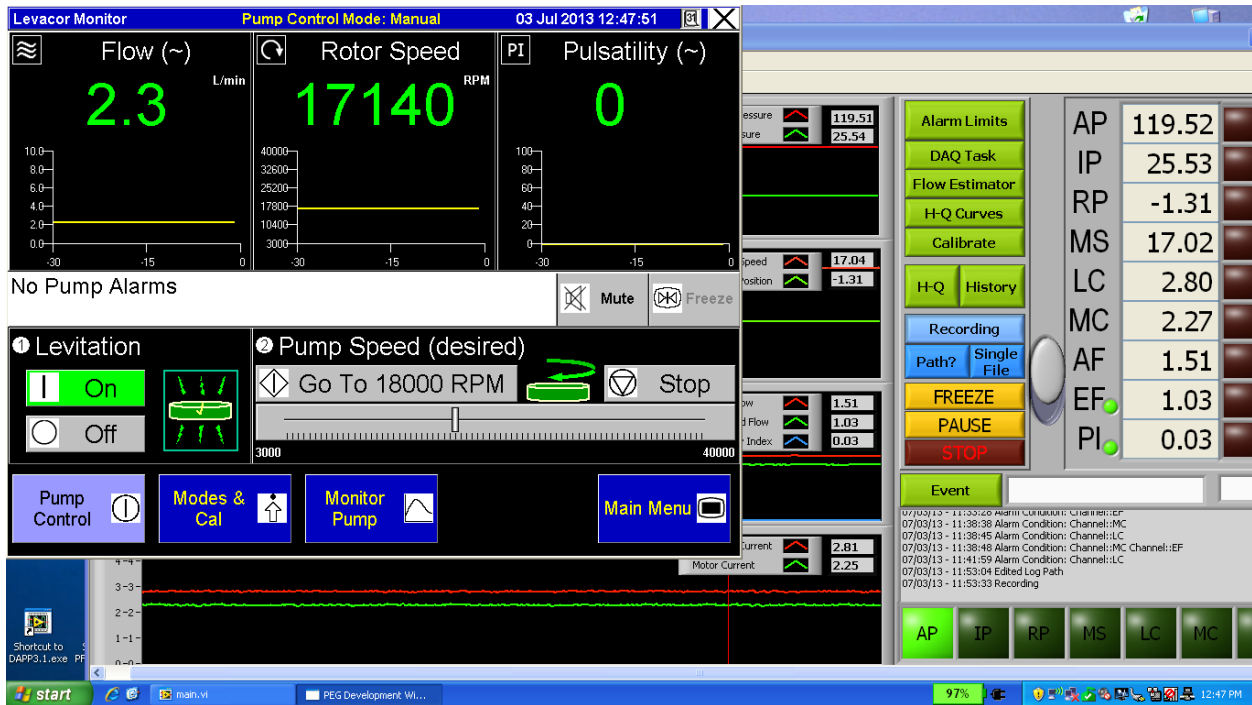


Figure 34. The DSS3.2 and the PediaFlow®/Levacor® pump controller software.

In the latest iteration (DSS4.1), the availability of the internet, through the prevalence of wireless access points, was exploited to provide remote notification and troubleshooting through the SMTP email protocol to desired recipients. The lightweight email sent includes a list of the triggered alarms and a compressed screenshot of the DSS window providing an ~6 sec window of the channel signals centered around the alarm event as highlighted in **Figure 35**. Providing a visual description and context of the alarm prior to receiving the phone call from the animal facility, minimizes the amount of time and information required before walking the veterinary technician through the steps required to rectify the situation. This also reduces the need for continual or overnight monitoring which is unnecessary and cost prohibitive during chronic, stable implants. Also addressed was a long-standing bug, related to the overlap of multiple items with screen refreshing, where the plot charts would occasionally clear and reset. A running

history with multiple timescales is now available, along with a super imposed H-Q curves plot for troubleshooting and a freeze screen for analysis without interrupting logging.

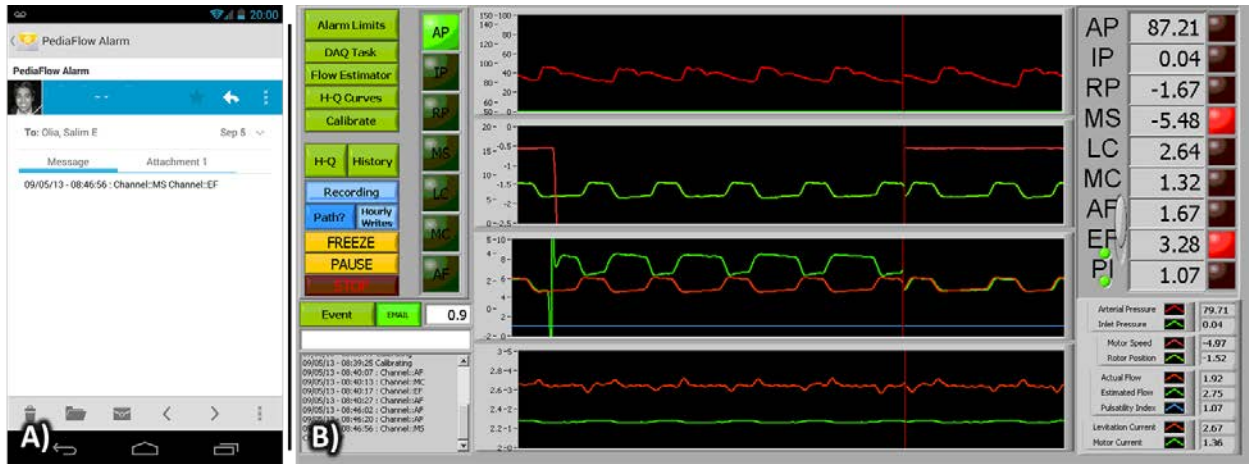


Figure 35. A) An automated DSS4.1 email alarm and attached screenshot (B) sent using the SMTP service.

4.2.3 Future Work

With the DSS platform now fully operational, additional modules can be added for enhanced functionality like the simplified discriminant-analysis based suction detection system proposed by Ferreira, *et al.* moving away from less useful low threshold alarm limits to smarter and more robust algorithms to optimize MCS support [170]. While direct remote access and/or control may appear as the logical next steps, security concerns including university IT policies and firewall restrictions, along with the installation and dependence on additional 3rd party applications, could create unnecessary complications, vulnerabilities, and restrict the compatibility afforded by the out-going only connection afforded by the current design.

4.3 PEDIAFLOW FLOW ESTIMATION

Accurate quantification of MCS D output flow is critical for both patient management and pump control/operation. This section describes the development of the PediaFlow® flow estimation algorithm in support of preclinical *in vivo* PF4 implant studies and moving closer towards a clinical-use device. Due to the failed delivery of a finalized clinical controller from a corporate partner, the PediaFlow® flow estimation algorithm evolved over two distinct iterations to overcome the limitations of the preclinical controllers. Additional accuracy was gained with the second flow estimator by the implementation of two specific hardware upgrades within the controllers as evidenced by the most recent implant.

4.3.1 Introduction

Pump flow rate is an important parameter to quickly *i)* quantify the amount of support delivered, *ii)* optimize device operation, and *iii)* troubleshoot cardiovascular-related symptoms in patients. Simply a function of beat-rate and stroke volume in earlier pulsatile-flow positive displacement MCS Ds, where stroke volume was either fixed (e.g.: Thoratec® XVE & PVAD, Berlin Heart® EXCOR®) or measured using mass airflow sensors (e.g.: Syncardia® TAH, Abiomed® AB5000), the calculated flow rate was both accurate and reliable. On the other hand, the flow rate of a RBP (at any given rotational speed) is dependent on (and inversely proportional to) the resistance, or pressure differential, across the pump. Concerns of hemocompatibility and fouling negate the use of inline, blood-contacting sensors; therefore, most extracorporeal RBPs (e.g.: CentriMAG®, PediMAG®, Tandem Heart®, RotaFlow®) use an ultrasonic, clamp-on, tubing flow probe for measurement of blood flow rate. As evidenced by the HeartAssist5®

(ReliantHeart®, Houston, TX), the only implantable LVAD with an integrated ultrasonic flow sensor, this approach is impractical for implantable RBPs due to several limitations. Because metallic interference necessitates an ultrasonic perivascular sensor located on the outflow graft with a discrete electrical tether, instead of within the pump housing, the HeartAssist5® is larger, less maneuverable, and more complex than similar devices (i.e.: Heartmate II®, Jarvik 2000®) [171].

As motor power consumption is simply work per unit time, all clinically used implantable RBPs (e.g.: VentrAssist™, Heartware® HVAD®, HeartMate® II & 3) estimate flow rate using device (pump) signals, namely motor speed (MS or ω) and motor current (MC), using rotodynamic principles and equations to relate these pump parameters to generated pressure head and flow rate [38, 172-174]. Of note, while all devices report or display the mean flow rate, some RBPs (e.g.: VentrAssist™, HVAD®) also provide the instantaneous flow rate, describing the entirety of the cardiac cycle, as a waveform display.

4.3.2 Materials and Methods

The pump controller, hydraulic, and hemodynamic data necessary for examining these relationships for the PediaFlow® was acquired *in vitro* in both static (**Figure 36**) and pulsatile mock loops using 40% glycerol-solution as a blood analogue. Two pressure transducers (648, PCB Piezotronics Inc., Depew, NY) were connected at the pump inlet (P_{IN}) and outlet (P_{OUT}) while an in-line ultrasonic flow probe (6PXN+TS410, Transonic, Ithaca, NY) was located distally to measure pump flow rate (Q_{PUMP}). The aforementioned hemodynamic parameters and directly available pump controller signals (i.e.: motor speed, motor current, [axial] rotor position, and [axial rotor] levitation current) were acquired and recorded using the DSS (see **4.0**) platform

modified for additional input signals. H-Q curves (see 1.3.2) were generated at several speeds (10-18 kRPM at ~2 kRPM intervals) through the use of the manual tubing-clamp throttle to control afterload in the circulation loop. As every hand-built PF4 pump is operated by a custom-tuned controller, with variable performance characteristics and signal signatures, this process was repeated for each PF4.x prototype-controller pair to create unique datasets for subsequent analysis and derivation of the flow estimation parameters.

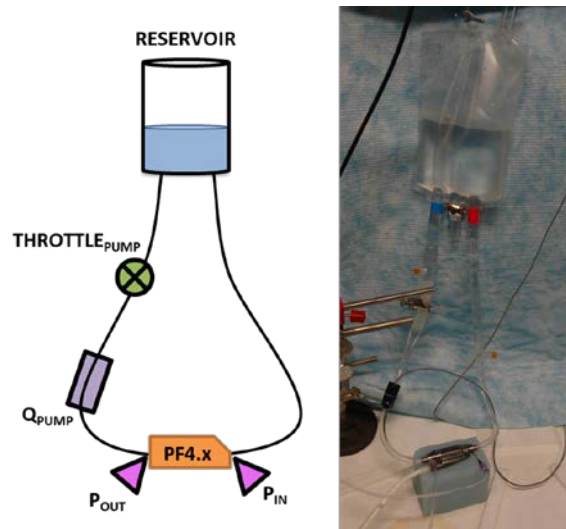


Figure 36. A schematic (left) and example image (right) of the simple static loop used for H-Q testing to acquire hemodynamic and PF4 controller values under steady, non-pulsatile conditions.

The mock circulatory system to acquire hemodynamic (H-Q curves) and controller data under pulsatile-flow conditions consisted of a silicone ventricle (Pulse Duplicator, ViVITRO Labs® Inc., Victoria, BC, Canada) actuated by a fixed, pneumatic driver (Utah-TAH preclinical controller). As shown in **Figure 37**, the PF4.x prototype was placed parallel to the single ventricle system, with an additional throttle to adjust systemic vascular resistance (SVR) while a second in-flow probe (13PXN+TS410, Transonic Systems®, Ithaca, NY) measures total cardiac output (Q_{CO}).

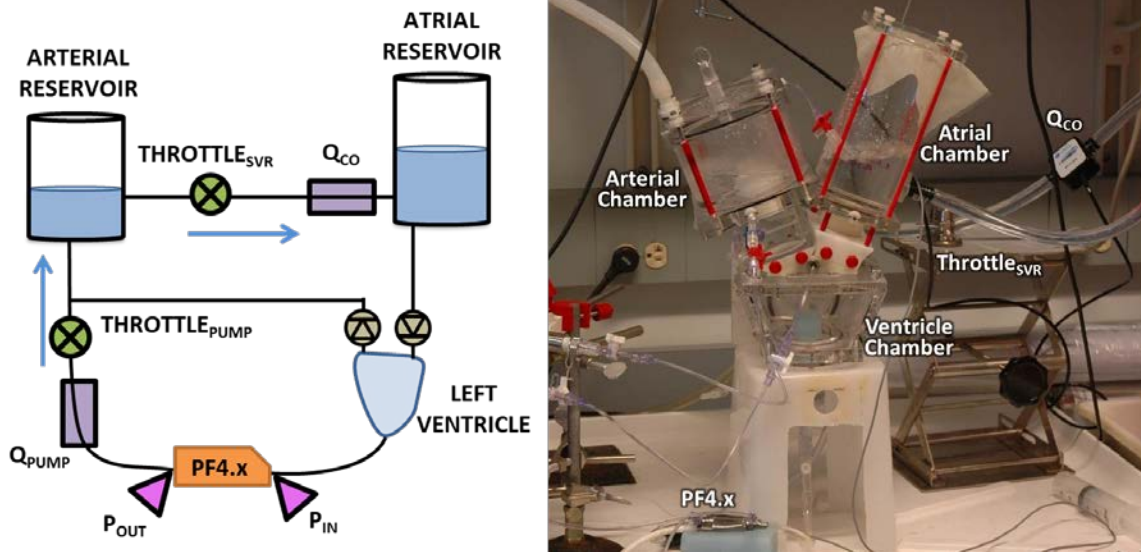


Figure 37. The schematic (**left**) and actual setup (**right**) of the pulse duplicator setup mimicking PF4 pump operation *in vivo* for acquiring the H-Q data under pulsatile-flow conditions used to develop the parameters and coefficients for flow estimation.

All processing, analysis, modeling, and fitting of the recorded data was done in MATLAB/Simulink (MathWorks, Natick, MA). A 10 Hz low pass filter was utilized on each signal, and all flow estimation coefficients were derived from the mean values of the *in vitro* pulsatile mock loop data. Validation was performed using PF4 *in vivo* implant signal data and compared against measured pump actual flow (AF) provided by a perivascular, transit-time ultrasonic flow probe (PS-series+TS420, Transonic, Ithaca, NY) placed on the outflow graft.

4.3.3 Results and Discussion

Identical in both hydraulic and topological design, the H-Q curves of the PF4 under steady conditions *in vitro* were similar across the PF4.x prototypes, as expected (see **Figure 38**, in red). Minute variations in the static performance between the hand-built pumps are instead namely

attributable to (in descending order): i) variable aqueous glycerol viscosities, ii) fabrication tolerances, and iii) motor-controller pairing differences.

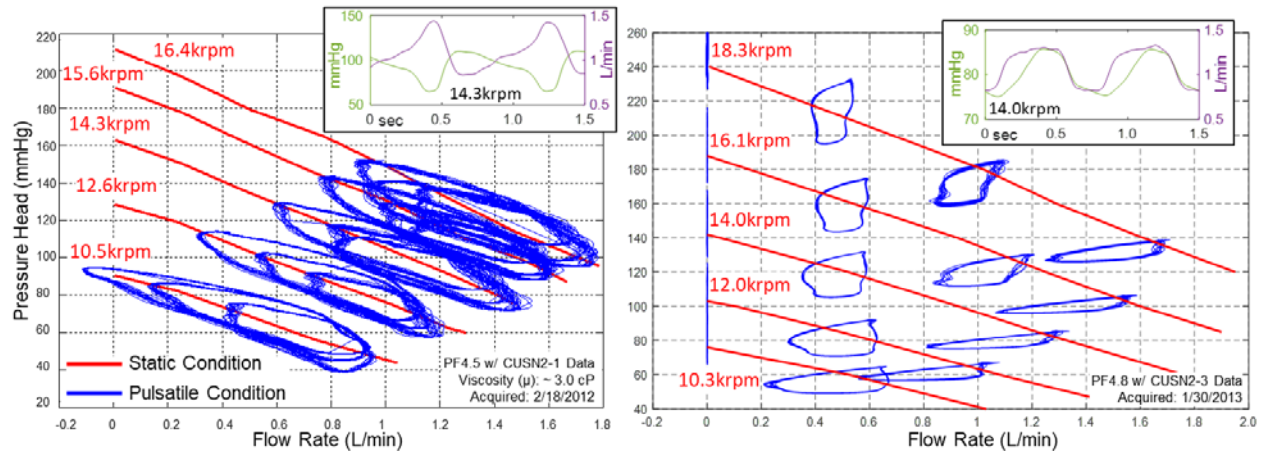


Figure 38. H-Q plots for two PF4.x prototypes generated from the *in vitro* mock loop experiments, representative of i) pump performance under steady versus dynamic conditions, ii) the hysteresis present in the latter, and iii) the differing signal phase offsets (**inset**) between the two pulsatile datasets accountable for the different loop shapes (**inset**).

In contrast, while the pulsatile results approximate the static data in each pump, the H-Q ‘loops’ varied considerably between the prototypes as shown in the example (**Figure 38**, in blue). This rate-dependent hysteresis, a function of pulsatility due to fluid inertial effects (from the beating heart/ventricle), presents natively *in vivo* as flat wide curves that narrow and steepen with increasing pump speeds in accordance with Starling’s response [175, 176]. The atypical and variable shape H-Q ‘loops’ here can be explained by; 1) changes in phase offset of the pressure and flow inputs among experiments (**Figure 38-inset**) due to i) flow meter signal conditioning delay and/or ii) dampening due to insufficient de-airing of the pressure transducers, and 2) the throttle adjusted control afterload as demonstrated by **Figure 39-A**.

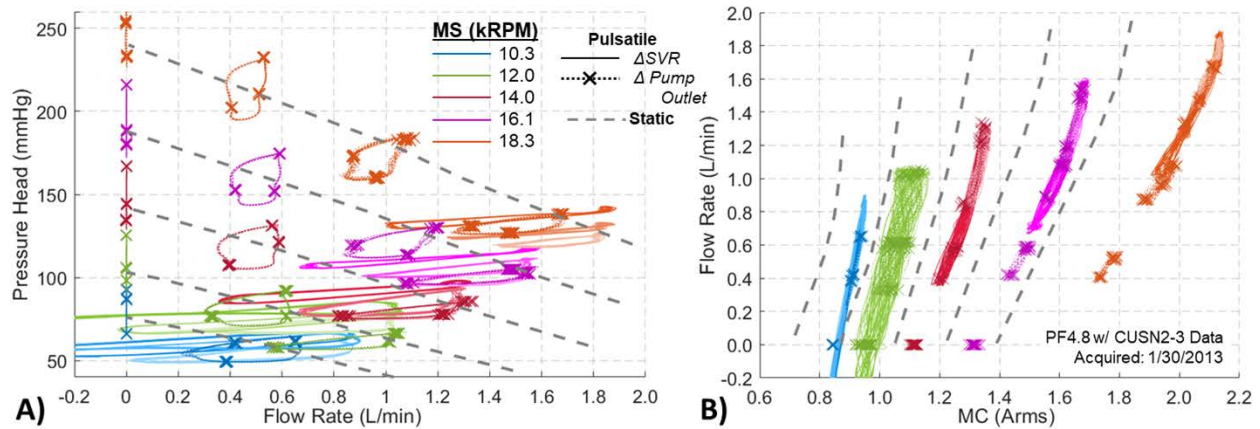


Figure 39. Signal measurements of PF4.x prototype generated under pulsatile conditions by adjusting either pump ($THROTTLE_{PUMP}$) or systemic ($THROTTLE_{SVR}$) afterload with the resultant (A) H-Q plot and (B) relationship between flow rate and motor current (MC).

All flow estimators in clinically-used RBPs are based primarily on motor speed (MS or ω) and motor current (MC), since power consumption is essentially proportional to flow rate over the physiologically relevant range [38, 173, 174, 177]. While flow is typically a multivalued function of power in axial pumps due to friction and internal energy losses at low flow rates [177], the fully magnetically levitated PF4 has a singular relationship between flow rate and MC throughout its entire operating range as evidenced by **Figure 39-B**.

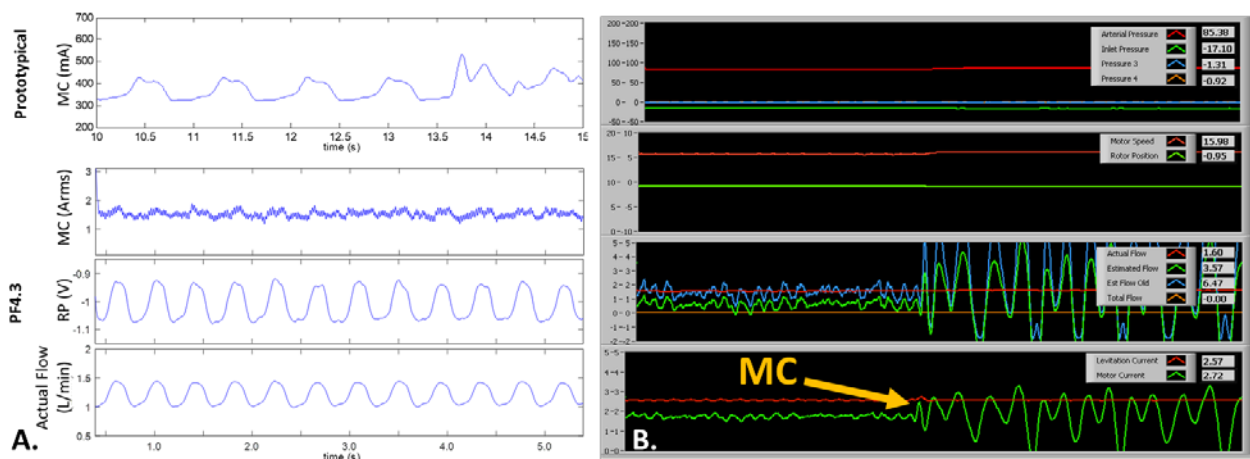


Figure 40. Motor current signal shortcomings with the original PF4 preclinical controllers. A) An *in vivo* MC signal from a prototypical maglev VAD able to distinguish the cardiac cycle in comparison to the PF4.3 and

controller with poor MC resolution but a rotor position (RP) signal reflective of the measured flow rate. **B)** At specific speeds (e.g. $\omega \sim 16$ krpm), the controller MC signal became erratic with negative values preventing the use of any flow estimator utilizing MC.

The ability to provide instantaneous flow, important for assessing LV unloading and suckdown events, necessitates distinguishing the cardiac cycle from available pump signals. The PF4 motor with the original sensor board on the preclinical controller yielded a noisy and non-characteristic MC signal that was unacceptable for estimating flow rate due to being both inaccurate (**Figure 40-A**) and erratic at select operating speeds (**Figure 40-B**). Due to the unique MagLev design configuration of the PF4, the rotor position (RP) sensor used for the active levitation control mechanism in the axial direction provided an alternative signal reflective of the measured, actual flow (AF) waveform.

Original Regression Model

Since the rotor position (RP) signal is proportional to the pressure head across the pump, the initial flow estimator was based on a regression model using RP and MS:

$$Q = X * a,$$

$$X = [1 \ \omega \ RP \ \omega * RP \ RP^2]$$

where ' Q ' = flow rate (L/min), ' ω ' = motor speed (kRPM), ' RP ' = rotor position (Volts) and the coefficients of array ' a ' were determined for each pump build from the mean signal values of the *in vitro*, pulsatile data.

While able to estimate instantaneous and mean flow rates *in vivo*, this 'RP/MS regression' was susceptible to RP inaccuracies including drift over time after implantation,

attributed to the temperature difference between the sensor coil within the pump and the sensor circuitry within the controller, as evident in **Figure 41**.

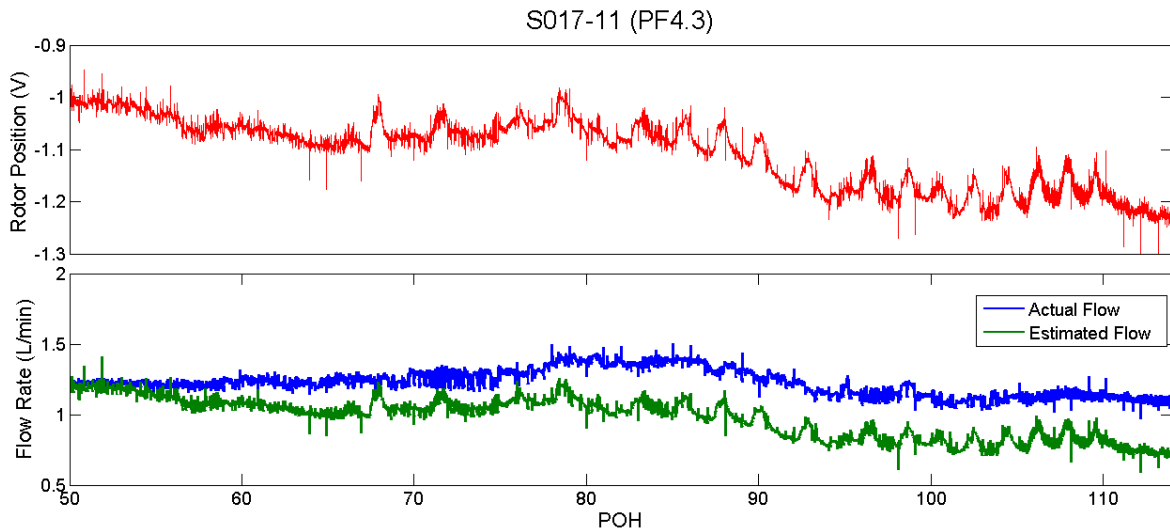


Figure 41. Rotor position (RP) signal drift (red) over the 115 post-operative hour (POH) period and ‘RP/MS regression’ flow estimator compared to the flow probe measurement (blue).

Dimensional Analysis Model

The inability to rely solely on absolute RP led to the adoption of a dimensional analysis approach to yield a robust estimation algorithm [178, 179]. Using pump-specific, physical and electrical constants, the PF4 characteristics at each operating speed can be nondimensionalized into three coefficients; pressure (Ψ), flow (Φ), and power (Π):

Table 3. The pump constants, parameters, and measurements for dimensional analysis, and the three nondimensional characteristic coefficient equations for the flow estimator algorithm.

H	Head pressure	mmHg
RP	Rotor position	V
μ	Dynamic viscosity	Kg/m*s
ρ	Density	Kg/m ³
ω	Speed	rpm
D	Diameter	cm
Q	Pump flow	L/min
MC	Motor current	Arms
P	Power	W
c_Ψ	Head coefficient constant	1.2157E+5
c_Φ	Flow coefficient constant	159.161
c_Π	Power coefficient constant	8.7082E+9

Pressure coefficient:

$$\Psi = c_\Psi \frac{H}{\rho \omega^2 D^2}$$

Flow coefficient:

$$\Phi = c_\Phi \frac{Q}{\omega D^3}$$

Power coefficient:

$$\Pi = c_\Pi \frac{P}{\rho \omega^3 D^5}$$

The original approach was to characterize Φ as a function of Π , through benchtop testing, which would then enable the calculation of flow rate through the estimation of the flow coefficient from ω and MC. Encountering the same quality issues with MC which lead to poor correlation between the power and flow coefficients, a modified approach was instead taken that utilized the relationship between the pressure and flow coefficient (**Figure 42**). Since pressure drop across the pump can be accurately estimated from coupling MC to RP and yielding the pressure coefficient, the hybrid approach characterized Φ as a function of Ψ to then enable the calculation of flow rate from all three relevant pump signals (ω , RP, and MC).

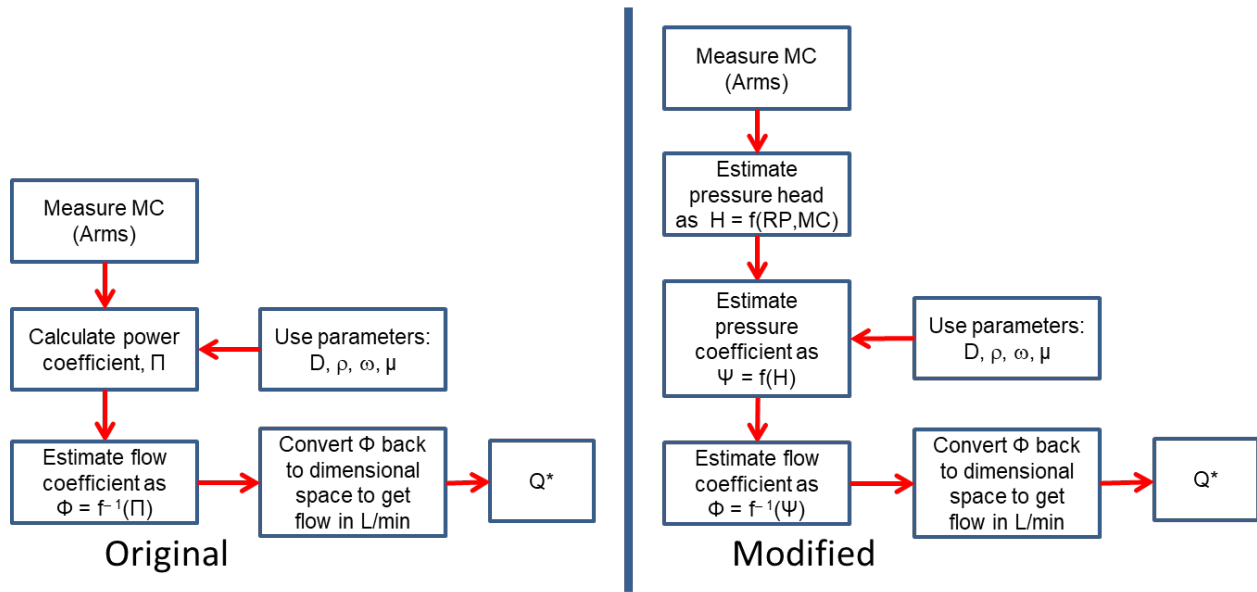


Figure 42. The original (left) and modified (right) algorithm for the dimensional analysis PF4 flow estimator.

The use of dimensional analysis with the three pump signals eliminates introducing motor current noise into the flow waveform while making the mean flow rate less susceptible to RP sensor drift. This estimator was used for PF4.6.1 when implanted for nine days (S044-12) as shown in **Figure 43**; the trend for RP, MC, and flow rates are shown on the left, while the right is a snapshot of six beats showing the noise of the MC isolated from the flow estimator.

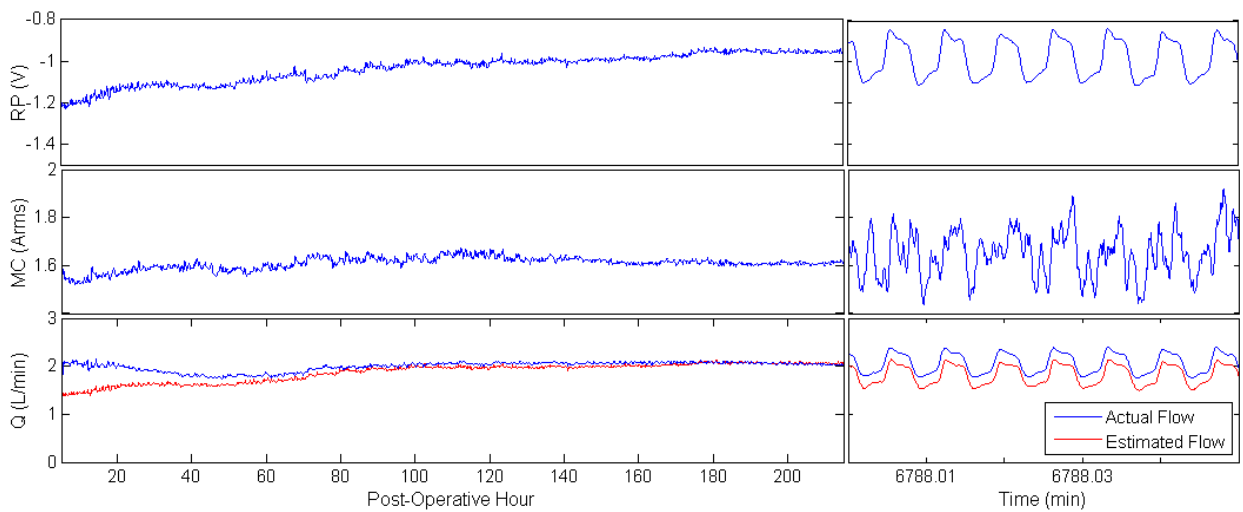


Figure 43. S044-12 (PF4.6.1) implant showing the overall parameter trends (left) and a signal snippet (right).

Controller Hardware Upgrades

Due to the 3-phase, 4-pole motor configuration of the PF4 and the fixed sampling frequency of the controller, the controller sensor measures a combination of actual and decayed motor current yielding the high frequency noise and resonance seen on the MC signal. After the indefinite suspension in the delivery of a clinical controller which would have addressed the signal quality, a ‘sample and hold’ alarm filter board was designed and fabricated for use within the preclinical controllers currently in use. Additionally, circuitry for temperature compensation was added to reduce the effect of temperature variations between the pump and controller on RP drift. The results of this additional circuitry are exemplified in the 60-day in vivo implant (PF4-S010, see 5.0) shown in **Figure 44**, where RP remained stable and the cardiac cycle can be seen within the MC signal.

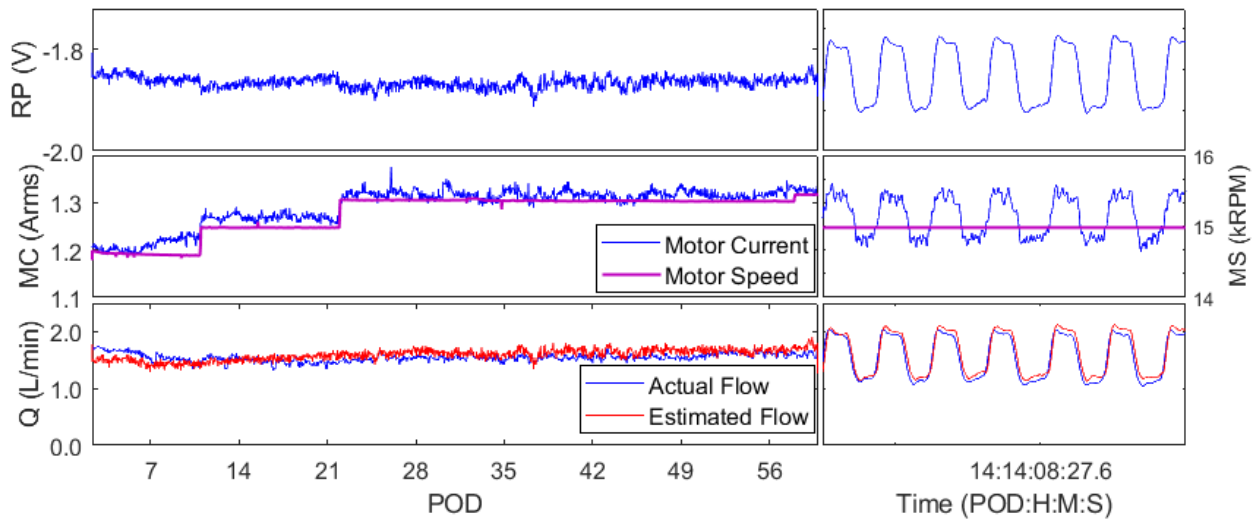


Figure 44. S011-13 (PF4.6.1) with the upgraded controller showing the overall parameter trends (**left**) and a signal snippet showcasing the enhanced MC signal (**right**).

4.3.4 Future Work

The ability to now accurately measure both MC and RP, due to the PediaFlow® preclinical controller upgrades, provides for an estimation that is more robust than current algorithms that only use MC, MS (ω), and occasionally blood viscosity (μ). The quality of the MC signal warrants revisiting the original dimensional analysis approach of characterizing the flow coefficient as a function of the power coefficient for flow estimation. With the addition of RP for estimating the pressure coefficient, changes in pump efficiency due to thrombus or electrical failure could be detected instead of reporting erroneous flow rates for smarter troubleshooting.

5.0 PRECLINICAL PERFORMANCE OF THE 4TH GENERATION PEDIAFLOW® PEDIATRIC VAD

This chapter describes the *in vitro* and *in vivo* efforts to evaluate the hemocompatibility and biocompatibility of the PF4. The experimental findings and subsequent design changes presented here were both an impetus and a product of the work described in the previous chapters, with the two most-recent implants representing the preclinical performance to date of the current PediaFlow® implantable system. This chapter in part was published in The Journal of Thoracic and Cardiovascular Surgery [1]

5.1 METHODS

5.1.1 *In Vitro* Assessment

Benchtop evaluation of the PF4 design was performed to confirm hemodynamic performance and characterize hemolysis potential. Using the developed standards (see 2.4), *in vitro* hemolysis testing was performed on several PF4 prototypes (Appendix C, Table 5) prior to *in vivo* implantation using purchased, citrated ovine whole blood (Lampire® Inc., Ottsville, PA) with a minimum total plasma protein concentration of 6.0 g/dL within three days of venipuncture [35,

84, 143, 144]. The clinically utilized, centrifugal PediMag® (Thoratec®, Pleasanton, CA) pump served as a control for comparison.

5.1.2 *In Vivo* Evaluation

Under UoP Institutional Animal Care and Use Committee approved protocols at the McGowan Institute's Center for Preclinical Studies, six PF4 prototypes were implanted in lambs (n=11, 19.0-30.3 kg) without cardiopulmonary bypass to evaluate the chronic *in vivo* hemodynamic performance and biocompatibility of the PediaFlow® and develop the implantable components (**C.2, Table 8**). Anesthesia, surgical approach, insertion, and post-operative management for the PF4 implants were similar to the 72-day PF3 implant described previously [132, 134]. Three sham studies, in which the aforementioned implant procedure was followed without actual device placement, were performed to serve as complementary 'surgical controls' (**C.2.2**). Blood samples were drawn at regular intervals during the course of the studies for hematology and biocompatibility assessments, including plasma-free hemoglobin, fibrinogen concentration, and platelet activation and functionality assays, followed by a complete necropsy and pump component examination [132, 159]. A summary of the initial PF4 implant findings (**C.2**), design modifications (**C.1**), and outflow graft iterations (**C.1.2**) can be found in **Appendix C**.

5.1.3 Current PF4 Implantable Design

Detailed here are the most recent PF4 implants (n=2) using the *de novo* designed 5 mm reinforced parabolic-tip inflow cannula (**3.2.1**) featuring a parabolic-shaped inlet entrance and detachable sewing ring to unload the left ventricle (**Figure 45-B**) and a 6 mm Gelweave®

(Vascutek® Ltd, Renfrewshire, Scotland, UK) outflow graft with graduated strain relief to return blood to the aorta (**Figure 45-C**) [152].



Figure 45. The PF4 PediaFlow® prototype and implantable components : **A)** the PF4 pump, **B)** the parabolic-tip inflow cannula with detachable sewing ring, and **C)** the pre-assembled 6 mm outflow graft assembly.

Surgical procedure with these implantable components varied only by first attaching the detachable sewing ring to the left ventricle (LV) apex using pledgeted sutures after gaining access. Following full anticoagulation with heparin, the outflow graft was anastomosed to the descending thoracic aorta and back-flushed before mating the graft connector to the pump outlet. The parabolic inflow cannula was inserted through the sewing ring after a cruciate incision without myocardium removal and a wet connection made to the pump inlet by the simultaneous removal of the inflow obturator and partial unclamping of the outflow graft. A perivascular ultrasonic probe (Transonic Systems®, Ithaca, NY) was placed on the outflow graft to measure pump flow rate. Pump support was initiated and cannula depth optimized before thoracotomy closure. Rotational speed was adjusted as needed for a target flow rate of 1.5 L/min.

5.2 RESULTS

Hemolysis (NIH) *in vitro* varied somewhat among PF4 prototypes but was very low at the three pediatric flow rates tested and comparable to the PediMag® control (**Figure 46**).

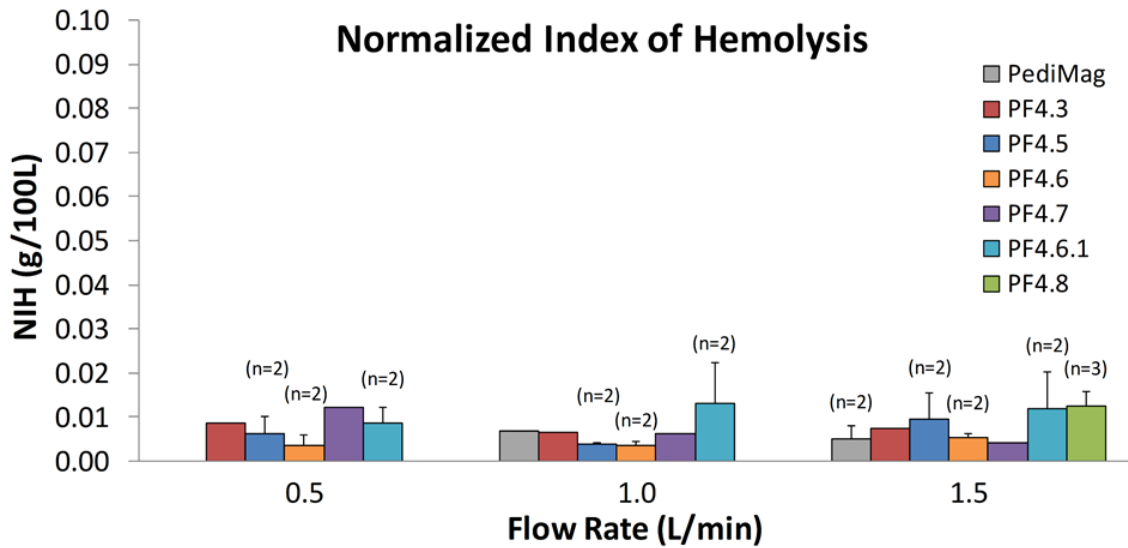


Figure 46. The calculated *in vitro* Normalized Index of Hemolysis (NIH) values (mean±SD) for the PF4.x prototypes compared to the PediMAG® control.

The last two implants with the PF4 prototypes and implantable components were unremarkable for a study duration of 14- and 60-days. Pump support was initiated within an hour after first incision, achieving flow rates up to 2.0 L/min before reducing motor speed (RPM) to maintain a target flow rate of 1.5 L/min following chest closure (**Figure 47-A**). Due to the difficulty of titrating anticoagulation for an activated clotting time (ACT) target of 180-200 s during the previous PF3 study, a continuous infusion of heparin was maintained at 20 UI/kg/hr beginning on post-operative day (POD) 2 and 7 for PF4-S10 (60-day implant) and PF4-S11 (14-day implant), respectively (**Figure 47-D**).

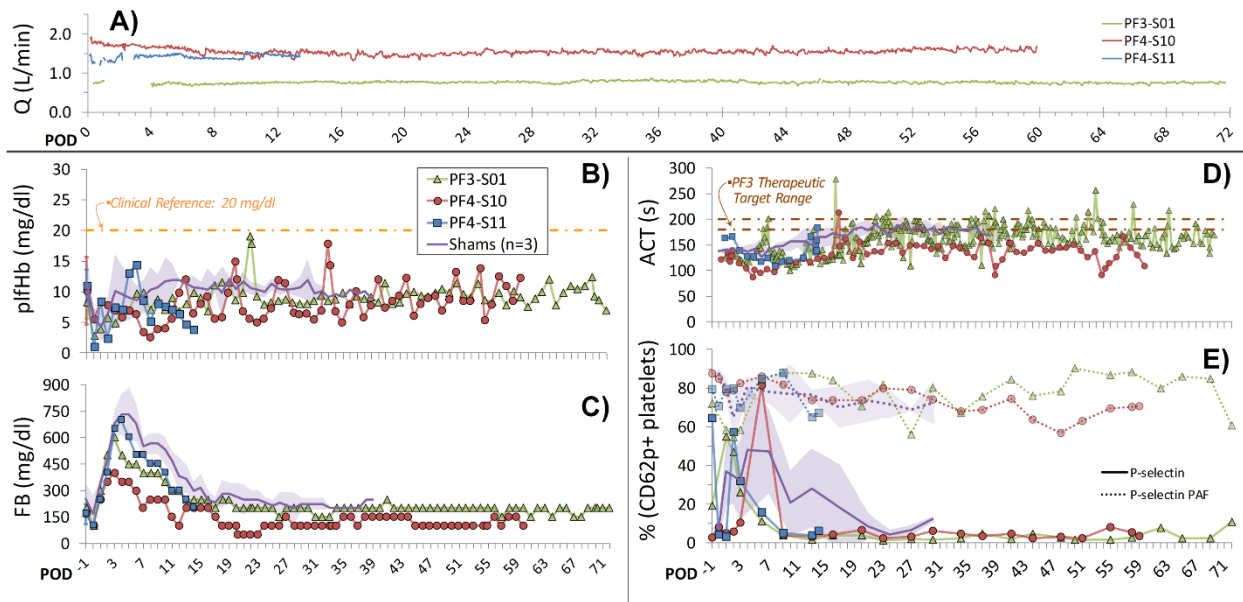


Figure 47. Results of the two PF4 ovine studies using the current-design cannulae system (PF4-S10, PF4-S11), in comparison to the previous 3rd-gen. chronic implant (PF3-S01) and the non-implanted surgical control ‘Shams’ (n=3, mean±SD): **A)** Measured pump flow rate (Q) for the implanted animals (gaps indicate durations of signal loss during post-operative acoustic recoupling of the outflow graft probe). Hematological and hemocompatibility measurements including **B)** plasma-free hemoglobin, **C)** fibrinogen, **D)** activated clotting time (ACT), and **E)** platelet biocompatibility as determined by the time course of platelet activation by P-selectin expression and platelet functionality by agonist stimulation using platelet activating factor (PAF).

During the PediaFlow® implants, hemodynamic performance was within the pediatric physiological range, while serum chemistry, hematology and cellular biocompatibility parameters closely followed the trends observed in the three surgical control sham studies (**Table 9**). Plasma-free hemoglobin remained within pre-operative levels and fibrinogen concentration values for the implants and surgical control animals returned to baseline by POD 14 (**Figure 47-B, C**). Platelet activation, measured by flow cytometry as percent of CD62p+ platelets, had a marked post-surgical response before returning to pre-operative baseline values by POD 10.

Throughout the studies, platelets remained responsive to stimulation with platelet activating factor (**Figure 47-E**).

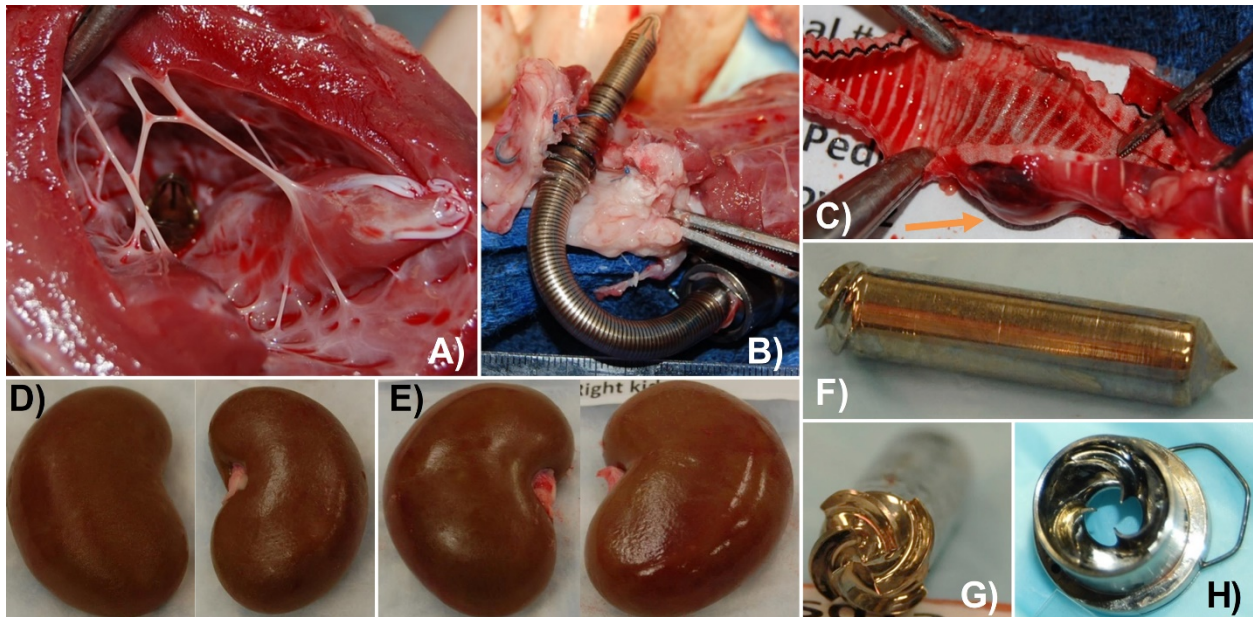


Figure 48. Necropsy images of PF4-S11 (14-day) implant. **A)** the inflow cannula position in situ, **B)** cannula body free of deposition, **C)** adherent thrombus on the exterior of the outflow graft, outside of the blood flow path, possibly from the de-airing needle, **D-E)** kidneys without evidence of infarcts, and **F-H)** rotor, impeller blading, and stator free of deposition.

Examination of the heart, lungs, liver, and spleen for the latest PF4 implants was unremarkable. The inflow cannulae were well healed within the LV apex with no myocardial injury evident, and the blood contacting surfaces of the pump, cannulae and outflow grafts free of adherent thrombus (**Figure 48 & Figure 49**). No surface lesions or infarcts were found on the kidneys of the two PF4 implants (**Figure 48-D,E & Figure 49-G**).

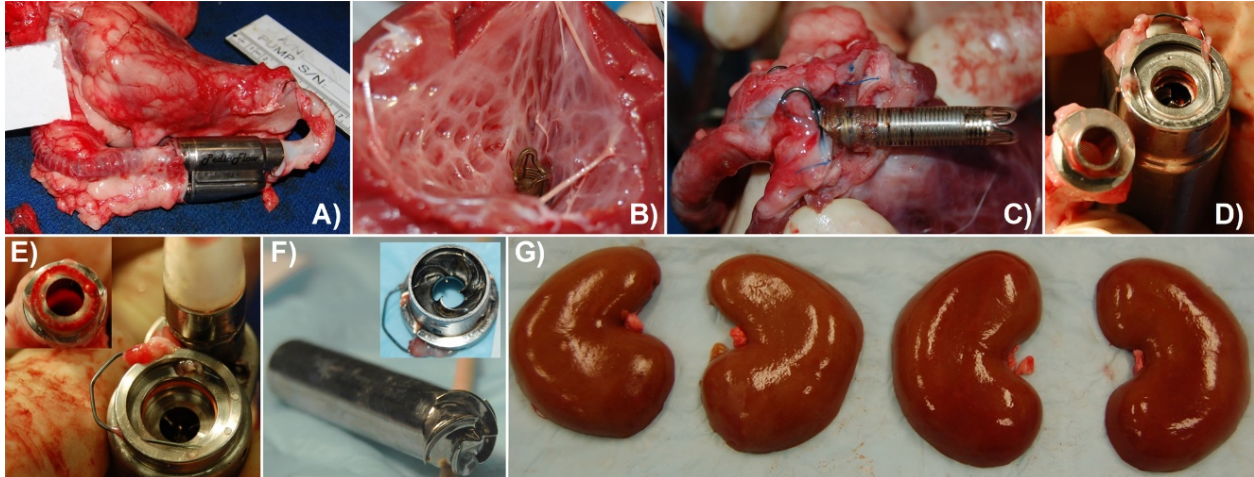


Figure 49. Explant photos of the PF4-S10 (60-day) implant. **A)** well encapsulated pump *in situ*, **B)** the inflow cannula tip position, **C)** the cannula body, **D)** inflow and **E)** outflow connections free of deposition within the flow path, **F)** the pump rotor and stator (**inset**) free of deposits, **G)** kidneys with no evidence of infarction.

5.3 DISCUSSION

Implantable pediatric VADs have the potential to expand the number of children in heart failure rescued by MCS [180]. The use of RBPs for the treatment of pediatric heart failure is appealing by reducing the immobilization and hospital in-patient restrictions that are currently associated with the EXCOR®. While the successful miniaturization of CF VADs will impact pediatric MCS options, the small market size and regulatory processes create a significant entry barrier for this technology in the United States. Supported by the bench and pre-clinical findings reported here, the PediaFlow® has the potential to serve as a bridge-to-transplant or bridge-to-recovery device.

Consistent with the program goals for the two NHLBI contracts under which this work was conducted, the primary considerations for the design and development of the PediaFlow®

were miniaturization and reduction of serious adverse events by maximizing cellular biocompatibility, as judged on the bench and *in situ* [134, 181, 182]. *In silico* optimization of the rotodynamics, magnetodynamics, heat transfer, and fluid dynamics yielded four successively smaller prototypes that were built and tested both *in vitro* and *in vivo*. **Figure 4** displays the marked reduction in profile of the PediaFlow® design in successive generations of prototypes (PF1 – PF4), with the PF4 prototype approximating the size of an AA cell battery (**Figure 45-A**). By increasing the voice (levitation) coil to motor stator size-ratio to enhance rotor stability and optimizing the pump blading from PF3, flow rates were improved enabling PF4 to reach the target design goals. With an NIH of < 0.02 g/100L for the final PF4 prototypes, the PediaFlow® PF4 device is non-hemolytic (e.g., the NIH for the PF4 approximates that of the maglev PediMag®) and less than published literature values for both adult and pediatric devices [143, 146, 183]. We attribute the absence of hemolysis to the fully magnetically levitated rotor design, the optimized single blood flow path, and relatively large annular gap (1.5 mm), which eliminates the need for bearings or seals, thereby reducing hemolytic potential. As each PF4 pump was hand-built, the variation in NIH among prototypes is likely due to assembly and polishing tolerances.

Another design consideration for the PediaFlow® technology is that pediatric MCS should be rapidly deployable and customizable to support the representative patient population. The use of cardiopulmonary bypass for VAD implantation is expected, however limiting on-pump time remains ideal. Within this context, and for the PediaFlow® inflow cannula, the removable sewing ring provides accurate and unencumbered placement onto the heart apex before allowing insertion and tool-less securement of the inflow body within the LV. The reinforced parabolic-shaped inflow tip (**Figure 45-B**) eases insertion and serves as a clinical

marker for echocardiography peri-operatively to adjust insertion depth and post-operatively when assessing cannula position. Along with the pre-assembled outflow graft and quick connect mechanisms (**Figure 45-C, C.1.3**), pump support was initiated in the latest studies in under an hour from first incision without the use of cardiopulmonary bypass. Without any evidence of ventricular suction supported by explant analysis in the PF3 and PF4 implant studies, we hypothesize that the additional flow paths provided by the inlet shape geometry render the parabolic-tip resistant to entrapment and less sensitive to positional variations [152].

While *in vivo* analysis is performed in healthy animals and does not necessarily reflect the etiologies of heart failure in children (i.e.: congenital, dilated, and/or restrictive cardiomyopathies), the results are nonetheless encouraging. The biocompatibility findings *in vivo* (**Figure 47**) and explant analyses (**Figure 48 & Figure 49**) are consistent with the *in vitro* results demonstrating no hemolysis, and neither platelet activation nor platelet dysfunction during implant periods up to 2-months. The lack of documented renal insufficiency or other evidence of thrombosis or thromboembolic events with only relatively low-dose heparin and sub-therapeutic ACTs is especially promising towards the design goal for the PediaFlow® pediatric VAD of solely anti-platelet therapies to minimize bleeding risk clinically [181, 182]. Additional implants using the current PF4 design and components are necessary to demonstrate reproducibility of the preclinical assessment for Investigation Device Exemption (IDE) application.

5.4 CONCLUSIONS

This report is the culmination of 10-years of NHLBI-supported development of a miniaturized, implantable rotary blood pump for the chronic support of infants/small children with congenital

and/or acquired cardiac defects. Over 20 design variations were evaluated and judged based on a multi-component objective function which factored several criteria including anatomic fit, cellular biocompatibility, heat generation and transfer, magnetically levitated suspension robustness, and manufacturability [134]. The design was improved and miniaturized through successive pump prototypes using computational fluid dynamics to minimize flow-induced blood damage via modification of the geometry of the predicted blood flow path [135]. The pump housing was modified to improve surgical fixation and the inflow/outflow attachments optimized to permit ease of insertion according to human factors engineering principles.

The data presented herein document the exceptional biocompatibility and the potential of safely providing chronic mechanical circulatory support to neonates and infants using a miniature, implantable, magnetically levitated, rotodynamic blood pump. As per the requirements of the NHLBI contract programs, the PediaFlow® has been designated by the FDA as a Humanitarian Use Device (HUD) for “mechanical circulatory support in neonates, infants, and toddlers weighing up to 20 kg as a bridge to transplant, a bridge to other therapeutic intervention such as surgery, or as a bridge to recovery.” This important designation provides insight as to the remaining pre-clinical testing (both on the bench and *in vivo*) to be undertaken. While accurate flow estimation has been achieved (**4.3, Figure 44**), work remains including the final prototyping and testing of a clinical-use controller which is required for the final preclinical studies in anticipation of submitting an IDE application to the FDA.

6.0 FINAL CONCLUSIONS AND FUTURE DIRECTIONS

The development of a pediatric-specific mechanical circulatory support device is both complex and perilous, as evidenced by the lone contractor remaining within the NHLBI PumpKIN trail [183]. Size remains the recurrent theme and obstacle throughout, whether in relationship to the i) device, ii) pump gap, iii) controller, iv) percutaneous driveline, v) mechanical blood trauma, or vi) market cap. Simply put, children are not “small adults”.

This dissertation describes the efforts undertaken to support the design, optimization, and evaluation of the 4th generation PediaFlow® pediatric VAD and implantable system. A pediatric-appropriate *in vitro* mock loop for benchtop mechanical blood trauma evaluation was developed and successfully implemented. A novel suction-resistant pediatric inflow cannula designed for optimal unloading and ease of implantation was created and validated. Finally, an MCS-specific DAQ system for preclinical testing was programmed and used effectively during *in vivo* animal implantations. This work along with the associated findings are largely applicable for all pediatric RBP under current and future development, as well as next-generation partial-support adult MCSDs too. However, additional avenues remain unaddressed and provide future opportunities for exploration, analysis, and development.

6.1.1 *In Vitro* Blood Trauma Testing

As MCS hemocompatibility continues to improve with each subsequent generation, continued evaluation and comparison of MCS biocompatibility will require both improving overall experimental sensitivity and finding new markers for pump-induced trauma. While reducing circulating blood volume and blood pool variability would enhance standard benchtop *in vitro* mechanical blood trauma testing, the current accepted practice of solely assessing lethal RBC hemolysis through free hemoglobin should also be expanded to include additional blood trauma components (e.g.: von Willebrand Factor degradation, platelet activation, sublethal RBC damage) reflective of on-going clinical complications. (i.e.: GI bleeding, thrombosis, stroke, chronic anemia). Furthermore, increasingly popular, transmyocardially-implanted RBPs for pediatric or partial support in adults should encourage the continued development of an intraventricular-appropriate MCS reservoir for *in vitro* circulation and benchtop evaluation.

6.1.2 Sublethal RBC Damage

Additional research is needed to further elucidate the factors, thresholds, and boundaries that define the realm of sublethal RBC trauma. A profile should be developed that describes sublethal RBC damage as a function of shear stress, exposure time, and cumulative history. This would be similar to how the “Leverett curve” has been used to suggest the hemolytic threshold between shear stress and exposure time [23, 34, 59, 184, 185].

6.1.3 Outflow Graft Permeability

The serious complications (i.e.: excessive serous chest drainage, plasma protein loss, local intra- and extra-luminal thrombus) noted during the initial PF4.x *in vivo* implants utilizing an ePTFE-based outflow tract (C.1.2) warrant further investigation to elucidate the potential implications (e.g.: plasma weep, thrombogenicity) of different vascular prosthesis compositions under the supra-physiological hemodynamics associated with VAD-applications.

6.1.4 DSS Functionality

In addition to the future diagnostic functionality (i.e.: flow estimation accuracy, pump thrombosis and LV suction detection) described above, a proper human factor analysis to characterize the GUI and response times between different users to acknowledge, manipulate, troubleshoot, and the resolve various scenarios would qualitatively validate the software and potentially identify areas of redesign or improvement to be made.

6.1.5 Transfusions During MCS

Acknowledging of the effects of storage lesion and the blood trauma induced from blood pumps, it appears paradoxical to transfuse patients on mechanical circulatory support where it will be immediately cleared. A study published in the New England Journal of Medicine (NEJM) showed no difference in outcomes for critical condition (not MCS-specific) patients who were transfused when blood hemoglobin dropped below a threshold of 7 g/dL versus 10 g/dL [186]. Even more promising, a community teaching hospital saw a 28.6% reduction in associated

complications after implementing an interventional monitoring program requiring physician adherence to restrictive transfusion criteria and blood product delivery protocols [187]. In the absence of active bleeding and clinically intolerable anemia, there is no evidence to suggest that blood transfusions improve outcomes of patients on MCS.

An avenue for exploration is the use of fresh blood products or erythropoiesis-stimulating agents for use in MCS patients. Comparison of these interventions to current practice *in vitro* and *in vivo* to assess clearance rate (via hemolysis and/or cellular markers) and relevant clinical parameters, may yield vital data for improving outcomes through the development of MCS-specific critical care policies. The use of bone marrow-stimulating therapies (e.g.: erythropoietin) may encourage native production of healthier and well deformable erythrocytes with longer circulation lifespans, if thrombosis-related complications do not significantly increase [188-190]. For those requiring immediate transfusion, the use of only recently donated blood products (for example: less than 7-days-old) and targeting a lower acceptable hemoglobin concentration goal, may maximize the clinical utility of each administered unit while minimizing immuno-activation [125, 126].

Additionally, despite critical care studies that suggest no difference between crystalloid and colloid solutions during general fluid resuscitation [191], the use of albumin and/or fresh frozen plasma (FFP) for postoperative volume replacement in MCS patients should be thoroughly examined. As both the etiology (trauma/sepsis versus surgery/device-placement) and goal (resuscitation versus euvolemia/device-preload) of intravenous fluid administration is vastly different, the use of colloid solutions for this patient group cannot be dismissed. The effects of plasma proteins including enhanced microcirculation through reduced RBC aggregation,

protection of RBCs from mechanical shear stresses, and intravascular fluid retention, may yield significant benefits to for patients with VADs.

APPENDIX A

RED BLOOD CELL MECHANICAL FRAGILITY TEST FOR CLINICAL RESEARCH APPLICATIONS

The work presented below has been published within Artificial Organs [93].

Red blood cell (RBC) susceptibility to mechanically induced hemolysis, or RBC mechanical fragility (MF), is an important parameter in the characterization of erythrocyte membrane health. The rocker bead test (RBT) and associated calculated mechanical fragility index (MFI) is a simple method for the assessment of RBC MF. Requiring a minimum of 15.5 mL of blood and necessitating adjustment of hematocrit (Ht) to a ‘standard’ value (40%), the current RBT is not suitable for use in most studies involving human subjects. To address these limitations, we propose a 6.5 mL reduced volume RBT and corresponding modified MFI (MMFI) that does not require prior Ht adjustment. This new method was assessed for **i**) correlation to the existing text, **ii**) to quantify the effect of Ht on MFI, and **iii**) validation by reexamining the protective effect of plasma proteins on RBC MF. The reduced volume RBT strongly correlated ($r = 0.941$) with the established large volume RBT at matched Hts, and an equation was developed to calculate MMFI: a numerical estimation ($R^2 = 0.923$) of MFI if performed with the reduced volume RBT at “standard” (40%) Ht. An inversely proportional

relationship was found between plasma protein concentration and RBC MF using the MMFI-reduced volume method, supporting previous literature findings. The new reduced volume RBT and modified MFI will allow for the measurement of RBC MF in clinical and preclinical studies involving humans or small animals.

A.1 INTRODUCTION

Red blood cell (RBC) mechanical fragility (MF) is a measure of erythrocyte susceptibility to mechanical stress. While a number of methods for the measurement of RBC MF have been proposed, a comparison of many existing methods has suggested that the rocker bead test (RBT) first described by *Kameneva et al* [96] is the most practical test for common use [83]. An important parameter in the characterization of erythrocyte membrane health, RBC MF tests have proven useful in assessing donor blood quality during *in vitro* hemolysis testing of blood-contacting medical devices, sublethal cell damage induced by cell salvage suction devices, and in characterizing RBC storage lesion [84, 88, 89].

The original RBT mentioned earlier requires a minimum of 15.5 mL of RBC suspension. This large volume requirement has limited the use of the RBT to large animals, healthy adults, or banked blood, precluding assessment from adult and pediatric patients, as well as small animals. However, preliminary investigations have indicated certain disease states are associated with higher RBC MF compared to healthy control groups [192-194]. Additionally, neonates have proven to have higher RBC MF than adults, potentially implicating a yet-to-be-investigated higher degree of sublethal cell trauma in pediatric patients from supraphysiological stresses like

those found during mechanical circulatory support or extracorporeal membrane oxygenation (ECMO) [85].

In addition to sample volume requirements, the existing RBT is hematocrit (Ht) dependent. Comparisons between RBC MFIs can only be made if the RBT was performed at equal Hts. Blood obtained directly from patients would have varied Ht values, and manual adjustment requires additional blood volume and time. Therefore, development of an easily employed method or algorithm to calculate a standardized MF value despite sample measurement at varied Hts is certainly justified.

A.2 MATERIALS AND METHODS

A.2.1 Experimental Design

Comparison of the traditional large volume RBT and our new, reduced volume RBT was accomplished by running these tests in parallel at the Ht values of 25, 30, 35, and 40% using matched bovine blood pools.

Human blood ($n = 4$) was used to characterize the effect of Ht on MFI and create a Ht-independent modified MF index (MMFI) for the reduced volume RBT. Each single-donor unit was assessed ($n = 6$) at four different Ht values (range 25–50%). Finally, validation of the reduced volume RBT's ability to ascertain differences in RBC fragility was achieved by the variation of total plasma protein, previously shown to significantly affect RBC MF [96], using human RBCs from a single blood pool.

A.2.2 Blood Preparation

All blood samples used in these studies were purchased from certified biological supply companies. Venipuncture-obtained, bovine whole blood anticoagulated in K2-EDTA was purchased (#7200807; Lampire Biological Laboratories, Pipersville, PA, USA) and used 2 days following draw date. Adult donor human whole blood anticoagulated in K2-EDTA was purchased (# HB1051K2; Valley Biomedical Products and Services, Inc., Winchester, VA, USA) and used within 4 days following withdrawal. Upon arrival, each unit was filtered (SQ40S blood transfusion filter; Pall Medical, Portsmouth, UK) to remove platelet microaggregates before storage at 0–4°C when not in use.

Experiments were performed using autologous donor pools. Ht variations were achieved by dilution with autologous plasma. Variation of total plasma protein was performed by dilution of plasma with phosphate-buffered saline. Upon resuspension at the desired parameters, Ht (SurePrep 75 mm heparinized self-sealing capillary tubes; BD Clay Adams, Sparks, MD, USA) and total hemoglobin (tHb) (OSM3 Hemoximeter; Radiometer, Copenhagen, Denmark) concentration were measured in every blood aliquot.

A.2.3 MF Measurement

The rocker bead experiments were set up and performed as described previously [81], differing only in tube preparation for the proposed method. Each traditional large volume RBT utilized five 7.0 mL silicone-coated, glass collection tubes (Red-Top Serum Vacutainer ref: 366431; Becton-Dickinson, Franklin Lakes, NJ, USA) filled with 3.0 mL of whole blood. Three experimental tubes contained five 1/800 diameter stainless steel ball bearings (BBs) each

(BNMX-2, Type 316 balls; Small Parts, Inc., Miami Lakes, FL, USA), and the remaining two tubes without BBs served as controls. In contrast, the modified reduced volume method consisted of three tubes (two experimental with BBs, one control) using 3.0 mL plastic collection tubes (No Additive Vacutainer ref: 366703; Becton-Dickinson) filled with 2.0 mL of whole blood and only three BBs per experimental tube.

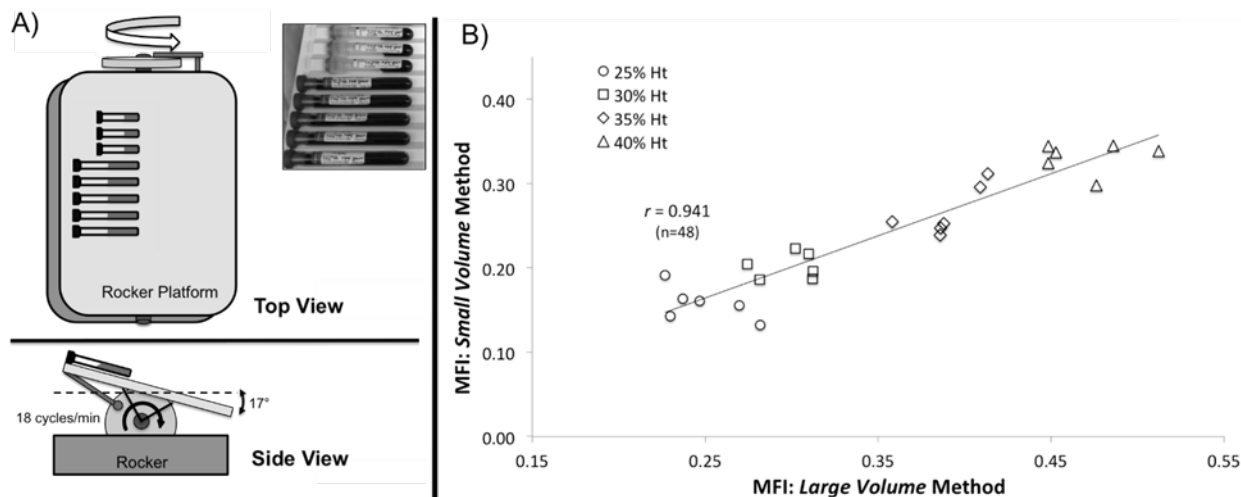


Figure 50. A) Schematic of reduced volume and large volume rocker bead tests running simultaneously and B) comparison of MFI values obtained from reduced volume and large volume tests run simultaneously at matched hematocrits between 25 and 40% using bovine blood (Pearson's correlation coefficient $r = 0.941$).

The 7.0 mL tubes were placed on a rocker (Type M79735 Platform Vari-Mix rocker; Barnstead Thermolyne Corp., Dubuque, IA, USA) with their tops touching the edge of the platform, and 3.0 mL tubes were placed with their bottoms aligned to the bottoms of the 7.0 mL tubes. Rocking was performed for 1 h at 18 cycles/min at a rocking angle $\pm 17^\circ$ from horizontal on a platform mixer (**Figure 50-A**). The tubes were centrifuged for 15 min at $2750 \times g$ (CR412; Jouan, Inc., Winchester, VA, USA) at which point the supernatant was transferred to 1.5 mL microcentrifuge tubes and spun at $20,800 \times g$ for 20 min (Eppendorf 5417R, Westbury, NY, USA). Free hemoglobin (fHb) in the final supernatant was measured via spectrophotometer

(Genesys 5; Spectronic Instruments, Inc., Columbus, OH, USA) using the Wintrobe method (absorbance at 540 nm) [24]. All of the above procedures were carried out at room temperature ($22 \pm 1^\circ\text{C}$).

The dimensionless MF index (MFI) value for each experiment was calculated as follows:

$$MFI = \frac{\overline{fHb}_{Experimental} - \overline{fHb}_{Control}}{\overline{tHb} * 1000 - \overline{fHb}_{Control}} * 100$$

where tHb is the total hemoglobin concentration of the blood sample in g/dL, and fHb is the average free hemoglobin concentration of the BB containing or control tubes in mg/dL.

A.2.4 Statistical Analysis

Descriptive statistics were expressed as mean \pm one standard deviation. Linear correlation (Pearson's correlation coefficient) was used to examine the relationship between the reduced volume and large volume methods, while multivariate linear regression (SPSS; IBM, Armonk, NY, USA) was used to establish the relationship of MFI with respect to Ht and create the reduced volume MMFI. One-way analysis of variance was applied to test MMFI significance between plasma protein concentrations, and a *P* value <0.05 was considered statistically significant. Post-hoc testing was conducted using the Tukey method.

A.3 RESULTS

A.3.1 Comparison of Rocker Bead Methods

While the new reduced volume RBT displayed lower MFI values relative to the older large volume method at each bovine blood matched Ht, a very strong linear relationship was observed between the two experimental protocols ($r = 0.941$) as shown in **Figure 50-B**.

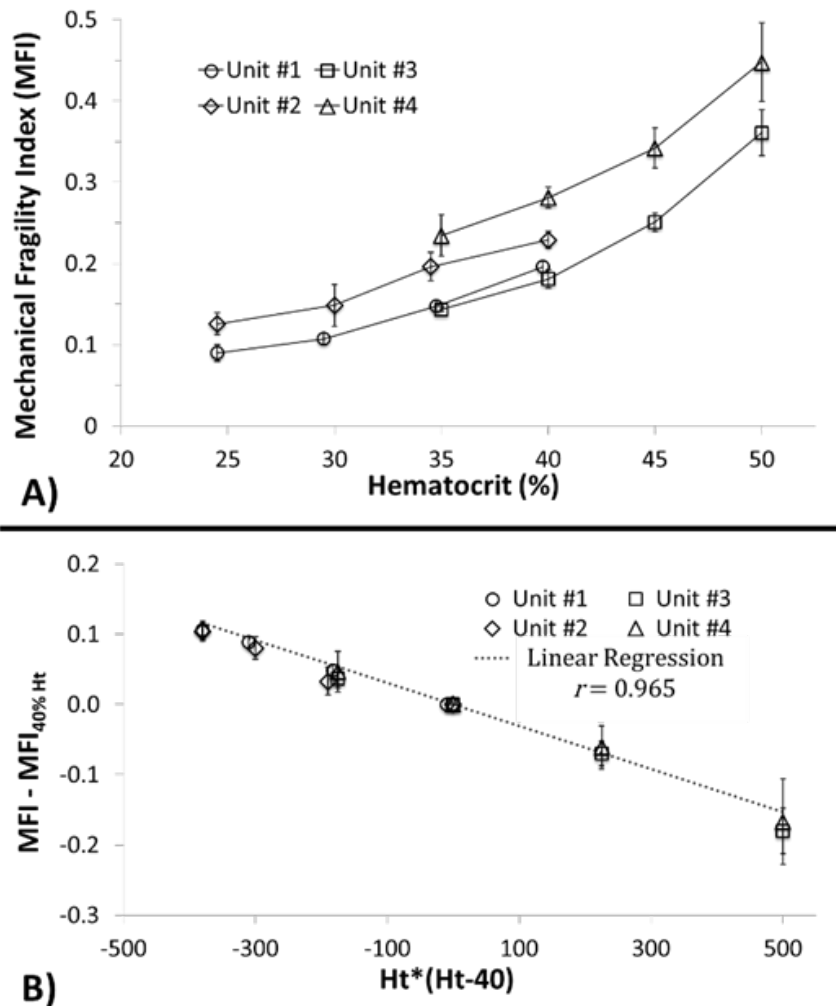


Figure 51. A) MFI values at hematocrit concentrations between 25 and 50% and B) the resultant regression analysis of the MFI residuals after linearization using the reduced volume RBT with human blood.

A.3.2 The Modified Mechanical Fragility Index (MMFI)

A strong nonlinear relationship was observed between sample Ht of the reduced volume RBT and the resultant MFI using human blood as shown in **Figure 51-A**. Linear regression analysis on the MFI residuals (difference in MFI from the paired MFI value at 40% Ht) as a function of Ht deviation multiplied by the test Ht yielded a highly correlated fit ($r = 0.965$) at a forced y-intercept of zero (**Figure 51-B**). The coefficient of determination predicting MFI from the experimental value at 40% Ht using the generated correction factor was $R^2 = 0.941$. Defining MMFI as the MFI if run at a standard Ht of 40%, the MMFI equation for the reduced volume RBT became:

$$MMFI = MFI - \frac{Ht(Ht - 40)}{3266}$$

where 3266 is the fitted correction constant derived from the slope of the linear regression analysis in **Figure 51-B**.

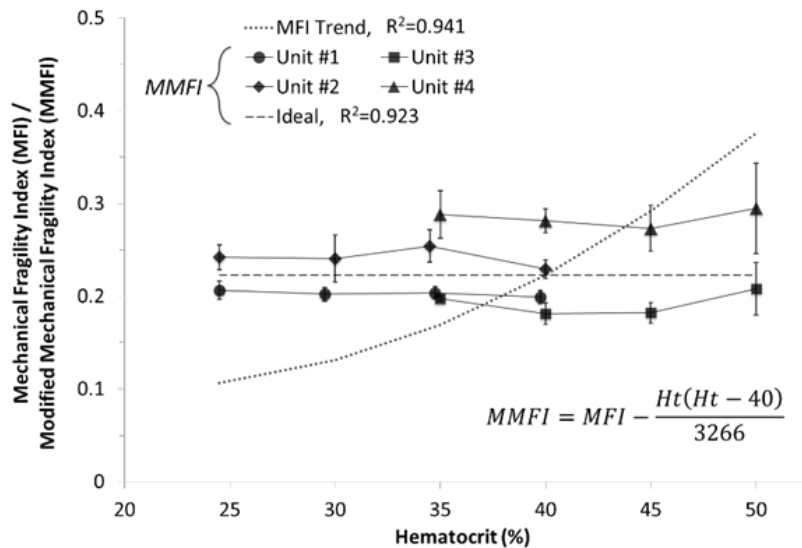


Figure 52. Comparison of the reduced volume MMFI to the MFI (mean \pm 1.0 SD) across four different human blood units at hematocrits between 25 and 50%.

The calculated MMFI for each experiment is shown in **Figure 52** corresponding well to the MFI measured at 40% Ht for each unit of human blood ($R^2 = 0.923$).

A.3.3 MMFI Reduced Volume Validation: Plasma Protein Protective Effect

There was a clear inverse linear relationship between total plasma protein concentration and RBC MF using the reduced volume RBT with human blood, with a statistically significant difference between 8.0 and 5.0 g/dL ($P < 0.01$) (**Figure 53**). There was a minor change in plasma viscosity associated with dilution, resulting in values of 1.74, 1.56, and 1.42 cP for the 8, 6.5, and 5.0 g/dL solutions, respectively.

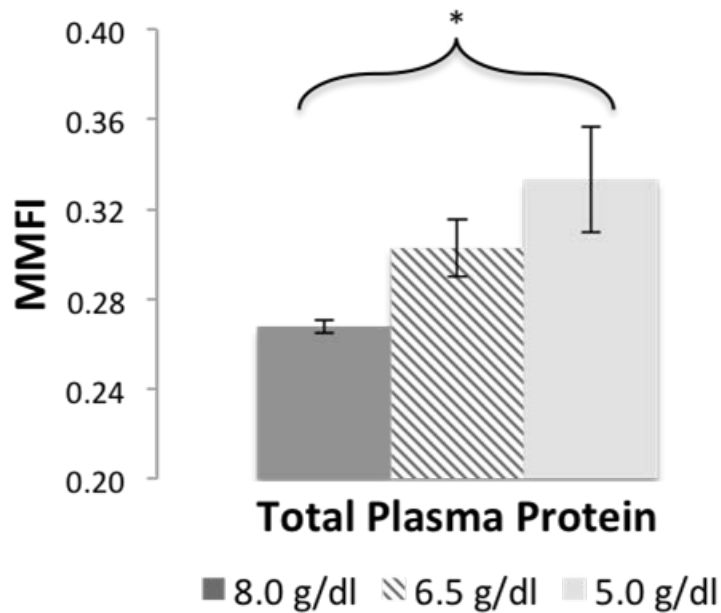


Figure 53. Effect of total plasma protein on red blood cell modified mechanical fragility index values as measured by the reduced volume RBT at 40% hematocrit using human blood. (* - $P < 0.01$).

A.4 DISCUSSION

The previously utilized large volume RBT of RBC MF, while an inexpensive, easily employable, and precise test, is limited in its scope of possible applications due to large blood sample volume requirements. For example, while it has been used in assessing blood quality during *in vitro* biocompatibility testing of blood pumps, researchers have been previously incapable of measuring the level of sublethal blood damage occurring in patients on mechanical circulatory support. Large sample volume requirement has also made it impossible to assess preoperative baseline RBC MF as a potential biomarker indicative of degree of hemolysis or anemia following left ventricular assist device (LVAD) implantation [195]. Should this prove a relevant clinical biomarker, the new test may predict patient outcomes prior to LVAD implantation.

As a function of MFI and a correction factor, MMFI remains dimensionless while retaining the familiar magnitude of scale. The same reasoning and principles applied with the selection of 40% Ht as the ‘standard’. While the Ht range examined (25–50%) represents typical clinical concentrations, MMFI values from reduced volume RBTs performed outside of this range may be less representative of RBC MF.

While previously published data investigated the effect of total plasma protein concentrations on RBC MF at 50 and 0% relative to baseline whole blood, we investigated concentrations of ~80 and ~60% relative to baseline whole blood [96]. A similar inversely proportional relationship was found in this study with a statistically significant difference in RBC MF at ~60% from baseline.

The new reduced volume RBT has some limitations. The large volume RBT has been previously shown to have excellent intralaboratory reproducibility but poor interlaboratory reproducibility [84]. While the phenomenon of interlaboratory reproducibility was not

investigated in our development of the reduced volume method, we hypothesize that it will be similar. There are a number of factors such as minor variations in rocker speed, rocker amplitude angle, and blood collection method that can influence results when performed in different laboratories. This does not decrease the efficacy or meaningfulness of our test because in the context of a single-center clinical or preclinical study, it is the relative differences in MMFI values between samples, not the absolute magnitude of the MMFI values, which is significant.

The use of K2-EDTA, a dry-form calcium chelator, for these studies was to minimize hemodilution and possible plasma protein alternations. Since anticoagulation may affect RBC MF through plasma protein dilution, activity, and other direct or indirect mechanisms of actions, one anticoagulant should be used for all samples in a given study.

This new test was created to be of use in single-center studies involving patients and/or small animal experiments. The possible applications other than the above-mentioned mechanical circulatory support patient studies are plentiful; examples include assessing mechanical RBC damage in patients supported by ECMO or dialysis, testing the effects of pharmaceutical treatments on blood diseases or blood bank stored donor RBC transfusion, and assessing the viability of modified RBCs acting as intravascular drug delivery vehicles [196].

A.5 CONCLUSION

We have created a reduced volume rocker bead test of red blood cell mechanical fragility, and associated modified mechanical fragility index, that is easily employable, inexpensive, and requires a relatively small volume of blood. This method can be utilized in clinical and preclinical research studies as well as a part of diagnostics and/or treatment of patients.

APPENDIX B

EFFECT OF INLET PRESSURE ON GAS EMBOLISM AND HEMOLYSIS IN CONTINUOUS-FLOW BLOOD PUMPS

The work described here was presented in part at the 2011 ASAIO 57th Annual Conference [197].

The current standard for reporting the results of an *in vitro* continuous-flow blood pump hemolysis test is to provide a description of the test circuit along with the numerical values of certain test parameters including motor speed, flow rate, hematocrit, time duration, and pressure drop across the pump. Noticeably absent from the reported parameters is the pressure at the pump inlet, which is surprising considering that previous studies have described the hemolytic effect of large vacuums when coupled to air exposure. Furthermore, many clinicians routinely encounter these negative pressures while running these pumps on patients. These preliminary experiments attempt to examine the effect of inlet pressure on hemolysis and gaseous emboli generation.

B.1 INTRODUCTION

There is increasing interest in high flow, low volume, biocompatible circulatory-assist devices leading to the development of small, high-speed rotary blood pumps for use in ECMO and as VADs. During clinical use, these pumps routinely encounter negative inlet pressures due to inadequate patient pre-load. Thus there is a need to quantify the effect of low preload on the *in vitro* hemolysis results of rotary blood pumps (RBPs).

B.1.1 Experiences with CPB

Previous cardiopulmonary bypass (CPB) studies have shown correlations between high vacuum pressures and hemolysis in reference to cardiotomy suction, in-adequate preload, or cannulae selection/placement [198-200]. While one study posited that extreme negative pressure does not cause hemolysis, this was supported in the absence of an air-blood interface and during pressure-driven, single pass experiments [201]. These assumptions are lost with the application of RBPs, as motor suspension and biocompatibility performance may be adversely effected by the presence of air.

B.1.2 Emboli Generation in Saline

Initial studies in saline indicated a strong relationship linking inlet pressure and motor speed to spontaneous emboli generation within a fully magnetically levitated, continuous-flow, centrifugal blood pump (**Table 4**). Using embolism detectors (>50 μm diameter threshold) at the inlet and outlet of a Thoratec® PediMAG® within a simple mock loop, taking the difference in

emboli count between detectors excludes any re-circulating emboli revealing only air generated by the pump itself.

Table 4. Emboli generation rate in saline with the Thoratec® PediMAG®.

Emboli/min ($>50 \mu\text{m}$)		Motor Speed (RPM)			
		2500	3000	2500	4000
Inlet Pressure (mmHg)	10	0	2		
	0	0	0	0	
	-10	0	0	7	
	-20		0	16	6
	-30		1	350	1150
	-40		542	3196	7231

Generation of gaseous emboli, whether from vacuum degasification or pump cavitation, pose a more serious risk when blood pumps are used as VADs due to the lack of an oxygenator to service as a ‘filter’. This preliminary study aims to examine the effect of inlet pressure on gas embolism and hemolysis in the Thoratec® PediMAG®.

B.2 METHODS

A ¼” flow loop circuit (**Figure 54**) was designed to evaluate hemolysis and gas embolism formation at 0.5 L/min (2300 rpm) and 1.5 L/min (2700 rpm) for four hours at three inlet pressures (0, -20, and -40 mmHg). The desired inlet pressures were reached by adjusting the inlet

and outlet throttle tubing clamps at the respective test flow rates, thereby maintaining the same pressure drops across the pump as well.

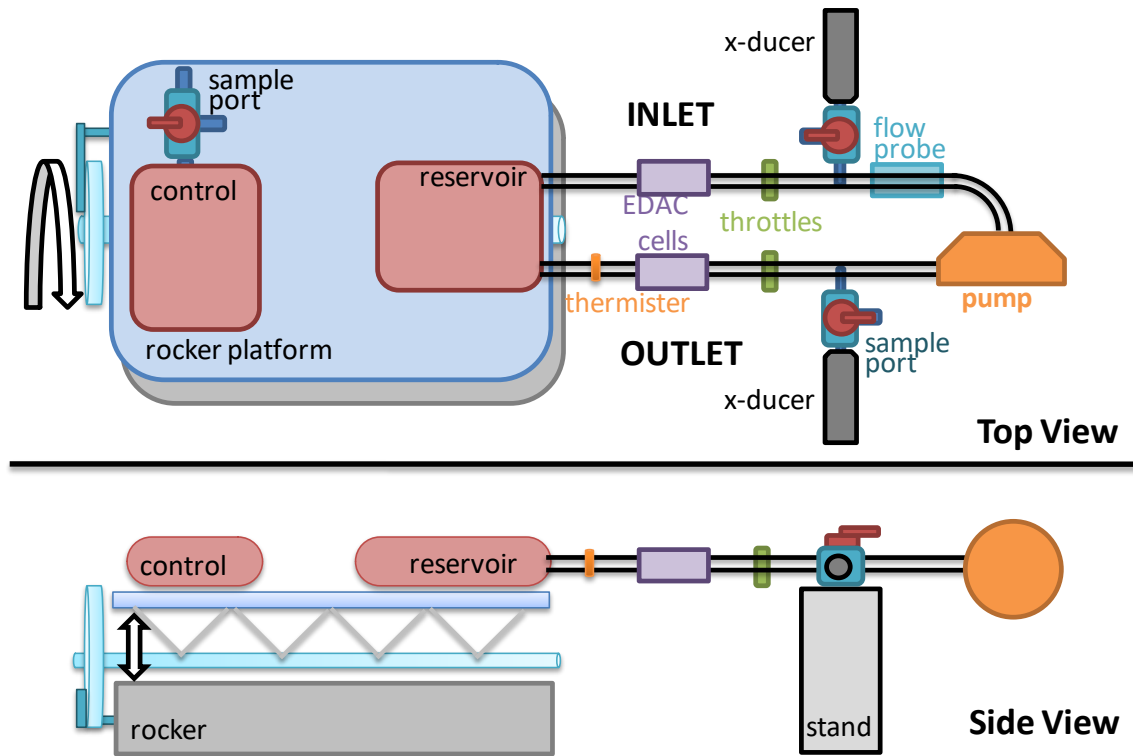


Figure 54. Schematic of the test loop for assessment of gas emboli and hemolysis.

A rocker platform was used to ensure adequate mixing within the reservoir bags due to the low flow rates. All blood contacting surfaces were passivated with 1% bovine serum albumin solution before emptying and priming. The flow loop and control bag was filled with 200 mL of fresh ovine blood, adjusted to a hematocrit of $30 \pm 2\%$, and completely de-aired before pump start. Samples (3 mL) were obtained every two hours for plasma free hemoglobin (plfHb) measurements and the Normalized Index of Hemolysis (NIH) calculated [143].

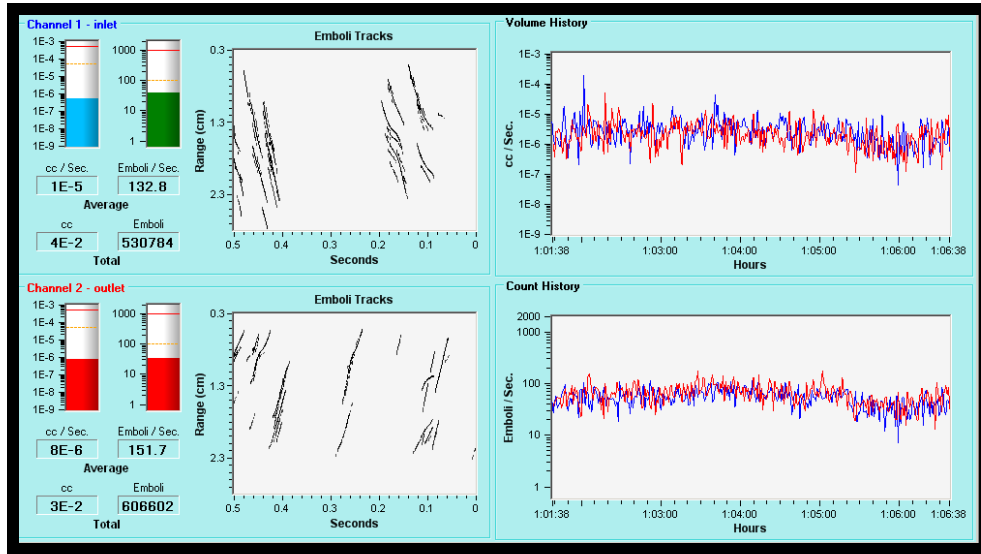


Figure 55. Display screen of the EDAC Quantifier system.

The Emboli Detection and Classification (EDAC) Quantifier (Luna Innovations®, Blacksburg, VA) was used to measure air emboli in real-time as shown in **Figure 55**. Two EDAC sensors cells (**Figure 56-Inset**), were placed (inlet and outlet of reservoir) in order to distinguish pump generated emboli from existing emboli circulating from the blood bag.

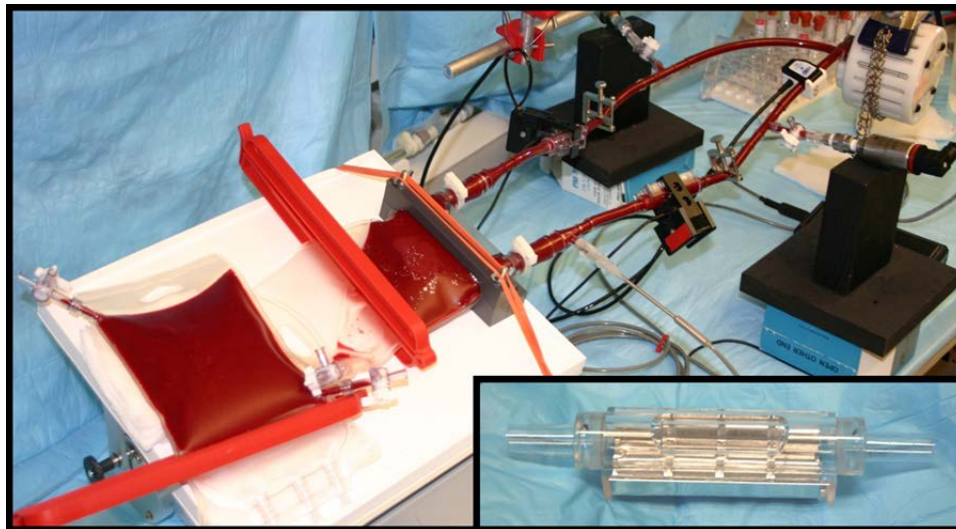


Figure 56. *In vitro* test setup with the EDAC cells (inset) used to measure the emboli within the flow loop.

B.3 RESULTS AND DISCUSSION

Hemolysis measurements suggest a threshold for increased NIH and inlet vacuum pressures at lower flow rates as shown in **Figure 57**. The larger NIH at the lower flow rate may be due to longer blood residence times within the pump, leaving the red blood cells exposed to high shear for longer periods.

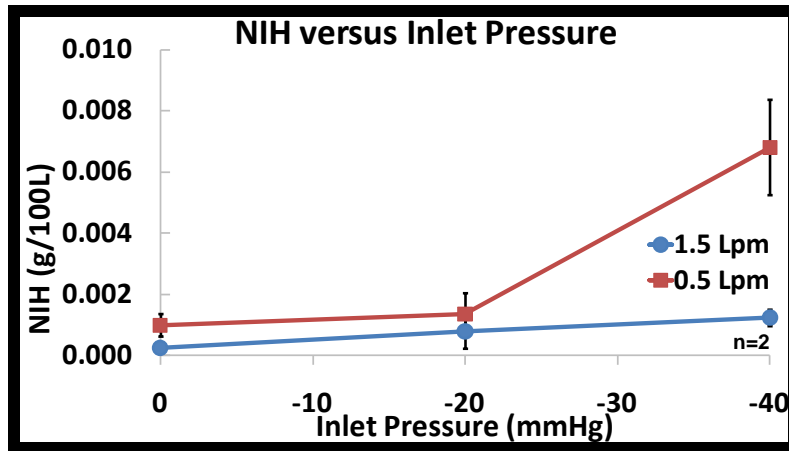


Figure 57. Plot of NIH \pm SDEV as a function of negative inlet pressure and flow rate.

Emboli generation per minute (**Figure 58**) reflects the same trend seen within the hemolysis data, showing a strong correlation between emboli generation and blood trauma.

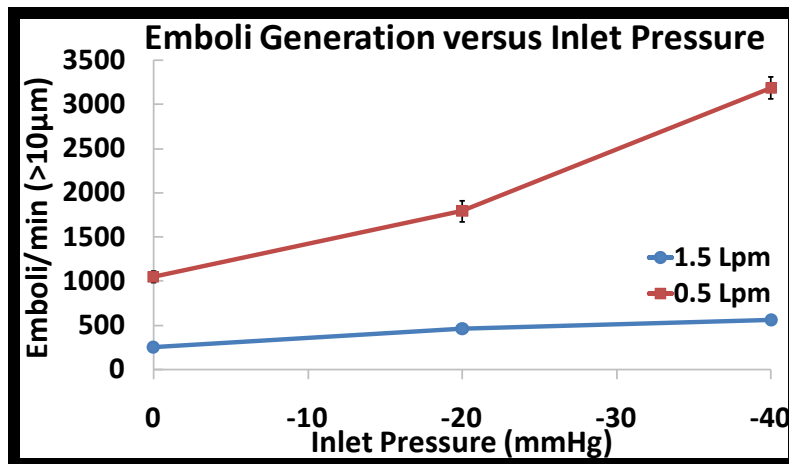


Figure 58. Plot of emboli generation rate \pm SDEV as a function of negative inlet pressure and flow rate.

While **Figure 59** shows similar overall total emboli count for 0.5 and 1.5 L/min, it is clear through the comparison of inlet and outlet counts that more air is actually generated at 0.5 L/min as opposed to simply recirculated within the loop.

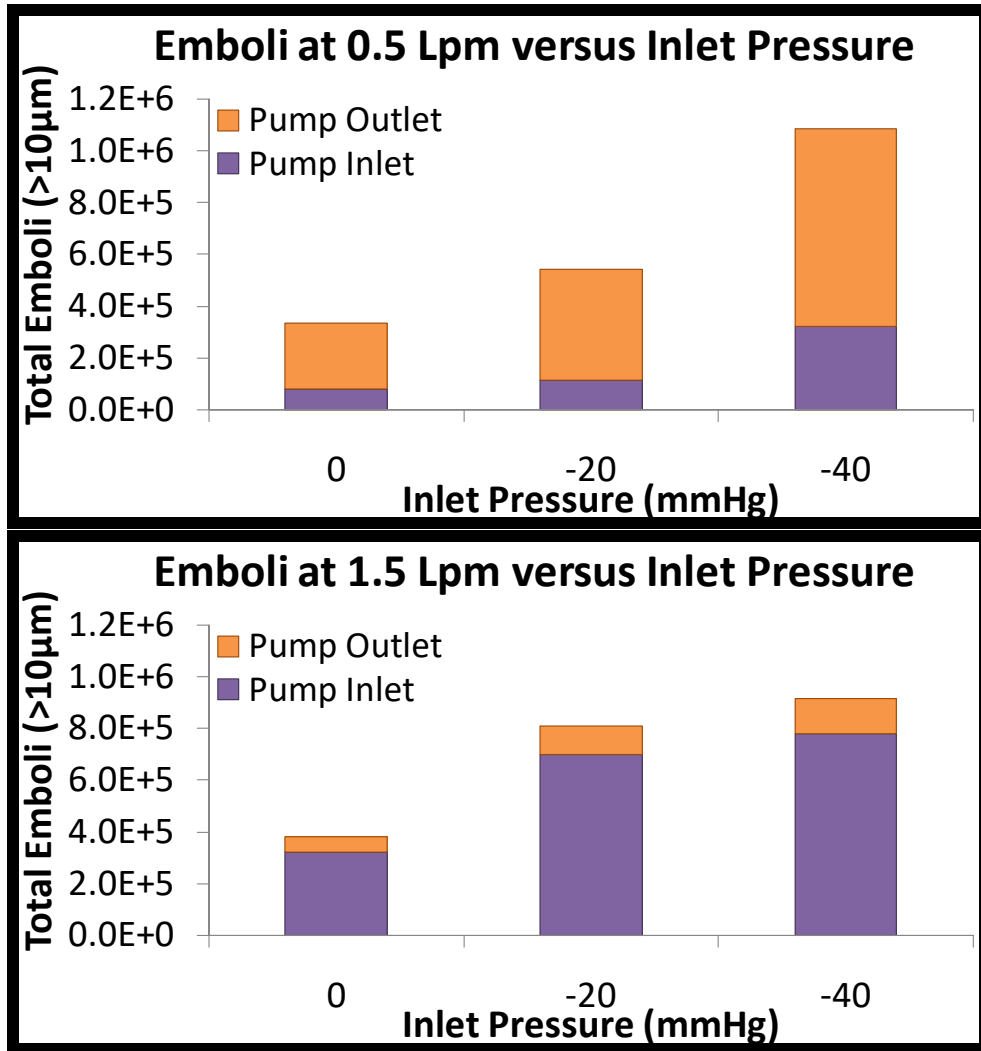


Figure 59. Total gaseous emboli entering and exiting the pump at each inlet pressure and flow rate.

Analysis of emboli size at the inlet and outlet EDAC cells (**Figure 60**) show greater counts of larger air emboli entering the pump while the exit has much higher counts of the bubbles at smaller diameters, indicating that there is bubble dispersion within the pump.

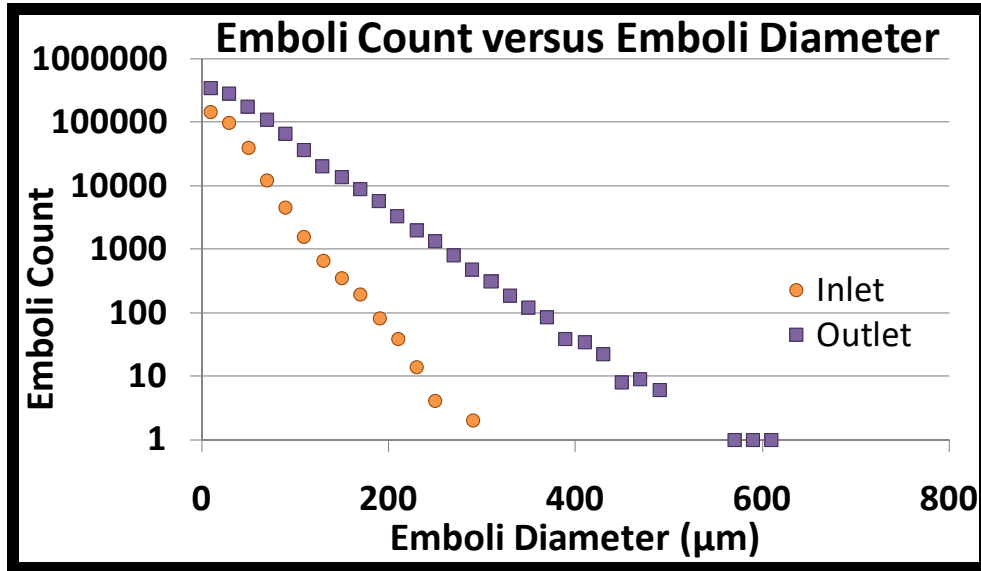


Figure 60. Histogram of total emboli segregated by size diameter for one 0.5 L/min study at -40 mmHg.

These preliminary studies indicate that ensuring adequate preload to minimize negative pump inlet pressures is important during *in vitro* hemolysis testing and clinical operation. Pump biocompatibility performance appears to be affected by the presence of air which may destabilize the motor suspension and/or contribute with shear stress to hemolysis. For future studies, if adequate mixing can be ensured, performing these tests vertically (reservoir above the pump) will minimize air emboli re-entering the pump; thereby reducing the noise of these tests.

APPENDIX C

SUMMARY RESULTS OF THE 4TH GENERATION PEDIAFLOW® DEVELOPMENT

Table 5. Summary of the 4th generation PediaFlow® prototypes (PF4.x) fabricated by the Consortium.

<i>Prototype</i>	<i>Extent of Testing</i>	<i>Modifications</i>	<i>Manufacturing Findings</i>
PF4.1	Non-operational	-	-
PF4.2	<i>In Vitro</i>	Epoxy-sealed feedthrough assembly and PCB board	Ground failure at feedthrough requiring external grounding precluding <i>in vivo</i> assessment
PF4.3	<i>In Vivo</i>	Improved percutaneous cable feedthrough attachment design	-
PF4.4	Non-operational	-	Noncompliant components
PF4.5	<i>In Vivo</i>	-	-
PF4.6	<i>In Vivo</i>	-	-
PF4.7	<i>In Vivo</i>	Revised stator housing to accommodate a Gelweave®-compatible outflow assembly connection	Epoxy infiltration into driveline during hermetic sealing leading to eventual fracture from fatigue
PF4.6.1*	<i>In Vivo</i>	1. Reduced-size driveline connector 2. Smoothing filter on motor current signal 3. Axial sensor temperature compensation circuitry	-
PF4.8*	<i>In Vivo</i>	(refurbished <i>PF4.7</i>) Copper-shielded percutaneous cable	-

**Used in the 60- and 14-day implants representing the current PF4 implantable design.*

A total of nine PF4.x prototypes were fabricated, with six builds remitted for in vivo implantation and biocompatibility testing. Aside from variations due to manufacturing tolerances, the pump topologies (i.e.: blood flow paths) are identical across the PF4 generation. Instead, each hand-built pump represents the incorporation of incremental improvements based on fabrication and/or implant findings of the previous prototype.

C.1 PF4 IMPLANTABLE DESIGN MODIFICATIONS

C.1.1 Inflow Cannula Prototypes

As summarized in **Table 6** below, a total of seven (n=7) different inflow cannula were evaluated for use with the PediaFlow®. Additional information about the initial designs leading to the “parabolic”-cannula (**3.2.1**) can be found in **3.1**.

Table 6. The inflow cannulae developed, utilized or under consideration for use with the PF4.

<i>Prototype</i>	<i>Iteration</i>	<i>Design Features</i>	<i>Findings</i>
Fenestrated	-	Modified 18-22 Fr commercial venous drainage Custom glue-fixed apical sewing ring Single-stage multi-port/caged-tip Malleable or right angle wire reinforced body	3.1.1
Conformal	1	Nitinol-reinforced silicone flange inlet Suture-less retention system (threaded nut) Deployment tool	3.1.2
Conformal	2	Increased flange diameter	3.1.2
Bevel	1.0	Nitinol, round-wire reinforced polyurethane Blunt-tip inlet opening Pre-attached, fixed-depth, rotating sewing ring	3.1.3
Bevel	1.1	Reduced pump connection flange diameter	3.1.3
Bevel	2	316 SS, flat-wire reinforcement Increased bend angle Graded strain relief at pump connector	3.1.3
Parabolic *	1	316 SS reinforced U-shaped inlet opening Removable, variable depth, tool-less sewing ring	5.2

**Used in the 60- and 14-day implants representing the current PF4 implantable design.*

C.1.2 Outflow Grafts

As described in **Table 7**, three outflow assembly iterations were implanted in conjunction with the PF4 *in vivo* studies. While previous generation PediaFlow® studies utilized polyester-based outflow grafts (including the 72-day *PF3-S01* implant), concerns about commercial availability and patency led to the selection of an ePTFE based graft for the first PF4 implants.

Table 7. The outflow graft assemblies used during the *in vivo* assessments of the PF4.

<i>Prototype</i>	<i>Outflow Graft</i>		<i>Modifications / External Strain Relief</i>
	<i>OD (mm)</i>	<i>Material</i>	
Bard® ePTFE	5.0	thin-wall ePTFE	-
SEAL-PTFE™	6.0	dual-layer, extraluminally gelatin-sealed ePTFE	Reduced pump connector flange dia. 8mm MAXIFLO™ ePTFE Wrap
Gelweave™ *	6.0	gelatin-impregnated polyester	8mm MAXIFLO™ ePTFE Wrap

**Used in the 60- and 14-day implants representing the current PF4 implantable design.*

Bard® ePTFE (5 mm Flex Thinwall Small Beading) is a product of Bard® Peripheral Vascular (Tempe, AZ, USA). SEAL-PTFE™ (standard-wall, external spiral support), MAXIFLO™ (standard-wall, external solid-PTFE spiral support), & Gelweave™ are products of Vascutek® Ltd (Renfrewshire, Scotland, UK).

The initial PF4.x ovine studies using a 5.0 mm Bard® ePTFE graft suffered from excessive serous chest drainage and significant plasma loss requiring premature elective termination of the studies (**C.2.1**). A qualitative analysis of graft permeability on the explanted ePTFE outflow graft from *PF4-S01* was performed impromptu following necropsy. Using a roller pump to simulate the *in vivo* flow conditions ($Q = 1.2$ L/min, $\Delta P = 100$ mmHg), ovine blood (30% Ht) with Coomassie blue was circulated within a mock loop through the outflow graft submerged in a saline bath (**Figure 61**).

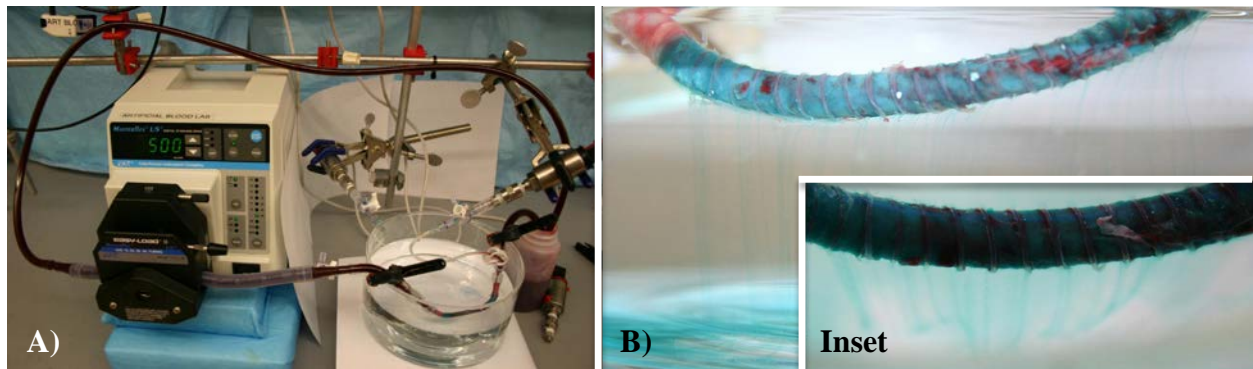


Figure 61. Qualitative analysis of outflow graft permeability **A)** experimental loop setup, and **B)** the explanted ePTFE graft with streak lines perpendicular to the graft surface highlighting “graft weep” (**Inset**).

Substantial leakage was observed (**Figure 61-Inset**) suggesting that the large fluid loss experienced during the implant study was due to graft permeability. Typically used for anatomical repair or applications under physiological hemodynamics, the supra-physiological pressures from pediatric RBPs may adversely affect the material properties and permeability of the notably hydrophobic ePTFE grafts [162]. With similar findings in a subsequent implant (*PF4-S02*), there is a strong evidence suggesting ePTFE vascular grafts are susceptible to both aqueous and protein permeability, or “plasma weep”.

Despite switching to a dual-layer, gelatin-coated exterior ePTFE graft for PF4 implants (*PF4-S04*, *PF4-S05*), questions still remained regarding biocompatibility with continued bleeding and decreased plasma protein concentrations, and findings including intraluminal and extraluminal outflow graft thrombus at necropsy (*not shown*). After evaluating two different ePTFE styles, continuing issues with excessive fluid and plasma protein loss (i.e.: “graft weep”), led to the decision to return to the Gelweave™ grafts previously used successfully.

C.1.3 Pump Connectors

Introduced with the 4th generation PediaFlow® prototypes was a compact, tool-less, ‘quick-connect’ coupling used with both the inflow cannula and outflow graft assembly. Consisting of a nitinol-wire retaining clasp on the pump mating face and a flanged inlet/outlet adapter, attachment or removal of the cannula/graft is achieved by depressing the loop to concentrically deform the two guidewires that hold the radial flange in place (**Figure 62-A**). After initial wet-to-wet connections during surgical implantation were less than successful (**Figure 62-B**), a reduced flange diameter adapter was used for the PF4-S04 and subsequent implants that eliminated difficulties with non-seated pump connections (**Figure 62-C**).

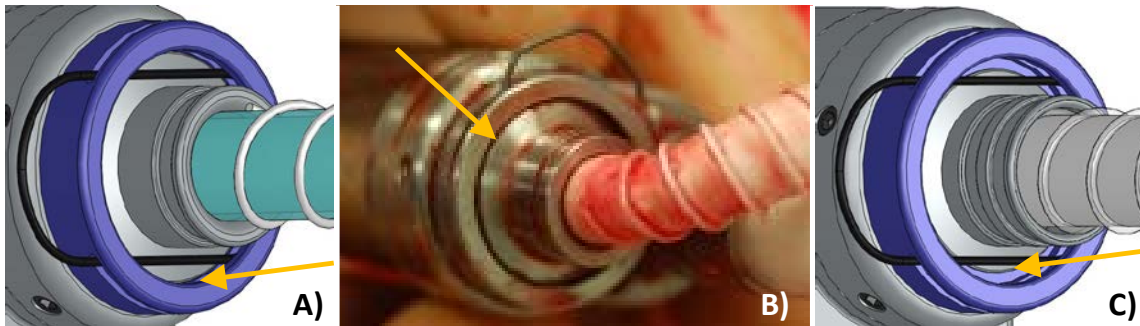


Figure 62. The PF4 ‘quick-connect’ attachment mechanism. **A)** The initial full-flange design was difficult to attach and **B)** prone to misalignment in vivo. **C)** The revised design with a smaller flange size to ease insertion past the guidewires.

C.1.4 Driveline and Controller Upgrades

Pending finalization of a clinical controller, the initial PF4.x prototypes in the interim utilized surplus Levacor® percutaneous cable and corresponding external driveline extension connector for connection to the preclinical controllers (**Figure 63-A**). After controller

development was halted, an analysis was undertaken to address the oversized threaded nut connector that was difficult to tunnel and unacceptable for clinical use with an excessive size difference between the outer diameter (OD) of the connector and cable. A more traditional push-pull, “Lemo”-type, connector was introduced with PF4.6.1 with a smaller OD and a watertight tunneling cap (**Figure 63-B**). Furthermore, concerns about signal noise and fatigue resistance due to the stainless steel braided shield of the existing driveline led to the selection of a copper-braid shielded percutaneous cable in PF4.8 and future pumps.

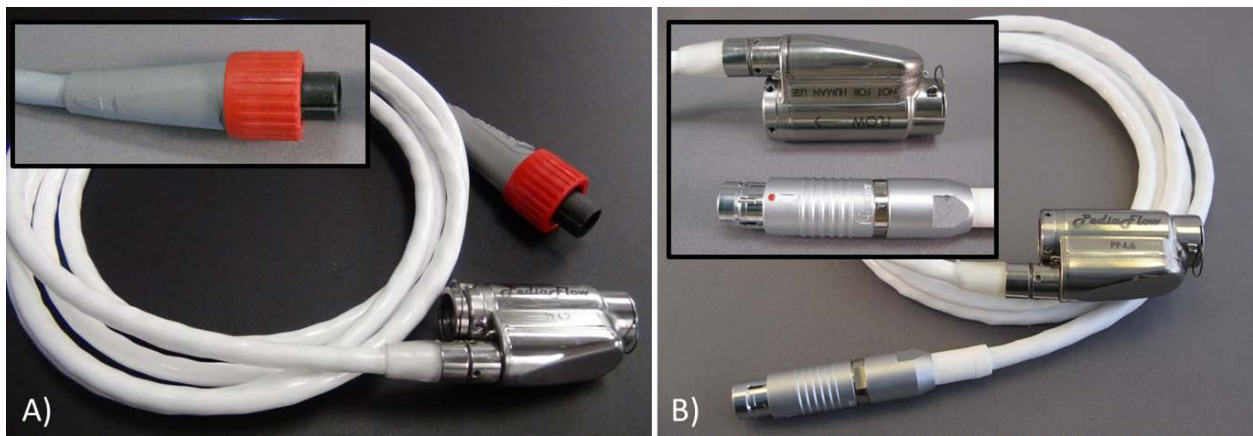


Figure 63. A) The original PF4.x threaded nut (A) driveline connector and the new push-pull connector (B) used in PF4.6.1 and subsequent prototypes.

Two notable hardware upgrades on the preclinical controllers introduced with PF4.6.1 were the axial sensor temperature correction circuitry to minimize rotor position signal drift post-implantation and a new alarm filter board for accurate output readings of pump motor current. These upgrades were relevant in the development of the PediaFlow® flow estimator and are detailed in **4.3.3**.

C.2 *IN VIVO* OVINE STUDIES & IMPLANTS

C.2.1 PF4.x Implants

A total of eleven juvenile sheep were implanted with the PF4.x prototypes to 1) evaluate the pump series from a physiological and biocompatibility standpoint, 2) the PediaFlow-specific inflow and outflow cannulae under development, and 3) the ease of surgical implantation and use of the pediatric LVAD system. A summary of these experimental studies and findings are shown in **Table 8**.

Table 8. Summary of the *in vivo* PF4-implanted juvenile ovine experiments.

<i>Implant #</i> (IACUC #)	<i>Weight</i> (kg)	<i>Pump</i>	<i>Inflow Cannula:</i> <i>Outflow Assembly:</i>	<i>Time</i> (days)	<i>Avg. Q</i> (L/min)	<i>Pertinent Findings</i>
PF4-S01 (S017-11)	28.0	PF4.3	I: 18Fr Fen. DLP® O: Bard® ePTFE	4/14	1.2	1. Serosanguinous fluid collection 2. Constricted outflow anastomosis
PF4-S02 (S026-11)	27.9	PF4.3	I: 22Fr Fen. Baxter® O: Bard® ePTFE	15/28	0.9	1. Detached pump inlet connection 2. Fibrous deposition surrounding outflow graft along entire length 3. Graft kink at pump attachment
PF4-S03 (S027-11)	23.0	PF4.5	I: Bevel 1.0 O: Bard® ePTFE	< 1	N/A	1. Respiratory failure peri-operatively following chest closure 2. Non-seated outflow connector
PF4-S04 (S034-11)	24.5	PF4.5	I: Bevel 1.1 O: SEAL-PTFE™	4/28	1.5	1. Respiratory failure secondary to thoracic blood collection 2. Outflow graft thrombus
PF4-S05 (S033-11)	28.0	PF4.6	I: Bevel 1.1 O: SEAL-PTFE™	4/28	1.0	1. Cardiac compression secondary to large thoracic hematoma 2. Tissue entrapped on cannula tip 3. Thrombus at base of LV
PF4-S06 (S009-12)	22.3	PF4.7	I: Bevel 1.1 O: Gelweave™	28/28	1.3	1. Inflow cannula kink
PF4-S07 (S018-12)	27.3	PF4.7	I: Bevel 1.1 O: Gelweave™	12/28	1.5	1. Rotor position sensor failure secondary to driveline fracture 2. Inflow cannula kink
PF4-S08 (S044-12)	28.2	PF4.6.1	I: Bevel 2.0 O: Gelweave™	9/28	2.0	1. Tamponade secondary to infectious pericarditis 2. Large thoracic hematoma
PF4-S09 (S001-13)	19.0	PF4.8	I: Bevel 2.0 O: Gelweave™	15/30	1.0	1. Cardiovascular collapse 2. Thoracic hematoma 3. Inflow cannula kink
PF4-S10 * (S011-13)	28.7	PF4.6.1	I: Parabolic O: Gelweave™	60/60	1.6	1. Unremarkable
PF4-S11 * (S012-13)	28.7	PF4.8	I: Parabolic O: Gelweave™	14/28	1.4	1. Unable to restart after rotor delevitation due to wear

* Current PF4 implantable design.

Despite the repeated challenges with the implantable peripherals *in vivo*, hemocompatibility as measured by plasma-free hemoglobin remained below 20 mg/dL for 7 of the 9 preliminary implants (**Figure 64**).

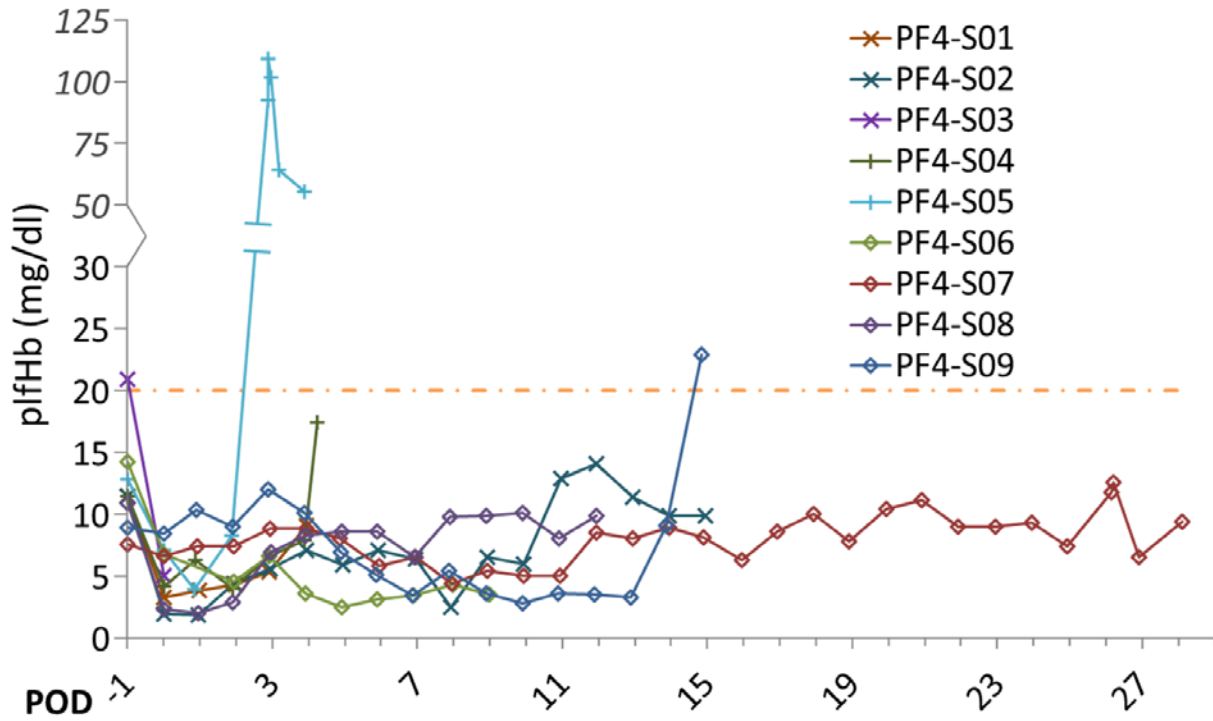


Figure 64. Plasma-free hemoglobin values for the initial *in vivo* PF4 implants.

Table 9. Additional blood parameters of the 3rd and 4th generation PediaFlow® and sham *in vivo* animal studies presented in 5.2. All were within reference values.

	PF3-S01 (72 days)	PF4-S10 (14 days)	PF4-S11 (60 days)	Sham Implants (n = 3, mean)	Reference Range
Weight (kg)	(24)	(30)	(28.7)	(43.3 ± 12.7)	
WBC (x 10 ³ /mm ³)	7.3 ± 1.2 (7.2)	8.6 ± 2.8 (9.5)	13.4 ± 3.4 (12.8)	5.0 ± 0.5 (5.6)	4-12
RBC (x 10 ⁶ /mm ³)	7.6 ± 0.5 (10.3)	8.2 ± 0.7 (13.1)	10.0 ± 0.7 (13.4)	8.5 ± 0.7 (9.9)	9-15
Hgb (g/dl)	8 ± 0.9 (9.9)	7.7 ± 0.6 (12.3)	10.7 ± 0.7 (14.2)	9.6 ± 1.0 (10.0)	9-15
HCT (%)	23.3 ± 2.7 (26.5)	24.1 ± 1.3 (37.6)	31.9 ± 1.9 (41.5)	26.6 ± 2.2 (31.9)	27-45
Platelets (x10 ³ /mm ³)	626 ± 248 (2000)	855 ± 477 (634)	605 ± 306 (518)	755 ± 571 (1406)	250-750
MCV (µm ³)	29.7 ± 1.8 (26)	29.7 ± 1.5 (29)	31.9 ± 1.0 (31)	31.4 ± 2.3 (31)	28-40
MCH (pg)	10.3 ± 0.6 (9.6)	9.4 ± 0.3 (9.4)	10.7 ± 0.3 (10.7)	11.4 ± 0.3 (10.2)	8-12
MCHC (%)	34.9 ± 1.2 (37.4)	31.8 ± 1.3 (32.7)	33.7 ± 0.9 (34.4)	35.8 ± 4.6 (35.2)	31-34
Neutrophils (x10 ³ /mm ³)	3 ± 1.3 (1.7)	3.8 ± 1.7 (3.2)	3.7 ± 2.4 (4.3)	2.2 ± 0.5 (1.9)	0.7-6.0
Lymphocytes (x10 ³ /mm ³)	3.7 ± 1.5 (4.6)	4.5 ± 2.1 (6.2)	9.2 ± 2.4 (8.2)	2.4 ± 0.5 (3.2)	2-9
PT (s)	22.1 ± 6.2 (26.6)	16.5 ± 7.3 (15.2)	16.9 ± 2.2 (16.2)	17.1 ± 3.4 (20.0)	N/A
INR	2.2 ± 3.5 (2.3)	N/A	N/A	N/A	N/A
PTT (s)	61.2 ± 22.7 (29.7)	43.7 ± 8.2 (44.5)	49.4 ± 12.8 (33.9)	31.1 ± 7.7 (38.2)	N/A
BUN (mg/dl)	21 ± 15.3 (16)	16 ± 5.4 (12)	11.2 ± 2.7 (13)	14.3 ± 1.9 (16)	10.3-26
Glucose (mg/dl)	91.9 ± 15.1 (88)	96.5 ± 32.1 (74)	77.9 ± 7.1 (86.5)	75.2 ± 4.3 (77.3)	44-81.2
Creatinine (mg/dl)	1.4 ± 1.5 (0.8)	0.9 ± 0.3 (0.7)	0.6 ± 0.1 (0.5)	1.3 ± 1.1 (0.6)	0.9-2.0
Ca (mg/dl)	10 ± 0.9 (10.5)	8.8 ± 1.1 (10.8)	10.1 ± 0.9 (10.9)	9.9 ± 0.3 (10.2)	9.3-11.7
Mg (mEQ/L)	1.1 ± 0.2 (1.6)	1.4 ± 0.3 (1.5)	1.6 ± 0.2 (1.8)	1.6 ± 0.0 (1.6)	2.0-2.7
Cl (mmol/L)	111 ± 4.7 (105)	109 ± 5.5 (107)	109 ± 3.3 (110)	109 ± 2.7 (108)	100.8-113.0
K (mmol/L)	6.1 ± 1.6 (4.4)	4.3 ± 0.7 (5.2)	5.2 ± 0.6 (4.7)	5.5 ± 0.8 (4.3)	4.3-6.3
Na (mmol/L)	143 ± 4 (144)	144 ± 3.3 (144)	145 ± 3.5 (150)	144 ± 0.5 (148)	141.6-159.6
SGPT(ALT) (IU/L)	11 ± 9 (13)	12.3 ± 10.5 (9)	10.4 ± 8.6 (10.5)	21.0 ± 17.6 (27.8)	14.8-43.8
SGOT(AST) (IU/L)	76 ± 46 (71)	212 ± 127 (82)	99 ± 67 (78)	71 ± 30 (70)	49.0-123.0
Albumin (g/dl)	2.7 ± 0.6 (3)	2.2 ± 0.3 (3.2)	2.8 ± 0.5 (3.4)	2.9 ± 0.1 (2.9)	2.4-3.0
Tot. Bilirubin (mg/dl)	0.1 ± 0 (0.2)	0.1 ± 0.1 (0.1)	0.6 ± 1.6 (0.1)	0.3 ± 0.2 (0.2)	0.1-0.5
GGT (IU/L)	44 ± 13 (57)	36.4 ± 6.0 (54)	36 ± 3.6 (52)	67 ± 25 (73)	10-118
LDH (IU/L)	437 ± 146 (325)	713 ± 355 (383)	427 ± 115 (439)	377 ± 8 (365)	238-560
Phos (mg/dl)	8.1 ± 1 (7.5)	5.1 ± 2.0 (6.2)	7.8 ± 1.3 (6.4)	7.2 ± 1.1 (6.4)	4.0-7.3
Cholesterol (mg/dl)	71.1 ± 26 (40)	47.8 ± 26.2 (56)	48.9 ± 13.8 (33.5)	71.7 ± 19.3 (43)	44.1-90.1
ALP (IU/L)	82.7 ± 23.6 (139)	100.8 ± 26.2 (144)	92.8 ± 17.7 (195.5)	112.3 ± 47.1 (230)	26.9-156.1
CPK (IU/L)	500 ± 1181 (111)	642 ± 805 (145)	613 ± 1678 (128)	270.8 ± 147.4 (300)	47-4212
Tot. Protein (g/dl)	5.2 ± 0.4 (5.7)	4.0 ± 0.5 (5.5)	5.1 ± 0.7 (5.7)	5.3 ± 0.2 (5.6)	5.9-7.8

Data presented as mean ± SD (pre-operative mean).

C.2.2 Surgical Shams (Controls)

Three “sham” implants were performed for an intended 28-days duration for the purpose of obtaining “control” biocompatibility data for the PediaFlow® implantations. These “sham”

surgical implants mimic an actual PediaFlow® implant except for device implantation and allow us to account for surgical effects and post-operative recovery on rheology, platelet activation and other biocompatibility indices of interest. As pre-operative jugular venipuncture samples are prone to artifact from needle sticking an awake animal [159], a jugular venous catheter was placed under general anesthesia a week before sham surgery for collection of baseline biocompatibility parameters (ie: platelet activation and plasma free hemoglobin).

For the actual “sham” surgery, following intubation and induction of anesthesia, the existing venous catheter in the left jugular vein was replaced and an arterial catheter was inserted in the left carotid artery. The thorax was entered via a left, fourth interspace thoracotomy and the left ventricular apex and descending aorta were exposed. The animal was anticoagulated with heparin to maintain the whole blood ACT at 1.5-2.0 times baseline. A lubricated sewing ring was fixed on the LV apex and a stab incision was made in the LV apex, which was then sutured closed. A 3 cm length of 6 mm diameter Gelweave™ (Vascutek® Ltd, Renfrewshire, Scotland, UK) graft was connected in an end-to-side fashion to the descending thoracic aorta to duplicate the pump outflow graft and anastomosis site. The graft was then “tied off” to prevent graft material being in contact with the blood.

The “sham” surgical procedures proceeded without any major complications, the animals recovered from anesthesia and were returned to the ICU, where they were monitored for the duration of the study. Recovery and follow-up was uneventful with hemodynamic and respiratory parameters remaining within normal limits. During follow-up periods, the animals were cared for exactly as the 72 day PF3 implanted animal had been. After meeting the intended 28-day study period, the three sham experiments were electively ended for gross necropsy examination per to surgeon availability.

Table 10. Summary of the surgical sham (control) animal studies.

<u>Study Animal</u> <u>(IACUC #)</u>	<u>Weight</u> <u>(kg)</u>	<u>Length (days)</u> <u>Actual/Intended</u>	<u>Findings</u>
Sham-S01 (S002-09)	45	39/28	1. Two minor (<2 mm dia), surface infarcts on left kidney 2. Two minor (<2 mm dia), surface infarcts on right kidneys
Sham-S02 (S003-09)	55	32/28	1. Single minor (<2 mm dia), surface infarct on right kidney
Sham-S03 (S017-09)	30	28/28	1. Unremarkable

C.2.3 PF3-01 72-day Implant [134]

The 3rd generation PediaFlow prototype (PF3) was implanted in a healthy lamb for 72 days in accordance with the Institutional Animal Care and Use Committee guidelines at the University of Pittsburgh. The pump was introduced into the circulation as a left ventricular assist device, interposed between the left ventricle and descending thoracic aorta. Surgical access was gained through a left thoracotomy, followed by heparinization for a target ACT >300s. A modified wire-reinforced polyurethane cannula (18Fr DLP®, Medtronic®, Minneapolis, MN, USA) was inserted into the apex of the left ventricle through a stab incision and secured with a sewing ring fashioned from thick surgical felt (PTFE, C.R. Bard®, Murray Hill, NJ, USA). The outflow from the PF3 was 6 mm diameter polyester vascular graft (Vascutek® Ltd, Renfrewshire, Scotland, UK) anastomosed to the descending thoracic aorta using a partial occlusion clamp. The pump was operated at a fixed speed of 14.5 kRPM. The flow rate was measured via an ultrasonic transit-time flow probe (Transonic® Inc., Ithaca, NY, USA) attached to the outflow graft. Throughout the study, pump flow, power consumption, and carotid blood pressure were

recorded. Hemorheology and serum chemistry values were collected daily to assess the biological impact of the pump on blood damage and organ function.

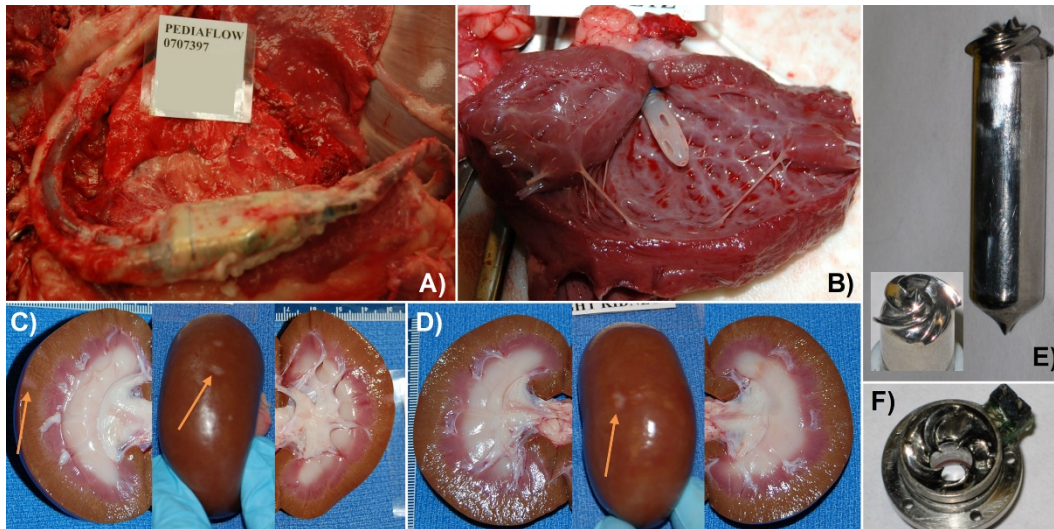


Figure 65. Necropsy images of the PF3-S01 (72-day) implant. A) pump placement *in situ*, **B)** the modified 18Fr fenestrated inflow cannula (Medtronic® DLP, Minneapolis, MN, USA) free of thrombus within the LV, **C)** left kidney with a minor and well-healed cortical infarction, **D)** right kidney with a minor surface infarction that was not visible upon sagittal dissection, **E)** the pump rotor and **F)** stator free of deposition.

Gross necropsy after the 72-day implant duration was unremarkable aside from a well-healed, minor cortical infarction on the left kidney, most likely at the time of initial surgery (**Figure 65-C**).

APPENDIX D

PROGRAMMING CODE

D.1 MATLAB SCRIPTS

D.1.1 Parsing Individual DSS Log File

```
% script to read data from LabVIEW generated .txt files
% specifically to examine individual files
% 07-16-13 SEO

nchan=9;
SR=400;
snip=5;

[fname,pname]=uigetfile('E:\PediaFlow\*.txt');
d = dir(pname);

disp(['Processing file ' [pname fname]]);
fid=fopen([pname fname],'r');

% mess=textscan(fid, '%s %s %f32 %f32 %f32 %f32 %f32 %f32 %f32 %f32 %f32');
% data=[mess{3},mess{4},mess{5},mess{6},mess{7},mess{8},mess{9},mess{10},mess{11}];
mess=textscan(fid,'%{M/d/yyyy}D %{HH:mm:ss.SSSSS}D %f32 %f32 %f32 %f32 %f32
%f32 %f32 %f32 %f32');
data=[mess{3},mess{4},mess{5},mess{6},mess{7},mess{8},mess{9},mess{10},mess{11}];

data=double(data);

%time = linspace(0,60,length(data(:,1)));
```

```

%time = linspace(0,length(data(:,1))/SR,length(data(:,1)));
mess{1}.Format='MM-dd-yyyy HH:mm:ss.SSS';
mess{2}.Format='MM-dd-yyyy HH:mm:ss.SSS';

time = mess{1}+timeofday(mess{2});

% LPF of data
[b_five,a_five]=butter(1,5*2*(1/SR));
% [b_half,a_half]=butter(1,0.5*2*(1/SR));
[b_tenth,a_tenth]=butter(1,0.1*2*(1/SR));

% 10Hz LPF coeffs
[b_ten,a_ten]=butter(1,10*2*(1/SR));

for n=1:nchan
%   data_tenth(:,n)=filtfilt(b_tenth,a_tenth,data(:,n));
%   data_five(:,n)=filtfilt(b_five,a_five,data(:,n));
   data_ten(:,n)=filtfilt(b_ten,a_ten,data(:,n));

   data_snip(:,n)=data(1:400*snip,n);

   data_ten_snip(:,n)=data_ten(1:400*snip,n);
%
%   [~,locs]=findpeaks(data_five(:,n)-data_tenth(:,n));
%   data_peak(:,n)=filtfilt(b_tenth,a_tenth,interp1(time(locs),data(locs,n),time,'spline'));
%
%   [~,locs]=findpeaks(-(data_five(:,n)-data_tenth(:,n)));
%   data_trough(:,n)=filtfilt(b_tenth,a_tenth,interp1(time(locs),data(locs,n),time,'spline'));
%
end

time_snip=time(1:400*snip);

% chan=["AP","CVP","RP","MS","LC","MC","AF","EF"];

% AP=data(:,1);
% RP=data(:,3);
% MS=data(:,4);
% LC=data(:,5);
% MC=data(:,6);
% AF=data(:,7);
% EF=data(:,8);
% EF_adj=0.8*(460502097.944 + 45678592*(MS.^2) + 427128023.204.*MC + -
8268351850*abs(RP+0.9))./(173167168.*MS);
%

```

```

createfigure(time,data(:,1),data(:,3),data(:,4),data(:,5),data(:,6),data(:,7));
createfigure(time,data_ten(:,1),data_ten(:,3),data_ten(:,4),data_ten(:,5),data_ten(:,6),data_ten(:,7)
);
createfigure(time_snip,data_snip(:,1),data_snip(:,3),data_snip(:,4),data_snip(:,5),data_snip(:,6),d
ata_snip(:,7));
createfigure(time_snip,data_ten_snip(:,1),data_ten_snip(:,3),data_ten_snip(:,4),data_ten_snip(:,5
),data_ten_snip(:,6),data_ten_snip(:,7));

```

D.1.2 Parsing Hourly DSS Files from Implant

```

% script to read data from LabVIEW generated .txt files
% specifically to collate/combine hourly files generated from an implant
% 07-16-13 SEO

clear all
clc

nchan=9;
SR=400;

pname=[uigetdir('E:\PediaFlow','Select a directory') '\'];
d = dir(pname);

for t=3:length(d)

    disp(['Processing file ' [pname d(t).name]]);

    fid=fopen([pname d(t).name],'r');

    mess=textscan(fid, '%s %s %f32 %f32 %f32 %f32 %f32 %f32 %f32 %f32 %f32');
    data=[mess{3},mess{4},mess{5},mess{6},mess{7},mess{8},mess{9},mess{10},mess{11}];

    data=double(data);

    time = linspace(0,60,length(data(:,1)));

    % LPF of data
    [b_five,a_five]=butter(1,5*2*(1/SR));
    [b_half,a_half]=butter(1,0.5*2*(1/SR));
    [b_tenth,a_tenth]=butter(1,0.1*2*(1/SR));

    for n=1:nchan

```

```

data_tenth(:,n)=filtfilt(b_tenth,a_tenth,data(:,n));
data_five(:,n)=filtfilt(b_five,a_five,data(:,n));

[~,locs]=findpeaks(data_five(:,n)-data_tenth(:,n));
data_peak(:,n)=filtfilt(b_tenth,a_tenth,interp1(time(locs),data(locs,n),time,'spline'));

[~,locs]=findpeaks(-(data_five(:,n)-data_tenth(:,n)));
data_trough(:,n)=filtfilt(b_tenth,a_tenth,interp1(time(locs),data(locs,n),time,'spline'));
end

time=downsample(time,400);
data_tenth=downsample(data_tenth,800);
data_peak=downsample(data_peak,800);
data_trough=downsample(data_trough,800);

if t==3
    avg_data=data_tenth;
    avg_peak=data_peak;
    avg_trough=data_trough;
else
    avg_data=[avg_data;data_tenth];
    avg_peak=[avg_peak;data_peak];
    avg_trough=[avg_trough;data_trough];
end

clear('data');
clear('data_tenth');
clear('data_five');
clear('data_peak');
clear('data_trough');

disp([' Data averaged and cleared, moving to next file...'])
fclose('all');
end

disp(['DONE']);

AP=avg_data(:,1);
RP=avg_data(:,3);
MS=avg_data(:,4);
LC=avg_data(:,5);
MC=avg_data(:,6);
AF=avg_data(:,7);

% createfigure(time,AP,RP,MS,LC,MC,AF);

```



```

% AP_LPF=data_LPF(:,1);
% RP_LPF=data_LPF(:,3);
% MS_LPF=data_LPF(:,4);
% LC_LPF=data_LPF(:,5);
% MC_LPF=data_LPF(:,6);
% AF_LPF=data_LPF(:,7);
%
% figure
% createfigure(time,AP_LPF,RP_LPF,MS_LPF,LC_LPF,MC_LPF,AF_LPF);

```

D.1.3 Parse Individual Pulse Duplicator File

```

% 06-13-18 SEO
% modified to read DSS/DAPP flow estimator files used w/ pulse duplicator
% 12 floating point columns (+ added 3 more %f32)

% 1) date (M/d/yyyy)
% 2) time (HH:mm:ss.SSSSSS)
% 3) pump outlet (mmHg) - Pout_DP
% 4) pump inlet (mmHg) - Pin_DP
% 5) rotor position (V) - RP
% 6) speed (krpm) - PS
% 7) levitation current
% 8) motor current (Arms) - MC
% 9) pump flow (L/min) - PF
% 10) total flow - TF
% 11) ventricle pressure
% 12) arterial pressure
% 13,14) est flow, flow pulse (disregard)

% 07-16-13 SEO
% script to read data from LabVIEW generated .txt files
% specifically to examine individual files

clear;

SR=400;

[fname,pname]=uigetfile('D:\Box Sync\Lab Work\PF4.x\Flow Estimator\*.txt');
d = dir(pname);

disp(['Processing file ' [pname fname]]);
fid=fopen([pname fname],'r');

```

```

% Read from DAPP files - 9 channels
% 1) date (M/d/yyyy)
% 2) time (HH:mm:ss.SSSSSS)
% 3) pump outlet (mmHg) - Pout_DP
% 4) pump inlet (mmHg) - Pin_DP
% 5) rotor position (V) - RP
% 6) speed (krpm) - PS
% 7) levitation current
% 8) motor current (Arms) - MC
% 9) pump flow (L/min) - PF
% 10,11) est flow, flow pulse (disregard)
mess=textscan(fid,'%{M/d/yyyy}D %{HH:mm:ss.SSSSSS}D %f32 %f32 %f32 %f32 %f32
%f32 %f32 %f32 %f32');
data=[mess{3},mess{4},mess{5},mess{6},mess{7},mess{8},mess{9}];

```

```

% Read from pulse duplicator/ EF program files -12 channels
% 1) date (M/d/yyyy)
% 2) time (HH:mm:ss.SSSSSS)
% 3) pump outlet (mmHg) - Pout_DP
% 4) pump inlet (mmHg) - Pin_DP
% 5) rotor position (V) - RP
% 6) speed (krpm) - PS
% 7) levitation current
% 8) motor current (Arms) - MC
% 9) pump flow (L/min) - PF
% 10) total flow - TF
% 11) ventricle pressure
% 12) arterial pressure
% 13,14) est flow, flow pulse (disregard)
% mess=textscan(fid,'%{M/d/yyyy}D %{HH:mm:ss.SSSSSS}D %f32 %f32 %f32 %f32 %f32
%f32 %f32 %f32 %f32 %f32 %f32 %f32 %f32');
% data=[mess{3},mess{4},mess{5},mess{6},mess{7},mess{8},mess{9},mess{10},mess{11},m
ess{12}];

```

```
data=double(data);
```

```
nchan=length(data(1,:));
```

```

% time = linspace(0,60,length(data(:,1)));
% time = linspace(0,length(data(:,1))/SR,length(data(:,1)));
mess{1}.Format='MM-dd-yyyy HH:mm:ss.SSS';
mess{2}.Format='MM-dd-yyyy HH:mm:ss.SSS';

```

```

time = mess{1}+timeofday(mess{2});

% LPF of data
% [b_five,a_five]=butter(1,5*2*(1/SR));
% [b_half,a_half]=butter(1,0.5*2*(1/SR));
% [b_tenth,a_tenth]=butter(1,0.1*2*(1/SR));

% 10Hz LPF coeffs
[b_ten,a_ten]=butter(1,10*2*(1/SR));

for n=1:nchan
%   data_tenth(:,n)=filtfilt(b_tenth,a_tenth,data(:,n));
%   data_five(:,n)=filtfilt(b_five,a_five,data(:,n));

    data_ten(:,n)=filtfilt(b_ten,a_ten,data(:,n));
%
%   [~,locs]=findpeaks(data_five(:,n)-data_tenth(:,n));
%   data_peak(:,n)=filtfilt(b_tenth,a_tenth,interp1(time(locs),data(locs,n),time,'spline'));
%
%   [~,locs]=findpeaks(-(data_five(:,n)-data_tenth(:,n)));
%   data_trough(:,n)=filtfilt(b_tenth,a_tenth,interp1(time(locs),data(locs,n),time,'spline'));
%
end

% round MS to nearest 0.01
data_ten(:,4)=round(data_ten(:,4),2);

% easy to use time column
data_ten(:,nchan+1)=second(time,'secondofday');

% for plot code reuse
aggregate(1,:)=[{fname(1:4)},{data_ten},'b'];
compiled_data=data_ten;
compiled_time=time;

clear('time');
clear('mess');
% clear('data');
clear('data_ten');

disp(['DONE']);

createfigure(compiled_data(:,nchan+1),compiled_data(:,1)-
compiled_data(:,2),compiled_data(:,3),compiled_data(:,4),compiled_data(:,5),compiled_data(:,6)
,compiled_data(:,7));

```

```

% H-Q plot and overlay on time
figure;
subplot(2,1,1);
yyaxis left;
plot(aggregate{j,2}(:,8),aggregate{j,2}(:,1)-aggregate{j,2}(:,2));
yyaxis right;
plot(aggregate{j,2}(:,8),aggregate{j,2}(:,7));

subplot(2,1,2);
plot(aggregate{j,2}(:,7),aggregate{j,2}(:,1)-aggregate{j,2}(:,2));

%code to make individual pressure/flow vs time and H-Q plots
% %PF4.8
% for j=10:12
% figure;
% subplot(2,1,1);
% yyaxis left;
% plot(aggregate{j,2}(:,11),aggregate{j,2}(:,10)-aggregate{j,2}(:,9));
% yyaxis right;
% plot(aggregate{j,2}(:,11),aggregate{j,2}(:,7));
%
% subplot(2,1,2);
% plot(aggregate{j,2}(:,7),aggregate{j,2}(:,10)-aggregate{j,2}(:,9));
% end
%
% %PF4.6
% for j=8:10
% figure;
% subplot(2,1,1);
% yyaxis left;
% plot(aggregate{j,2}(:,11),aggregate{j,2}(:,1)-aggregate{j,2}(:,2));
% yyaxis right;
% plot(aggregate{j,2}(:,11),aggregate{j,2}(:,7));
%
% subplot(2,1,2);
% plot(aggregate{j,2}(:,7),aggregate{j,2}(:,1)-aggregate{j,2}(:,2));
% end

```

D.1.4 Load Pulse Duplicator DSS Files

```

% 06-16-18 SEO
% modified to read and compile all pulse duplicator files

```

```

% 1) date (M/d/yyyy)
% 2) time (HH:mm:ss.SSSSSS)
% 3) pump outlet (mmHg) - Pout_DP
% 4) pump inlet (mmHg) - Pin_DP
% 5) rotor position (V) - RP
% 6) speed (krpm) - PS
% 7) levitation current
% 8) motor current (Arms) - MC
% 9) pump flow (L/min) - PF
% 10) total flow - TF
% 11) ventricle pressure
% 12) arterial pressure
% 13,14) est flow, flow pulse (disregard)

% script to read data from LabVIEW generated .txt files
% 07-16-13 SEO

```

```

clear all
clc

```

```

% PFx = 'PF4.6';
PFx = 'PF4.8';

```

```

SR=400;
rpmcolors=['m';'c';'g';'r';'b';'m';'c'];
plotcolors=[0.600000023841858 0.839215695858002 1;
0 0.541176497936249 0.898039221763611;
0.298039227724075 0.721568644046783 1;
0.815686285495758 0.909803926944733 0.686274528503418;
0.678431391716003 0.847058832645416 0.450980395078659;
0.537254929542542 0.780392169952393 0.215686276555061;
0.921568632125854 0.376470595598221 0.47843137383461;
0.886274516582489 0.109803922474384 0.254901975393295;
0.952941179275513 0.643137276172638 0.701960802078247;
1 0.298039227724075 1;
1 0 1;
1 0.600000023841858 1;
0.925490200519562 0.537254929542542 0.368627458810806;
0.890196084976196 0.337254911661148 0.105882354080677;
0.95686274766922 0.733333349227905 0.639215707778931;
0 0.447058826684952 0.74117648601532;
0 0.447058826684952 0.74117648601532;
0.466666668653488 0.674509823322296 0.18823529779911;
0.466666668653488 0.674509823322296 0.18823529779911;
0.466666668653488 0.674509823322296 0.18823529779911;

```

```

0.709803938865662 0.0862745121121407 0.20392157137394;
0.709803938865662 0.0862745121121407 0.20392157137394;
0.709803938865662 0.0862745121121407 0.20392157137394;
0.749019622802734 0 0.749019622802734;
0.749019622802734 0 0.749019622802734;
0.749019622802734 0 0.749019622802734;
0.749019622802734 0 0.749019622802734;
0.850980401039124 0.325490206480026 0.0980392172932625;
0.850980401039124 0.325490206480026 0.0980392172932625;
0.850980401039124 0.325490206480026 0.0980392172932625;
0.850980401039124 0.325490206480026 0.0980392172932625 ];

```

```

pname=[uigetdir('D:\Box Sync\Lab Work\PF4.x\Flow Estimator','Select a directory') '\'];
d = dir(pname);

```

```

for t=3:length(d)

```

```

    disp(['Processing file ' [pname d(t).name]);

```

```

    fid=fopen([pname d(t).name],'r');

```

```

% mess=textscan(fid, '%s %s %f32 %f32 %f32 %f32 %f32 %f32 %f32 %f32 %f32');
%

```

```

data=[mess{3},mess{4},mess{5},mess{6},mess{7},mess{8},mess{9},mess{10},mess{11}];

```

```

    mess=textscan(fid,'% {M/d/yyyy}D % {HH:mm:ss.SSSSS}D %f32 %f32 %f32 %f32 %f32
%f32 %f32 %f32 %f32 %f32 %f32 %f32');

```

```

data=[mess{3},mess{4},mess{5},mess{6},mess{7},mess{8},mess{9},mess{10},mess{11},mess
{12}];

```

```

    data=double(data);

```

```

    nchan=length(data(1,:));

```

```

% format time

```

```

mess{1}.Format='MM-dd-yyyy HH:mm:ss.SSS';

```

```

mess{2}.Format='MM-dd-yyyy HH:mm:ss.SSS';

```

```

    time = mess{1}+timeofday(mess{2});

```

```

% flow estimator for PF4.6

```

```

% data(:,10)=0.8*(460502097.944 + 45678592*(data(:,4).^2) + 427128023.204.*data(:,6) + -
8268351850*abs(data(:,3)))/(173167168.*data(:,4));

```

```

% flow estimator for PF4.7/4.8
% data(:,11)=0.8*(-513*121580*-42.81 + 0.0673*(data(:,4).^2)*1088*(0.64)*(10^6) + -
513*121580*-6.82.*data(:,6) + -
513*121580*143.2*abs(data(:,3)))/((10^3).*data(:,4)*1088*159.161);

% time = linspace(0,60,length(data(:,1)));

% LPF of data
% [b_five,a_five]=butter(1,5*2*(1/SR));
% [b_half,a_half]=butter(1,0.5*2*(1/SR));
% [b_tenth,a_tenth]=butter(1,0.1*2*(1/SR));
[b_ten,a_ten]=butter(1,10*2*(1/SR));

for n=1:nchan
% data_tenth(:,n)=filtfilt(b_tenth,a_tenth,data(:,n));
% data_five(:,n)=filtfilt(b_five,a_five,data(:,n));

data_ten(:,n)=filtfilt(b_ten,a_ten,data(:,n));
%
% [~,locs]=findpeaks(data_five(:,n)-data_tenth(:,n));
% data_peak(:,n)=filtfilt(b_tenth,a_tenth,interp1(time(locs),data(locs,n),time,'spline'));
%
% [~,locs]=findpeaks(-(data_five(:,n)-data_tenth(:,n)));
% data_trough(:,n)=filtfilt(b_tenth,a_tenth,interp1(time(locs),data(locs,n),time,'spline'));
end

% time=downsample(time,400);
% data_tenth=downsample(data_tenth,800);
% data_peak=downsample(data_peak,800);
% data_trough=downsample(data_trough,800);

% round MS to nearest 0.01
data_ten(:,4)=round(data_ten(:,4),2);

data_ten(:,nchan+1)=second(time,'secondofday');

if t==3
% avg_data=data_tenth;
% avg_peak=data_peak;
% avg_trough=data_trough;

compiled_data=data_ten;
compiled_time=time;

% first instance for rpm colors

```

```

        i=1;
    else
    %     avg_data=[avg_data;data_tenth];
    %     avg_peak=[avg_peak;data_peak];
    %     avg_trough=[avg_trough;data_trough];

        compiled_data=[compiled_data;data_ten];
        compiled_time=[compiled_time;time];

        % check rpm and iterate colors if changed
        if strcmp(d(t).name(1:4),aggregate{t-2-1,1})
            i=i;
        else
            i=i+1;
        end

    end

    aggregate(t-2,:)=[{d(t).name(1:4)},{data_ten},rpmcolors(i)];

    clear('mess');
    clear('data');
    clear('data_ten');
    clear('time');

    % clear('data_tenth');
    % clear('data_five');
    % clear('data_peak');
    % clear('data_trough');

    disp([' Data averaged and cleared, moving to next file...'])
    fclose('all');
end

disp(['DONE']);

if strcmp(PFx,'PF4.6')

    createfigure(compiled_data(:,nchan+1),compiled_data(:,1)-
compiled_data(:,2),compiled_data(:,3),compiled_data(:,4),compiled_data(:,5),compiled_data(:,6)
,compiled_data(:,7));

else if strcmp(PFx,'PF4.8')

```



```

    createfigure(compiled_data(:,nchan+1),compiled_data(:,10)-
compiled_data(:,9),compiled_data(:,3),compiled_data(:,4),compiled_data(:,5),compiled_data(:,6)
,compiled_data(:,7));

    end
end

% marker symbols
marker=[ '-' ;
        'x' ];

% marker  i)size ii)spacing
marker_prop=[ 5 , 50.0 ;
              10 , 100.0 ];

%H-Q Plot
figure;
hold on;
for m=1:2
    if m==1
        aggregate=agg_svr;
    else
        aggregate=agg_clamp;
    end

    for j=1:length(aggregate(:,1))

        if strcmp(PFx,'PF4.6')

            plot(aggregate{j,2}(:,7),aggregate{j,2}(:,1)-
aggregate{j,2}(:,2),[aggregate{j,3},marker(m,:)],'MarkerSize',marker_prop(m,1),'MarkerIndices',
1:marker_prop(m,2):length(aggregate{j,2}(:,7)));

            else if strcmp(PFx,'PF4.8')

                plot(aggregate{j,2}(:,7),aggregate{j,2}(:,10)-
aggregate{j,2}(:,9),[aggregate{j,3},marker(m,:)],'MarkerSize',marker_prop(m,1),'MarkerIndices',
1:marker_prop(m,2):length(aggregate{j,2}(:,7)));

            end
        end

    end
end

legend(aggregate{:,1},'Location','northwest');

```

```
% static data... UNCOMMENT BELOW TO USE
```

```
if strcmp(PFx,'PF4.6')
    load 'D:\Box Sync\Lab Work\PF4.x\Flow Estimator\Programs\PF46_data\3-16-12\PF46_Data_Shaun'
else if strcmp(PFx,'PF4.8')
    load 'D:\Box Sync\Lab Work\PF4.x\Flow Estimator\PF4.8 Flow Estimator\PF48_Data_Shaun_norm'
    end
end

% %    static(:,1)=A(:,3); %pressure head
% %    static(:,3)=A(:,5); %rp
% %    static(:,4)=A(:,1); %ms
% %    static(:,6)=A(:,6); %mc
% %    static(:,7)=A(:,2); %flow
% %    static(:,8)=A(:,7); %curves

for d=1:5
    i=(d-1)*5+1;
    static{d}=[A(i:i+4,3),zeros(5,1),A(i:i+4,5),A(i:i+4,1),zeros(5,1),A(i:i+4,6),A(i:i+4,2)];

    plot(static{d}(:,7),static{d}(:,1)-static{d}(:,2),'k--','LineWidth',2.0);
end

% /static data...

hold off;

%MC-Q Plot
figure;
hold on;
for m=1:2
    if m==1
        aggregate=agg_svr;
        ycount=1;
    else
        aggregate=agg_clamp;
    end

    for j=1:length(aggregate(:,1))

plot(aggregate{j,2}(:,6),aggregate{j,2}(:,7),[aggregate{j,3},marker(m,:)],'Color',plotcolors(ycount
```

```

nt,:), 'MarkerSize', marker_prop(m,1), 'MarkerIndices', 1:marker_prop(m,2):length(aggregate{j,2}(:
,7)));
    ycount=ycount+1;
end
end
legend(aggregate{:,1}, 'Location', 'northwest');

for d=1:5
    i=(d-1)*5+1;

    plot(static{d}(:,6), static{d}(:,7), 'LineWidth', 2.0, 'LineStyle', '--', 'Color', [0.501960813999176
0.501960813999176 0.501960813999176]);

end

hold off;

```

D.1.5 Flow Estimation Coefficients Script

```

% A. Ferreira
% 3-19-2012
% Reads pulsatile data from PF4.6
% modified by SE Olia 1/31/13 for PF4.8

clc
clear
close all

% 1) timestamp (fyi: might appear as two columns because there is a space between the date and
time)
% 2) pump outlet (mmHg) - Pout_DP
% 3) pump inlet (mmHg) - Pin_DP
% 4) rotor position (V) - RP
% 5) speed (krpm) - PS
% 6) levitation current
% 7) motor current (Arms) - MC
% 8) pump flow (L/min) - PF
% 9) total flow - TF
% 10) ventricle pressure
% 11) arterial pressure

% 9,10) est flow, flow pulse (disregard)

```

```

fs = 400;
dt = 1/fs;

% LPF -----
filter_order = 101;
freq = 10; % cut-off frequency in Hertz
wc = 2*freq/fs; % FIR parameter
wo = 0; % FIR parameters
[fir_coeff] = firdes(filter_order, wc, wo, 2, 1); % see firdes routine
% -----

% LPF -----
filter_order = 51;
freq = 10; % cut-off frequency in Hertz
wc = 2*freq/fs; % FIR parameter
wo = 0; % FIR parameters
[LPF_10] = firdes(filter_order, wc, wo, 2, 1); % see firdes routine
% -----

MA_mean = [ones(1,1*fs)./(1*fs)];

file_list = {'10.3krpm_0.0Lpm.txt', '10.3krpm_0.5Lpm.txt',...
            '11.9krpm_0.0Lpm.txt', '11.9krpm_0.5Lpm.txt', '11.9krpm_0.8Lpm.txt', ...
            '14.0krpm_0.0Lpm.txt', '14.0krpm_0.5Lpm.txt', '14.0krpm_1.1Lpm.txt',...
            '16.1krpm_0.0Lpm.txt', '16.1krpm_0.5Lpm.txt', '16.1krpm_1.0Lpm.txt',
            '16.1krpm_1.4Lpm.txt', ...
            '18.2krpm_0.0Lpm.txt', '18.2krpm_0.5Lpm.txt', '18.2krpm_1.0Lpm.txt',
            '18.2krpm_1.5Lpm.txt'};

ind = [1,2,3,4,5,6,7,8,9];

load PF46_Data_Shaun

ms_S = A(:,1);
pf_S = A(:,2);
dp_S = A(:,3); % pump head
rp_S = abs(A(:,5));
mc_S = A(:,6);
cl_S = A(:,7);

figure; plot(rp_S, dp_S, 'ro')

% to proces PF46 data of 3/16/2012 -----

```

```

ms = ms_S;
dp = dp_S;
pf = pf_S;
mc = mc_S;
cl = cl_S;

flow = pf;
c = [1 2 3 4 5];
ln = {'ko', 'ks', 'k*', 'k+', 'kv'};

Kt = 0.00065; % Nm/Arms
D = 0.8; % cm
rho = 995.7*0.70 + 1259.37*0.30; % density kg/m^3

c_p = 8.7082e9;
c_phi = 159.161;
c_psi = 1.2158e5;

for i=1:5
    switch c(i)
        case 1
            ii = find(cl == 1);
            figure(1); subplot(1,2,1); plot(mc(ii), flow(ii), ln{i}, 'MarkerSize', 8, 'LineWidth', 2); hold
on,
                subplot(1,2,2); plot(flow(ii), dp(ii), ln{i}, 'MarkerSize', 8, 'LineWidth', 2); hold on,

            C_power{i} = power_coeff(Kt, c_p, rho, D, ms(ii), mc(ii));
            C_flow{i} = flow_coeff(c_phi, D, pf(ii), ms(ii));
            C_pressure{i} = pressure_coeff(c_psi, rho, D, dp(ii), ms(ii));

            figure(2); subplot(1,2,1); plot(C_power{i}, C_flow{i}, ln{i}, 'MarkerSize', 8,
'LineWidth', 2); hold on
                subplot(1,2,2); plot(C_flow{i}, C_pressure{i}, ln{i}, 'MarkerSize', 8, 'LineWidth',
2); hold on

        case 2
            ii = find(cl == 2);
            figure(1); plot(flow(ii), mc(ii), ln{i}, 'MarkerSize', 8, 'LineWidth', 2);
            figure(1); subplot(1,2,1); plot(mc(ii), flow(ii), ln{i}, 'MarkerSize', 8, 'LineWidth', 2); hold
on
                subplot(1,2,2); plot(flow(ii), dp(ii), ln{i}, 'MarkerSize', 8, 'LineWidth', 2); hold on

            C_power{i} = power_coeff(Kt, c_p, rho, D, ms(ii), mc(ii));
            C_flow{i} = flow_coeff(c_phi, D, pf(ii), ms(ii));
            C_pressure{i} = pressure_coeff(c_psi, rho, D, dp(ii), ms(ii));

```

```

figure(2); subplot(1,2,1); plot(C_power{i}, C_flow{i}, ln{i}, 'MarkerSize', 8,
'LineWidth', 2); hold on
    subplot(1,2,2); plot(C_flow{i}, C_pressure{i}, ln{i}, 'MarkerSize', 8, 'LineWidth',
2); hold on

case 3
    ii = find(cl == 3);
figure(1); plot(flow(ii), mc(ii), ln{i}, 'MarkerSize', 8, 'LineWidth', 2);

figure(1); subplot(1,2,1); plot(mc(ii), flow(ii), ln{i}, 'MarkerSize', 8, 'LineWidth', 2); hold
on
    subplot(1,2,2); plot(flow(ii), dp(ii), ln{i}, 'MarkerSize', 8, 'LineWidth', 2); hold on

C_power{i} = power_coeff(Kt, c_p, rho, D, ms(ii), mc(ii));
C_flow{i} = flow_coeff(c_phi, D, pf(ii), ms(ii));
C_pressure{i} = pressure_coeff(c_psi, rho, D, dp(ii), ms(ii));

figure(2); subplot(1,2,1); plot(C_power{i}, C_flow{i}, ln{i}, 'MarkerSize', 8,
'LineWidth', 2); hold on
    subplot(1,2,2); plot(C_flow{i}, C_pressure{i}, ln{i}, 'MarkerSize', 8, 'LineWidth',
2); hold on

case 4
    ii = find(cl == 4);
figure(1); plot(flow(ii), mc(ii), ln{i}, 'MarkerSize', 8, 'LineWidth', 2);

figure(1); subplot(1,2,1); plot(mc(ii), flow(ii), ln{i}, 'MarkerSize', 8, 'LineWidth', 2); hold
on
    subplot(1,2,2); plot(flow(ii), dp(ii), ln{i}, 'MarkerSize', 8, 'LineWidth', 2); hold on

C_power{i} = power_coeff(Kt, c_p, rho, D, ms(ii), mc(ii));
C_flow{i} = flow_coeff(c_phi, D, pf(ii), ms(ii));
C_pressure{i} = pressure_coeff(c_psi, rho, D, dp(ii), ms(ii));

figure(2); subplot(1,2,1); plot(C_power{i}, C_flow{i}, ln{i}, 'MarkerSize', 8,
'LineWidth', 2); hold on
    subplot(1,2,2); plot(C_flow{i}, C_pressure{i}, ln{i}, 'MarkerSize', 8, 'LineWidth',
2); hold on

case 5
    ii = find(cl == 5);

figure(1); subplot(1,2,1); plot(mc(ii), flow(ii), ln{i}, 'MarkerSize', 8, 'LineWidth', 2); hold
on
    subplot(1,2,2); plot(flow(ii), dp(ii), ln{i}, 'MarkerSize', 8, 'LineWidth', 2); hold on

```

```

C_power{i} = power_coeff(Kt, c_p, rho, D, ms(ii), mc(ii));
C_flow{i} = flow_coeff(c_phi, D, pf(ii), ms(ii));
C_pressure{i} = pressure_coeff(c_psi, rho, D, dp(ii), ms(ii));

figure(2); subplot(1,2,1); plot(C_power{i}, C_flow{i}, ln{i}, 'MarkerSize', 8,
'LineWidth', 2); hold on
        subplot(1,2,2); plot(C_flow{i}, C_pressure{i}, ln{i}, 'MarkerSize', 8, 'LineWidth',
2); hold on
        end
end

```

```

figure(1); subplot(1,2,1); legend('10.0krpm', '12.2krpm', '13.9krpm', '16krpm', '18,1krpm', 4)
        ylabel('Pump Flow (l/min)'); xlabel('Motor Current (Arms)')
        subplot(1,2,2); legend('10.0krpm', '12.2krpm', '13.9krpm', '16krpm', '18,1krpm',4)
        xlabel('Pump Flow (l/min)'); ylabel('Head pressure (mmHg)')

```

```

figure(2); subplot(1,2,1); legend('10.0krpm', '12.2krpm', '13.9krpm', '16krpm', '18.1krpm', 4)
        ylabel('Flow coefficient (\Phi)'); xlabel('Power coefficient')
        subplot(1,2,2); legend('10.0krpm', '12.2krpm', '13.9krpm', '16krpm', '18,1krpm',4)
        xlabel('Flow coefficient (\Phi)'); ylabel('Pressure coefficient (\Psi)')

```

```

flow_coeff = [];
pressure_coeff = [];
power_coeff = [];

```

```

for i=1:5
    flow_coeff = [flow_coeff; C_flow{i}];
    pressure_coeff = [pressure_coeff; C_pressure{i}];
    power_coeff = [power_coeff; C_power{i}];
end

```

22

% call regression tool in Matlab -

```

%
%
%
```

```

% load pf45_18_mloop
% load PF45_coeffs

% k1 = [1,6,13,20,28];
% k2 = [5,12,19,27,35];

c = [1 2 3 4 5];
% ps = []; DDP = []; FF = []; MMC = [];

for i = 2 % 1:length(ind)

fid = fopen(file_list{ind(i)});
i;
file_list{ind(i)}

% fid = fopen('10.3K_100MAP.txt');
C = textscan(fid, '%s %s %f %f %f %f %f %f %f %f %f %f %f');
fclose(fid);

N = length(C{1});
time = (0:N-1)*dt;
% t1 = 5;
% t2 = 8;
t1 = 0;
t2 = time(end);

i0 = find(time >=t1 & time <= t2);
time = time(i0); time = time';

Pout_h = C{3}; Pout_h = Pout_h(i0);
Pin_h = C{4}; Pin_h = Pin_h(i0);
RP = C{5}; RP = RP(i0);
PS = C{6}; PS = PS(i0);
LC = C{7}; LC = LC(i0);
MC = C{8}; MC = MC(i0); % MC = 0.292*MC + 0.407;
Flow = C{9}; Flow = Flow(i0);
TF = C{10}; TF = TF(i0);
LVP = C{11}; LVP = LVP(i0);
AP = C{12}; AP = AP(i0);
x1 = C{13}; x1 = x1(i0);
x2 = C{14}; x2 = x2(i0);

H = Pout_h - Pin_h;
%
```



```

h = filtfilt(fir_coeff, 1, H);
pf = filtfilt(fir_coeff, 1, Flow);
rp = filtfilt(fir_coeff, 1, RP);
%
%
% figure; plot(time, Pout_h)
% figure; plot(time, Pin_h)
%
% figure; plot(pf ,h)
% figure; plot(rp, h)
%
%
% end
%
%
% for simulink file
%
t1 = 0;
t2 = time(end);

PIN = [time - t1 Pin_h];
POUT = [time - t1 Pout_h];
PS = [time - t1 PS];
C = [time - t1 MC]; % calibration current
Q = [time - t1 Flow];
RRP = [time - 1 RP];

tt = time(end)-5;
X2 = [time - t1 x2];

F_est_PF46_2

end

p1 = -494.6;
p2 = 0.06562;

a1 = -7.658;
a2 = -7.103;
a3 = 137.5;

%
% X2 = filtfilt(fir_coeff, 1, x2);
% X2 = filtfilt(MA_mean, 1, X2);
%

```

```

% H = Pout_h - Pin_h;
% a = diff(Pout_h);
%
% i3 = k1(i):k2(i);
% figure(100); plot(FF(i3), DDP(i3), '-r'); hold on
%     plot(Flow, H, 'b')
%
% figure(200); plot(time, Flow, 'b', time, X2, 'r')

% figure(1); plot(time, Pout_h, time, Pin_h)
% figure(2); plot(time, MC)
% figure(3); plot(time, Flow)
%
% 22
%
%
% t5 = ScopeData1.time;
% v1 = ScopeData1.signals(1,1).values;
% v2 = ScopeData1.signals(1,2).values;
%
% figure(110); subplot(211); plot(t5, v1); hold on
%     plot(time, H, 'k')
%     subplot(212); plot(t5, v2); hold on
%     plot(time, Flow, 'k')
% xx = [-0.5 2];
% yy = [-0.5 2];
% NN1 = length(v2);
% NN2 = length(v4);
% v3 = v1; v4 = v2;
%
% figure(213); subplot(121); plot(v2(1:100:NN1,1), v2(1:100:NN1,2), 'ro'); hold on
%     plot(v4(1:100:NN2,1), v4(1:100:NN2,2), 'bs')
%     xx = [-0.5 2];
%     yy = [-0.5 2];
%     plot(xx, yy, 'k--')
%     xlabel('Mean Q measured (l/min)')
%     ylabel('Mean Q estimated (l/min)')
%     subplot(122); plot(v1(1:100:NN1,1), v1(1:100:NN1,2), 'ro'); hold on
%     plot(v3(1:100:NN2,1), v3(1:100:NN2,2), 'bs')
%     xx = [0 150];
%     yy = [0 150];
%     plot(xx, yy, 'k--')
%     xlabel('Mean H measured (mmHg)')
%     ylabel('Mean H estimated (mmHg)')
%
%

```

```

% save flow_pulsatile v1 v2
% load flow_pulsatile
%

% for simulink file

% PIN = [time - t1 Pin_h];
% POUT = [time - t1 Pout_h];
% PS = [time - t1 MS];
% C = [time - t1 MC]; % calibration current
% Q = [time - t1 Flow];
% tt = time(end);
%
% H_est_PF45_new_ml

% So, using  $Q_{est} = f(\text{motor speed, motor current})$ , these are the new coefficients:
%  $a = [-2.528, 0.04916, 7.014, -0.4856, 1.387]^T$ 
% Variable vector is  $X = [1, ms, mc, ms*mc, mc^2]$ ,
% and  $Q_{est} = X*a$ . (ms = motor speed in Krpm, mc = motor current in Arms).

%
%
% mc = filtfilt(fir_coeff, 1, MC);
% mc = filtfilt(MA_mean, 1, mc);
%
% a = diff(Pout_h);
% if Pout_h(10) > Pout_h(end-5)
%   ii = find(a < -2);
% else
%   ii = find(a > 2);
% end
%
% figure(i); subplot(211); plot(time, Pout_h); hold on
%       plot(time(ii), Pout_h(ii), 'ro')
%       subplot(212); plot(time(2:end), a)
%
% H = Pout_h - Pin_h;
%
% for j=1:length(ii)
%   h(j) = mean(H(ii(j)-20:ii(j)-10));
%   f(j) = mean(Flow(ii(j)-20:ii(j)-10));
%   mc2(j) = mean(mc(ii(j)-20:ii(j)-10));
%   ps = [ps; mean(PS)];

```

```

% end
%
% h(j+1) = mean(H(ii(j)+10:ii(j)+20));
% f(j+1) = mean(Flow(ii(j)+10:ii(j)+20));
% mc2(j+1) = mean(mc(ii(j)+10:ii(j)+20));
% DDP = [DDP; h'];
% FF = [FF; f'];
% MMC = [MMC; mc2'];
%
% ps = [ps; mean(PS)];
%
% figure(i); subplot(211); plot(time, H); hold on
%         plot(time(ii), H(ii), 'ro')
%         subplot(212); plot(time, mc)
%
% i2 = find(cl_S == i);
%
% figure(100); plot(pf_S(i2), dp_S(i2), '-bo', 'MarkerSize', 10, 'LineWidth', 3); hold on
%         plot(f, h, '-rs', 'MarkerSize', 10, 'LineWidth', 3)
%
% figure(200); plot(pf_S(i2), mc_S(i2), '-bo', 'MarkerSize', 10, 'LineWidth', 3); hold on
%         plot(f, mc2, '-rs', 'MarkerSize', 10, 'LineWidth', 3)
%
%
% end
%
% save pf45_18_mloop DDP FF MMC ps
%
%
% 'fim'
%
%
%
%
%
%
%
%
% save pf45_16_loop2 MM

% ii = 1:5;
% ii = 6:10;

```

```

% ii = 17:21;
% ii = 22:25;
%
%
% figure(13); plot(MM(:,2), MM(:,5), 'rs'); hold on
% plot(pf_S(ii), mc_S(ii), 'kv')
% figure(11); plot(MM(:,2), MM(:,3), 'ro'); hold on
% plot(pf_S(ii), dp_S(ii), 'kv')
%
% save pf45_16_loop MM

%
% xx = [0 2];
% yy = [0 2];
%
% figure(211); plot(fl_m, fl_est_m, 'ro'); hold on
% xlabel('Mean Q estimated (l/min)')
% ylabel('Mean Q measured (l/min)')
% figure(211); plot(xx, yy, 'k:')
%
%

```

BIBLIOGRAPHY

- [1] Olia SE, Wearden PD, Maul TM, et al. Preclinical performance of a pediatric mechanical circulatory support device: The PediaFlow ventricular assist device. *The Journal of Thoracic and Cardiovascular Surgery*. 2018.
- [2] *AHA 2005 Statistical Reference Book*. Dallas: American Heart Association; 2005.
- [3] Lipshultz SE, Sleeper LA, Towbin JA, et al. The incidence of pediatric cardiomyopathy in two regions of the United States. *N ENGL J MED*. 2003:1647-1655.
- [4] Boneva RS, Botto LD, Moore CA, Yang Q, Correa A, Erickson JD. Mortality associated with congenital heart defects in the United States: trends and racial disparities, 1979-1997. *Circulation*. 2001:2376-2381.
- [5] Almond CS, Thiagarajan RR, Piercey GE, et al. Waiting List Mortality Among Children Listed for Heart Transplantation in the United States. *Circulation*. 2009:717-727.
- [6] Organ Procurement and Transplantation Network. Vol 2015: U.S. Department of Health & Human Services.
- [7] Baldwin JT, Borovetz HS, Duncan BW, et al. The National Heart, Lung, and Blood Institute Pediatric Circulatory Support Program. *Circulation*. 2006;113:147-155.
- [8] Goldman AP, Cassidy J, de Leval M, et al. The waiting game: bridging to paediatric heart transplantation. *Lancet*. 2003:1967-1970.
- [9] Mozaffarian D, Benjamin EJ, Go AS, et al. Heart Disease and Stroke Statistics—2015 Update: A Report From the American Heart Association. *Circulation*. 2015;131:e29-e322.
- [10] Garatti A, Bruschi G, Colombo T, et al. Clinical outcome and bridge to transplant rate of left ventricular assist device recipient patients: comparison between continuous-flow and pulsatile-flow devices. *Eur J Cardiothorac Surg*. 2008;34:276-280.
- [11] Lahpor JR. State of the art: implantable ventricular assist devices. *Curr Opin Organ Transplant*. 2009;14:554-559.

- [12] Slaughter MS, Rogers JG, Milano CA, et al. Advanced heart failure treated with continuous-flow left ventricular assist device. *N ENGL J MED*. 2009;361:2241-2251.
- [13] Clegg AJ, Scott DA, Loveman E, Colquitt J, Royle P, Bryant J. Clinical and cost-effectiveness of left ventricular assist devices as destination therapy for people with end-stage heart failure: a systematic review and economic evaluation. *Int. J. Technol. Assess. Health Care*. 2007;23:261–268.
- [14] Deiwick M, Hoffmeier A, Tjan TD. Heart failure in children- Mechanical assistance. *Thorac Cardiovasc Surg*. 2005:S135-S140.
- [15] Kulik TJ, Moler FW, Palmisano JM. Outcome-associated factors in pediatric patients treated with extracorporeal membrane oxygenator after cardiac surgery. *Circulation*. 1996:1163-1168.
- [16] Kirklin JK, Naftel DC, Pagani FD, et al. Seventh INTERMACS annual report: 15,000 patients and counting. *The Journal of Heart and Lung Transplantation*. 2015:10.
- [17] Honjo O, Rao V. Implantation of HeartWare Left Ventricular Assist Device in Pediatric Population. *Operative Techniques in Thoracic and Cardiovascular Surgery*. 2014;19:80-95.
- [18] Kirklin JK, Pearce FB, Pamboukian SV, et al. Implantation of the HeartWare HVAD in a child after a recent thromboembolic stroke. *The Annals of thoracic surgery*. 2012;93:977-978.
- [19] D'Alessandro D, Forest SJ, Lamour J, Hsu D, Weinstein S, Goldstein D. First reported use of the heartware HVAD in the US as bridge to transplant in an adolescent. *Pediatric transplantation*. 2012;16:E356-359.
- [20] VanderPluym CJ, Fynn-Thompson F, Blume ED. Ventricular Assist Devices in Children: Progress With an Orphan Device Application. *Circulation*. 2014;129:1530-1537.
- [21] Sharma MS, Webber SA, Morell VO, et al. Ventricular Assist Device Support in Children and Adolescents as a Bridge to Heart Transplantation. *The Annals of Thoracic Surgery*. 2006;82:926-932.
- [22] Fraser CDJ, Jaquiss RDB, Rosenthal DN, et al. Prospective trial of a pediatric ventricular assist device. *N ENGL J MED*. 2012;367:532-541 (supplementary appendix).
- [23] Olie SE, Maul TM, Antaki JF, Kameneva MV. Mechanical blood trauma in assisted circulation: sublethal RBC damage preceding hemolysis. *Int J Artif Organs*. 2016:0.
- [24] Wintrobe MM. *Clinical Hematology*. 6 ed. Philadelphia, Pa: Lea & Febiger; 1967.

- [25] L'Acqua C, Hod E. New perspectives on the thrombotic complications of haemolysis. *British Journal of Haematology*. 2015;168:175-185.
- [26] Whitson BA, Eckman P, Kamdar F, et al. Hemolysis, pump thrombus, and neurologic events in continuous-flow left ventricular assist device recipients. *Ann Thorac Surg*. 2014;97:2097-2103.
- [27] Starling RC, Moazami N, Silvestry SC, et al. Unexpected Abrupt Increase in Left Ventricular Assist Device Thrombosis. *New England Journal of Medicine*. 2014;370:33-40.
- [28] Berger S, Salzman EW. Thromboembolic complication of prosthetic devices. *Progress in hemostasis and thrombosis*. 1973;2:273-309.
- [29] Sutura SP. Flow-induced trauma to blood cells. *Circulation research*. 1977;41:2-8.
- [30] Wurzinger L, Opitz R. Hematological principles of hemolysis and thrombosis with special reference to rotary blood pumps. *International Workshop on Rotary Blood Pumps* 1991.
- [31] Mecozzi G, Milano AD, De Carlo M, et al. Intravascular hemolysis in patients with new-generation prosthetic heart valves: a prospective study. *The Journal of thoracic and cardiovascular surgery*. 2002;123:550-556.
- [32] Maraj R, Jacobs LE, Ioli A, Kotler MN. Evaluation of hemolysis in patients with prosthetic heart valves. *Clinical cardiology*. 1998;21:387-392.
- [33] Ismeno G, Renzulli A, Carozza A, et al. Intravascular hemolysis after mitral and aortic valve replacement with different types of mechanical prostheses. *International journal of cardiology*. 1999;69:179-183.
- [34] Leverett L, Hellums J, Alfrey C, Lynch E. Red blood cell damage by shear stress. *Biophysical journal*. 1972;12:257.
- [35] Maul TM, Kameneva MV, Wearden PD. *Mechanical Blood Trauma in Circulatory-Assist Devices*. ASME Press, New York, NY: Momentum Press; 2015.
- [36] Zhang J, Gellman B, Koert A, et al. Computational and experimental evaluation of the fluid dynamics and hemocompatibility of the CentriMag blood pump. *Artif Organs*. 2006;30:168-177.
- [37] Zhang J, Koert A, Gellman B. Optimization of a Minature Maglev Ventricular Assist Device for Pediatric Circulatory Support. *ASAIO J*. 2007:23-31.

- [38] LaRose JA, Tamez D, Ashenuga M, Reyes C. Design Concepts and Principle of Operation of the HeartWare Ventricular Assist System. *ASAIO Journal*. 2010;56:285-289.
- [39] Thamsen B, Blümel B, Schaller J, et al. Numerical analysis of blood damage potential of the HeartMate II and HeartWare HVAD rotary blood pumps. *Artificial organs*. 2015;39:651-659.
- [40] Thamsen B, Mevert R, Lommel M, et al. A two-stage rotary blood pump design with potentially lower blood trauma: a computational study. *Int J Artif Organs*. 2016;39:178-183.
- [41] Shapira Y, Bairey O, Vatury M, Magen-Nativ H, Prokocimer M, Sagie A. Erythropoietin can obviate the need for repeated heart valve replacement in high-risk patients with severe mechanical hemolytic anemia: case reports and literature review. *The Journal of heart valve disease*. 2001;10:431-435.
- [42] Blackshear P. Mechanical hemolysis in flowing blood: Prentice-Hall, Inc.: Englewood Cliffs, NJ, USA; 1972:501-528.
- [43] Seiyama A, Suzuki Y, Tateshi N, Maeda N. Viscous properties of partially hemolyzed erythrocyte suspension. *Biorheology*. 1991;28:452.
- [44] Minneci PC, Deans KJ, Zhi H, et al. Hemolysis-associated endothelial dysfunction mediated by accelerated NO inactivation by decompartmentalized oxyhemoglobin. *Journal of Clinical Investigation*. 2005;115:3409.
- [45] Schmidt A. *Zur Blutlehre*: FCW Vogel; 1892.
- [46] Wurzinger L, Blasberg P, Schmid-Schönbein H. Towards a concept of thrombosis in accelerated flow: rheology, fluid dynamics, and biochemistry. *Biorheology*. 1984;22:437-450.
- [47] Brinsfield D, Hopf M, Geering R, Galletti P. Hematological changes in long-term perfusion. *Journal of applied physiology*. 1962;17:531-534.
- [48] Bernstein EF, Castaneda AR, Varco RL. SOME BIOLOGIC LIMITATIONS TO PROLONGED BLOOD PUMPING. *ASAIO Journal*. 1965;11:118-121.
- [49] Bernstein EF, Indeglia RA, Shea MA, Varco RL. Sublethal damage to the red blood cell from pumping. *Circulation*. 1967;35:1226-233.
- [50] Indeglia R, Shea M, Forstrom R, Bernstein E. Influence of mechanical factors on erythrocyte sublethal damage. *ASAIO Journal*. 1968;14:264-272.

- [51] Sandza Jr J, Clark R, Weldon C, Sutura S. Subhemolytic trauma of erythrocytes: recognition and sequestration by the spleen as a function of shear. *ASAIO Journal*. 1974;20:457-462.
- [52] Pierce CN, Larson DF, Arabia FA, Copeland JG. Inflammatory mediated chronic anemia in patients supported with a mechanical circulatory assist device. *The Journal of extracorporeal technology*. 2004;36:10-15.
- [53] Pierce CN, Larson DF. Inflammatory cytokine inhibition of erythropoiesis in patients implanted with a mechanical circulatory assist device. *Perfusion*. 2005;20:83-90.
- [54] Hung T-C, Butter DB, Yie C, et al. Effects of long-term Novacor artificial heart support on blood rheology. *ASAIO transactions/American Society for Artificial Internal Organs*. 1990;37:M312-313.
- [55] Hung TC, Butter DB, Kormos RL, et al. Characteristics of blood rheology in patients during Novacor left ventricular assist system support. *ASAIO Trans*. 1989;35:611-613.
- [56] Ganong WF. *Review of medical physiology*. 15 ed. Norwalk, CT: Appleton & Lange; 1991.
- [57] Chien S. Shear dependence of effective cell volume as a determinant of blood viscosity. *Science*. 1970;168:977-979.
- [58] Kameneva MV, Undar A, Antaki JF, Watach MJ, Calhoon JH, Borovetz HS. Decrease in red blood cell deformability caused by hypothermia, hemodilution, and mechanical stress: factors related to cardiopulmonary bypass. *ASAIO J*. 1999;45:307-310.
- [59] Lee SS, Antaki JF, Kameneva MV, et al. Strain hardening of red blood cells by accumulated cyclic supraphysiological stress. *Artificial organs*. 2007;31:80-86.
- [60] Marascalco PJ, Ritchie SP, Snyder TA, Kameneva MV. Development of standard tests to examine viscoelastic properties of blood of experimental animals for pediatric mechanical support device evaluation. *ASAIO journal*. 2006;52:567-574.
- [61] Baskurt OK, Uyuklu M, Meiselman HJ. Protection of erythrocytes from sub-hemolytic mechanical damage by nitric oxide mediated inhibition of potassium leakage. *Biorheology*. 2004;41:79-89.
- [62] Lee SS, Ahn KH, Lee SJ, Sun K, Goedhart PT, Hardeman MR. Shear induced damage of red blood cells monitored by the decrease of their deformability. *Korea-Australia Rheology Journal*. 2004:141-146.
- [63] Mizuno T, Tsukiya T, Taenaka Y, et al. Ultrastructural alterations in red blood cell membranes exposed to shear stress. *Asaio Journal*. 2002;48:668-670.

- [64] Kameneva MV, Antaki JF, Borovetz HS, et al. Mechanisms of Red Blood Cell Trauma in Assisted Circulation: Rheologic Similarities of Red Blood Cell Transformations Due to Natural Aging and Mechanical Stress. *ASAIO Journal*. 1995;41:M457-M460.
- [65] Dao K, O'Rear E, Johnson A, Peitersen S. Sensitivity of the erythrocyte membrane bilayer to subhemolytic mechanical trauma as detected by fluorescence anisotropy. *Biorheology*. 1993;31:69-76.
- [66] Chien S. Red cell deformability and its relevance to blood flow. *Annual review of physiology*. 1987;49:177-192.
- [67] Baskurt OK, Hardeman MR, Uyuklu M, et al. Comparison of three commercially available ektacytometers with different shearing geometries. *Biorheology*. 2009;46:251-264.
- [68] Popel AS, Johnson PC, Kameneva MV, Wild MA. Capacity for red blood cell aggregation is higher in athletic mammalian species than in sedentary species. *Journal of Applied Physiology*. 1994;77:1790-1794.
- [69] Fåhræus R, Lindqvist T. The viscosity of the blood in narrow capillary tubes. *American Journal of Physiology--Legacy Content*. 1931;96:562-568.
- [70] Seiyama A, Suzuki Y, Maeda N. Increased viscosity of erythrocyte suspension upon hemolysis. *Colloid and Polymer Science*. 1993;271:63-69.
- [71] Ami RB, Barshtein G, Zeltser D, et al. Parameters of red blood cell aggregation as correlates of the inflammatory state. *American Journal of Physiology-Heart and Circulatory Physiology*. 2001;280:H1982-H1988.
- [72] Gu Y, Graaff R, De Hoog E, et al. Influence of hemodilution of plasma proteins on erythrocyte aggregability: an in vivo study in patients undergoing cardiopulmonary bypass. *Clinical hemorheology and microcirculation*. 2004;33:95-107.
- [73] Carney E, Litwak K, Weiss W, Group AMW. Animal models for pediatric circulatory support device pre-clinical testing: National Heart, Lung, and Blood Institute Pediatric Assist Device Contractor's Meeting Animal Models Working Group. *ASAIO Journal*. 2009;55:6-9.
- [74] Kameneva MV, Antaki JF. Mechanical trauma to blood. In: Baskurt OK, Harderman MR, Rampling MW, Meiselman HJ, eds. *Handbook of Hemorheology and Hemodynamics*. Amsterdam: IOS Press; 2007:206-227.
- [75] Kameneva MV, Antaki JF, Butler KC, et al. A sheep model for the study of hemorheology with assisted circulation. Effect of an axial flow blood pump. *ASAIO J*. 1994;40:959-963.

- [76] Maeda N, Imaizumi K, Sekiya M, Shiga T. Rheological characteristics of desialylated erythrocytes in relation to fibrinogen-induced aggregation. *Biochimica et Biophysica Acta (BBA)-Biomembranes*. 1984;776:151-158.
- [77] Hadengue A, Razavian S, Del-Pino M, Simon A, Levenson J. Influence of sialic acid on erythrocyte aggregation in hypercholesterolemia. *Thrombosis and haemostasis*. 1996;76:944-949.
- [78] Hadengue AL, Del-Pino M, Simon A, Levenson J. Erythrocyte disaggregation shear stress, sialic acid, and cell aging in humans. *Hypertension*. 1998;32:324-330.
- [79] Baskurt OK, Uykulu M, Ulker P, et al. Comparison of three instruments for measuring red blood cell aggregation. *Clin. Hemorheol. Microcirc*. 2009;43:283-298.
- [80] Hardeman MR, Goedhart PT, Shin S. Methods in Hemorheology. In: Baskurt OK, al. e, eds. *Handbook of Hemorheology and Hemodynamics*. Vol 69. Amsterdam: IOS Press; 2007:242-266.
- [81] Kameneva MV, Antaki JF, Konishi H, et al. Effect of perfluorochemical emulsion on blood trauma and hemorheology. *ASAIO journal*. 1994;40:M576-M579.
- [82] Kameneva MV, Watach MJ, Litwak P, et al. Chronic animal health assessment during axial ventricular assistance: importance of hemorheologic parameters. *ASAIO journal*. 1999;45:183-188.
- [83] Gu L, Smith WA, Chatzimavroudis GP. Mechanical fragility calibration of red blood cells. *ASAIO journal*. 2005;51:194-201.
- [84] Herbertson LH, Olia SE, Daly AR, et al. Multi-Laboratory Study of Flow-Induced Hemolysis Using the FDA Benchmark Nozzle Model. *Artificial Organs*. 2015;39:237-248.
- [85] Bohler T, Leo A, Stadler A, Linderkamp O. Mechanical fragility of erythrocyte membrane in neonates and adults. *Pediatr Res*. 1992;32:92-96.
- [86] Kameneva M, Garrett K, Watach M, Borovetz H. Red blood cell aging and risk of cardiovascular diseases. *Clinical hemorheology and microcirculation*. 1998;18:67-74.
- [87] Kameneva M, Watach M, Borovetz H. Gender difference in rheologic properties of blood and risk of cardiovascular diseases. *CLINICAL HEMORHEOLOGY AND MICROCIRULATION*. 1999;21:357-364.
- [88] Yazer MH, Waters JH, Elkin KR, Rohrbaugh ME, Kameneva MV. A comparison of hemolysis and red cell mechanical fragility in blood collected with different cell salvage suction devices. *Transfusion*. 2008;48:1188-1191.

- [89] Raval J, Waters J, Seltsam A, et al. The use of the mechanical fragility test in evaluating sublethal RBC injury during storage. *Vox sanguinis*. 2010;99:325-331.
- [90] Daly A, Raval JS, Waters JH, Yazer MH, Kameneva MV. Effect of blood bank storage on the rheological properties of male and female donor red blood cells. *Clinical hemorheology and microcirculation*. 2014;56:337-345.
- [91] Vandromme M, McGwin G, Weinberg J. Blood transfusion in the critically ill: does storage age matter? *Scandinavian Journal of Trauma, Resuscitation and Emergency Medicine*. 2009;17:35.
- [92] Sparrow RL. Red blood cell storage duration and trauma. *Transfusion medicine reviews*. 2015;29:120-126.
- [93] Ziegler LA, Olia SE, Kameneva MV. Red Blood Cell Mechanical Fragility Test for Clinical Research Applications. *Artif Organs*. 2016;41:678-682.
- [94] Kamada T, McMillan DE, Sternlieb JJ, Björk VO, Otsuji S. Albumin prevents erythrocyte crenation in patients undergoing extracorporeal circulation. *Scandinavian journal of thoracic and cardiovascular surgery*. 1988;22:155-158.
- [95] Armstrong JK, Meiselman HJ, Fisher TC. Inhibition of red blood cell-induced platelet aggregation in whole blood by a nonionic surfactant, poloxamer 188 (Rheothrx® Injection). *Thrombosis research*. 1995;79:437-450.
- [96] Kameneva MV, Antaki JF, Yeleswarapu KK, Watach MJ, Griffith BP, Borovetz HS. Plasma protective effect on red blood cells exposed to mechanical stress. *ASAIO J*. 1997;43:M571-575.
- [97] Kameneva MV, Borovetz HS, Antaki JF, et al. Effect of Perfluorochemical Emulsion on Hemorheology and Shear Induced Blood Trauma. In: Nemoto E, LaManna J, Cooper C, et al., eds. *Oxygen Transport to Tissue XVIII*. Vol 411: Springer US; 1997:383-390.
- [98] Faraoni D, Willems A, Savan V, Demanet H, De Ville A, Van der Linden P. Plasma fibrinogen concentration is correlated with postoperative blood loss in children undergoing cardiac surgery. A retrospective review. *European journal of anaesthesiology*. 2014;31:317-326.
- [99] Miao X, Liu J, Zhao M, et al. Evidence-based use of FFP: the influence of a priming strategy without FFP during CPB on postoperative coagulation and recovery in pediatric patients. *Perfusion*. 2015;30:140-147.
- [100] Agarwal H, Barrett S, Barry K, et al. Association of Blood Products Administration During Cardiopulmonary Bypass and Excessive Post-operative Bleeding in Pediatric Cardiac Surgery. *Pediatr Cardiol*. 2015;36:459-467.

- [101] Moret E, Jacob MW, Ranucci M, Schramko AA. Albumin—Beyond Fluid Replacement in Cardiopulmonary Bypass Surgery: Why, How, and When? *Seminars in Cardiothoracic and Vascular Anesthesia*. 2014;18:252-259.
- [102] Cho JE, Shim JK, Song JW, Lee HW, Kim DH, Kwak YL. Effect of 6% hydroxyethyl starch 130/0.4 as a priming solution on coagulation and inflammation following complex heart surgery. *Yonsei medical journal*. 2014;55:625-634.
- [103] Sumpelmann R, Schürholz T, Marx G, Zander R. Protective effects of plasma replacement fluids on erythrocytes exposed to mechanical stress. *Anaesthesia*. 2000;55:976-979.
- [104] Kameneva MV, Repko BM, Krasik EF, Perricelli BC, Borovetz HS. Polyethylene glycol additives reduce hemolysis in red blood cell suspensions exposed to mechanical stress. *ASAIO journal*. 2003;49:537-542.
- [105] Hellums JD. 1993 Whitaker Lecture: biorheology in thrombosis research. *Annals of biomedical engineering*. 1994;22:445-455.
- [106] Rubenstein DA, Yin W. Quantifying the effects of shear stress and shear exposure duration regulation on flow induced platelet activation and aggregation. *Journal of thrombosis and thrombolysis*. 2010;30:36-45.
- [107] Kawahito K, Mohara J, Misawa Y, Fuse K. Platelet Damage Caused by the Centrifugal Pump: In Vitro Evaluation by Measuring the Release of α -Granule Packing Proteins. *Artificial organs*. 1997;21:1105-1109.
- [108] Koster A, Loebe M, Hansen R, et al. Alterations in coagulation after implantation of a pulsatile Novacor LVAD and the axial flow MicroMed DeBakey LVAD. *The Annals of thoracic surgery*. 2000;70:533-537.
- [109] Brown CH, Leverett LB, Lewis CW, Alfrey CP, Hellums JD. Morphological, biochemical, and functional changes in human platelets subjected to shear stress. *J Lab Clin Med*. 1975;86:462-471.
- [110] Alkhamis TM, Beissinger RL, Chediak JR. Red Blood Cell Effect on Platelet Adhesion and Aggregation in Low-Stress Shear Flow: Myth or Fact? *ASAIO Journal*. 1988;34:868-873.
- [111] Nevaril CG, Lynch EG, Alfrey CP, Hellums JD. Erythrocyte damage and destruction induced by shearing stress. *Translational Research*. 1968;71:784-790.
- [112] Turitto VT, Weiss HJ. Red Blood Cells: Their Dual Role in Thrombus Formation. *Science*. 1980;207:541-543.

- [113] Keller KH. Effect of fluid shear on mass transport in flowing blood. *Federation proceedings*. Vol 301970:1591-1599.
- [114] Wang NL, Keller K. Solute transport induced by erythrocyte motions in shear flow. *ASAIO Journal*. 1979;25:14-18.
- [115] Aarts PA, Bolhuis PA, Sakariassen KS, Heethaar RM, Sixma JJ. Red blood cell size is important for adherence of blood platelets to artery subendothelium. *Blood*. 1983;62:214-217.
- [116] Aarts P, Heethaar R, Sixma J. Red blood cell deformability influences platelets--vessel wall interaction in flowing blood. *Blood*. 1984;64:1228-1233.
- [117] Aarts P, Banga J, van Houwelingen H, Heethaar R, Sixma J. Increased red blood cell deformability due to isoxsuprine administration decreases platelet adherence in a perfusion chamber: a double-blind cross-over study in patients with intermittent claudication. *Blood*. 1986;67:1474-1481.
- [118] Tokarev A, Butylin A, Ataulakhanov F. Platelet adhesion from shear blood flow is controlled by near-wall rebounding collisions with erythrocytes. *Biophysical journal*. 2011;100:799-808.
- [119] Rosenthal J, Starling R. Coagulopathy in Mechanical Circulatory Support: A Fine Balance. *Curr Cardiol Rep*. 2015;17:1-9.
- [120] John R, Lee S. The Biological Basis of Thrombosis and Bleeding in Patients with Ventricular Assist Devices. *J. of Cardiovasc. Trans. Res*. 2009;2:63-70.
- [121] Stern DR, Kazam J, Edwards P, et al. Increased Incidence of Gastrointestinal Bleeding Following Implantation of the HeartMate II LVAD. *Journal of Cardiac Surgery*. 2010;25:352-356.
- [122] Amer S, Shah P, Hassan S. Gastrointestinal bleeding with continuous-flow left ventricular assist devices. *Clinical Journal of Gastroenterology*. 2015;8:63-67.
- [123] Stulak JM, Lee D, Haft JW, et al. Gastrointestinal bleeding and subsequent risk of thromboembolic events during support with a left ventricular assist device. *The Journal of Heart and Lung Transplantation*. 2014;33:60-64.
- [124] Schaffer JM, Arnaoutakis GJ, Allen JG, et al. Bleeding Complications and Blood Product Utilization With Left Ventricular Assist Device Implantation. *The Annals of Thoracic Surgery*. 2011;91:740-749.
- [125] Hod EA, Brittenham GM, Billote GB, et al. Transfusion of human volunteers with older, stored red blood cells produces extravascular hemolysis and circulating non-transferrin-bound iron. *Blood*. 2011;118:6675-6682.

- [126] Koch CG, Figueroa PI, Li L, Sabik JF, 3rd, Mihaljevic T, Blackstone EH. Red blood cell storage: how long is too long? *Ann Thorac Surg.* 2013;96:1894-1899.
- [127] Goldstein DJ, Seldomridge JA, Chen JM, et al. Use of aprotinin in LVAD recipients reduces blood loss, blood use, and perioperative mortality. *The Annals of Thoracic Surgery.* 1995;59:1063-1068.
- [128] Goldstein DJ, Beauford RB. Left ventricular assist devices and bleeding: adding insult to injury. *The Annals of Thoracic Surgery.* 2003;75:S42-S47.
- [129] Uriel N, Pak S-W, Jorde UP, et al. Acquired von Willebrand Syndrome After Continuous-Flow Mechanical Device Support Contributes to a High Prevalence of Bleeding During Long-Term Support and at the Time of Transplantation. *Journal of the American College of Cardiology.* 2010;56:1207-1213.
- [130] Baldwin JT, Borovetz HS, Duncan BW, Gartner MJ, Jarvik RK, Weiss WJ. The National Heart, Lung, and Blood Institute Pediatric Circulatory Support Program. A Summary of the 5-Year Experience. *Circulation.* 2011:1233-1240.
- [131] Uber BE, Webber SA, Morell VO, Antaki JF. Hemodynamic guidelines for design and control of a turbodynamic pediatric ventricular assist device. *ASAIO J.* 2006;52:471-478.
- [132] Maul TM, Kocyildirim E, Johnson CA, Jr., et al. In Vitro and In Vivo Performance Evaluation of the Second Developmental Version of the PediaFlow Pediatric Ventricular Assist Device. *Cardiovasc Eng Technol.* 2011;2:253-262.
- [133] Noh D, Antaki JF, Ricci MR, et al. Magnetic Design for the PediaFlow Ventricular Assist Device. *Artificial Organs.* 2007;32:127-135.
- [134] Antaki JF, Ricci MR, Verkaik JE, et al. PediaFlow Maglev Ventricular Assist Device: A Prescriptive Design Approach. *Cardiovasc Eng.* 2010;1:104-121.
- [135] Wu J, Antaki JF, Verkaik J, Snyder S, Ricci M. Computational Fluid Dynamics-Based Design Optimization for an Implantable Miniature Maglev Pediatric Ventricular Assist Device. *Journal of Fluids Engineering.* 2012;134:041101-041109.
- [136] Takatani S, Hoshi H, Tajima K. Feasibility of a miniature centrifugal rotary blood pump for low-flow circulation in children and infants. *ASAIO J.* 2005;51:557-562.
- [137] Badiwala MV, Ross HJ, Rao V. An unusual complication of support with a continuous-flow cardiac assist device. *N ENGL J MED.* 2007;357:936-937.
- [138] Amin DV, Antaki JF, Litwak K, Thomas D, Wu ZJ, Watach M. Induction of ventricular collapse by an axial flow blood pump. *ASAIO J.* 1998;44:M685-690.

- [139] Reesink K, Dekker A, Van der Nagel T, et al. Suction due to left ventricular assist: implications for device control and management. *Artificial Organs*. 2007;31:542-549.
- [140] Health FaDACfDaR. Guidance for Cardiopulmonary Bypass Oxygenators 510(k) Submissions; Final Guidance for Industry and FDA Staff. In: Health FaDACfDaR, ed. Silver Spring, MD: Food and Drug Administration; 2000.
- [141] Health FaDACfDaR. Implanted Blood Access Devices for Hemodialysis; Guidance for Industry and FDA Staff. In: Health FaDACfDaR, ed. Silver Spring, MD: Food and Drug Administration; 2016.
- [142] Health FaDACfDaR. Guidance for Industry and FDA Staff: General Considerations for Animal Studies for Cardiovascular Devices. In: Health FaDACfDaR, ed. Silver Spring, MD: Food and Drug Administration; 2010.
- [143] Naito K, Mizuguchi K, Nose Y. The need for standardizing the index of hemolysis. *Artificial Organs*. 1994:7-10.
- [144] F1841-97 AS. Standard Practice for Assessment of Hemolysis in Continuous Flow Blood Pumps. West Conshohocken, PA: ASTM International; Reapproved 2013.
- [145] Chan CH, Pieper IL, Hambly R, et al. The CentriMag centrifugal blood pump as a benchmark for in vitro testing of hemocompatibility in implantable ventricular assist devices. *Artif Organs*. 2015;39:93-101.
- [146] Giridharan GA, Sobieski MA, Ising M, Slaughter MS, Koenig SC. Blood trauma testing for mechanical circulatory support devices. *Biomed Instrum Technol*. 2011;45:334-339.
- [147] Bourque K, Cotter C, Dague C, et al. Design Rationale and Preclinical Evaluation of the HeartMate 3 Left Ventricular Assist System for Hemocompatibility. *Asaio j*. 2016;62:375-383.
- [148] Johnson CA, Jr., Vandenberghe S, Daly AR, et al. Biocompatibility assessment of the first generation PediaFlow pediatric ventricular assist device. *Artif Organs*. 2011;35:9-21.
- [149] Antaki JF, Butler KC, Kormos RL, et al. In-Vivo Evaluation of the Nimbus Axial Flow Ventricular Assist System: Criteria and Methods. *ASAIO J*. 1993:M231-236.
- [150] Olia SE, Herbertson LH, Malinauskas RA, Kameneva MV. A Reusable, Compliant, Small Volume Blood Reservoir for In Vitro Hemolysis Testing. *Artif Organs*. 2016.
- [151] Naito K, Suenaga E, Cao ZL, et al. Comparative hemolysis study of clinically available centrifugal pumps. *Artif Organs*. 1996;20:560-563.

- [152] Griffin MT, Grzywinski MF, Voorhees HJ, Kameneva MV, Olia SE. Ex Vivo Assessment of a Parabolic-Tip Inflow Cannula for Pediatric Continuous-Flow VADs. *Asaio j.* 2016;62:600-606.
- [153] Morrow WR, Naftel D, Chinnock R, et al. Outcome of listing for heart transplantation in infants younger than six months: predictors of death and interval to transplantation. The Pediatric Heart Transplantation Study Group. *The Journal of heart and lung transplantation: the official publication of the International Society for Heart Transplantation.* 1997;16:1255-1266.
- [154] Adachi I, Burki S, Zafar F, Morales DLS. Pediatric ventricular assist devices. *Journal of Thoracic Disease.* 2015;7:2194-2202.
- [155] Ibrahim AE, Duncan BW, Blume ED, Jonas RA. Long-term follow-up of pediatric cardiac patients requiring mechanical circulatory support. *The Annals of Thoracic Surgery.* 2000;69:186-192.
- [156] Levi D, Marelli D, Plunkett M, et al. Use of assist devices and ECMO to bridge pediatric patients with cardiomyopathy to transplantation. *The Journal of heart and lung transplantation.* 2002;21:760-770.
- [157] Bae J-O, Frischer JS, Waich M, Addonizio LJ, Lazar EL, Stolar CJH. Extracorporeal membrane oxygenation in pediatric cardiac transplantation. *Journal of Pediatric Surgery.*40:1051-1057.
- [158] Almond CS, Morales DL, Blackstone EH, et al. The Berlin Heart EXCOR® pediatric ventricular assist device for bridge to heart transplantation in US children. *Circulation.* 2013:CIRCULATIONAHA. 112.000685.
- [159] Johnson CA, Wearden PD, Kocyildirim E, et al. Platelet Activation in Ovine Undergoing Sham Surgery or Implant of the Second Generation PediaFlow Pediatric Ventricular Assist Device. *Artificial Organs.* 2011;35:602-613.
- [160] Bachman TN, Bhama JK, Verkaik J, Vandenberghe S, Kormos RL, Antaki JF. In vitro evaluation of ventricular cannulation for rotodynamic cardiac assist devices. *Cardiovascular engineering and technology.* 2011;2:203-211.
- [161] Bhama JK, Bachman TN, Kormos RL, Borovetz H, Antaki JF. Development of an ex vivo ovine ventricular assist device model for intraventricular visualization of the inflow cannula. *The Journal of Heart and Lung Transplantation.* 2009;28:860-861.
- [162] Olia SE, Maul TM, Shankarraman V, et al. Biocompatibility Testing of the Frozen Design 4th Gen. PediaFlow(R) Pediatric VAD. *American Society for Artificial Internal Organs, 58th Annual Conference.* San Francisco2012.

- [163] Olia SE, Maul TM, Snyder ST, et al. Inflow Cannula Enhancements for the PediaFlow(R) Pediatric VAD. *American Society for Artificial Internal Organs, 59th Annual Conference*. Chicago, IL2013.
- [164] Ferreira A, Boston JR, Antaki JF. A control system for rotary blood pumps based on suction detection. *IEEE Trans Biomed Eng*. 2009;56:656-665.
- [165] Arndt A, Nüsser P, Graichen K, Müller J, Lampe B. Physiological control of a rotary blood pump with selectable therapeutic options: control of pulsatility gradient. *Artificial organs*. 2008;32:761-771.
- [166] Watanabe K, Asai T, Ichikawa S, et al. Development of a flexible inflow cannula with a titanium inflow tip for the NEDO biventricular assist device. *ASAIO J*. 2004;50:381-386.
- [167] Schmid C, Jurmann M, Birnbaum D, et al. Influence of inflow cannula length in axial-flow pumps on neurologic adverse event rate: results from a multi-center analysis. *J Heart Lung Transplantation*. 2008;27:253-260.
- [168] James NL, van der Meer AL, Edwards GA, et al. Implantation of the VentrAssist implantable rotary blood pump in sheep. *ASAIO journal*. 2003;49:454-458.
- [169] Sawyer D. Do It By Design: An Introduction to Human Factors in Medical Devices. In: U.S HHS P, Food and Drug Administration, ed. Center for Devices and Radiological Health1996.
- [170] Ferreira A, Chen S, Simaan MA, Boston JR, Antaki JF. A discriminant-analysis-based suction detection system for rotary blood pumps. *EMBS Annual International Conference*. New York City2006.
- [171] Noon GP, Loebe M. Current Status of the MicroMed DeBakey Noon Ventricular Assist Device. *Tex Heart Inst. J*. 2010;37:652-653.
- [172] Bertram CD. Measurement for implantable rotary blood pumps. *Physiological measurement*. 2005;26:R99.
- [173] Farrar DJ, Bourque K, Dague CP, Cotter CJ, Poirier VL. Design Features, Developmental Status, and Experimental Results With the Heartmate III Centrifugal Left Ventricular Assist System With a Magnetically Levitated Rotor. *ASAIO Journal*. 2007;53:310-315.
- [174] Arnold WS, Bourque K. The engineer and the clinician: Understanding the work output and troubleshooting of the HeartMate II rotary flow pump. *J Thorac Cardiovasc Surg*. 2013;145:32-36.
- [175] Ayre PJ, Lovell NH, Woodard JC. Non-invasive flow estimation in an implantable rotary blood pump: a study considering non-pulsatile and pulsatile flows. *Physiological measurement*. 2003;24:179-189.

- [176] Pirbodaghi T, Weber A, Carrel T, Vandenberghe S. Effect of pulsatility on the mathematical modeling of rotary blood pumps. *Artif Organs*. 2011;35:825-832.
- [177] Pennings KAMA, Martina JR, Rodermans BFM, et al. Pump Flow Estimation From Pressure Head and Power Uptake for the HeartAssist5, HeartMate II, and HeartWare VADs. *ASAIO Journal*. 2013;59:420-426.
- [178] Tsukiya T, Akamatsu T. Use of Motor Current in Flow Rate Measurement for the Magnetically Suspended Centrifugal Blood Pump. *Artificial Organs*. 1997;21:396-401.
- [179] Lim E, Karantonis D. Noninvasive Average Flow and Differential Pressure Estimation for an Implantable Rotary Blood Pump Using Dimensional Analysis. *IEEE Trans Biomed Eng*. 2008;55:2094-2100.
- [180] Webber S. Pediatric circulatory support contractors' meeting: report of the clinical trials working group. *ASAIO J*. 2009;55:10-12.
- [181] Borovetz HS, Badylak SF, Boston JR, et al. Towards the Development of a Pediatric Ventricular Assist Device. *Cell Transplantation*. 2006;15:S69-S74.
- [182] Wearden PD, Morell VO, Keller BB, et al. The PediaFlow pediatric ventricular assist device. *Semin Thorac Cardiovasc Surg Pediatric Card Surg Annu*. 2006;9:92-98.
- [183] Baldwin JT, Adachi I, Teal J, et al. Closing in on the PumpKIN Trial of the Jarvik 2015 Ventricular Assist Device. *Seminars in thoracic and cardiovascular surgery. Pediatric cardiac surgery annual*. 2017;20:9-15.
- [184] Yeleswarapu KK, Antaki JF, Kameneva MV, Rajagopal KR. A Mathematical Model for Shear-Induced Hemolysis. *Artificial Organs*. 1995;19:576-582.
- [185] Dobbe J, Streekstra G, Hardeman M, Ince C, Grimbergen C. Measurement of the distribution of red blood cell deformability using an automated rheoscope. *Cytometry*. 2002;50:313-325.
- [186] Hébert PC, Wells G, Blajchman MA, et al. A multicenter, randomized, controlled clinical trial of transfusion requirements in critical care. *New England Journal of Medicine*. 1999;340:409-417.
- [187] Politsmakher A, Doddapaneni V, Seeratan R, Dosik H. Effective reduction of blood product use in a community teaching hospital: when less is more. *The American journal of medicine*. 2013;126:894-902.
- [188] Besarab A, Goodkin DA, Nissenson AR. The normal hematocrit study—follow-up. *New England Journal of Medicine*. 2008;358:433-434.

- [189] Singh AK, Szczech L, Tang KL, et al. Correction of anemia with epoetin alfa in chronic kidney disease. *New England Journal of Medicine*. 2006;355:2085-2098.
- [190] Mix T-CH, Brenner RM, Cooper ME, et al. Rationale—Trial to Reduce Cardiovascular Events with Aranesp Therapy (TREAT): evolving the management of cardiovascular risk in patients with chronic kidney disease. *American heart journal*. 2005;149:408-413.
- [191] Finfer S, Bellomo R, Boyce N, et al. A comparison of albumin and saline for fluid resuscitation in the intensive care unit. *N Engl J Med*. 2004;350:2247-2256.
- [192] Lippi G, Mercadanti M, Aloe R, Targher G. Erythrocyte mechanical fragility is increased in patients with type 2 diabetes. *European journal of internal medicine*. 2012;23:150-153.
- [193] Tarasev M, Alfano K, Chakraborty S, Light L, Doeden K, Gorlin JB. Similar donors—similar blood? *Transfusion*. 2014;54:933-941.
- [194] Presley TD, Perlegas AS, Bain LE, et al. Effects of a single sickling event on the mechanical fragility of sickle cell trait erythrocytes. *Hemoglobin*. 2010;34:24-36.
- [195] Madden JL, Drakos SG, Stehlik J, et al. Baseline red blood cell osmotic fragility does not predict the degree of post-LVAD hemolysis. *ASAIO journal (American Society for Artificial Internal Organs: 1992)*. 2014;60:524.
- [196] Muzykantov VR. Drug delivery by red blood cells: vascular carriers designed by mother nature. *Expert opinion on drug delivery*. 2010;7:403-427.
- [197] Olia SE, Maul TM, Kameneva MV. The Effect of Inlet Pressure on Gas Embolism and Hemolysis in Continuous-Flow Blood Pumps. *ASAIO 57th Annual Conference*. Washington, DC2011.
- [198] Pedersen TH, Videm V, Svennevig JL, et al. Extracorporeal membrane oxygenation using a centrifugal pump and a servo regulator to prevent negative inlet pressure. *The Annals of thoracic surgery*. 1997;63:1333-1339.
- [199] Wagner K, Risnes I, Abdelnoor M, Karlsen H, Svennevig J. Is it possible to predict outcome in pulmonary ECMO? Analysis of pre-operative risk factors. *Perfusion*. 2008;23:95-99.
- [200] Pohlmann JR, Toomasian JM, Hampton CE, Cook KE, Annich GM, Bartlett RH. The Relationships between Air Exposure, Negative Pressure and Hemolysis. *ASAIO journal (American Society for Artificial Internal Organs: 1992)*. 2009;55:469.
- [201] Chambers SD, Ceccio SL, Annich GA, Bartlett RH. Extreme negative pressure does not cause erythrocyte damage in flowing blood. *ASAIO journal*. 1999;45:431-435.